Catalytic Conversion of Carbon Monoxide and Methane over Metal and Metal Oxide Catalysts: Synthesis, In-Situ X-Ray Spectroscopy Study, and Catalytic Performance

By

Wenchi Liu

A dissertation submitted in partial satisfaction of the

requirements for the degree of

Doctor of Philosophy

in

Chemistry

in the

Graduate Division

of the

University of California, Berkeley

Committee in charge:

Prof. Gabor A. Somorjai, Chair

Prof. Peidong Yang

Prof. Marcin Majda

Prof. Alexis T. Bell

Spring 2018

Catalytic Conversion of Carbon Monoxide and Methane over Metal and Metal Oxide Catalysts: Synthesis, In-Situ X-Ray Spectroscopy Study, and Catalytic Performance

By

Wenchi Liu

Abstract

Catalytic Conversion of Carbon Monoxide and Methane over Metal and Metal Oxide Catalysts: Synthesis, In-Situ X-Ray Spectroscopy Study, and Catalytic Performance

by

Wenchi Liu

Doctor of Philosophy in Chemistry

University of California, Berkeley

Professor Gabor A. Somorjai, Chair

Catalysis is of vital importance in a wide range of areas including energy processing and chemical production. Catalytic conversion of C_1 sources such as carbon monoxide and methane to make hydrocarbon fuels and oxygenated products has far reaching implications especially in the context of the gradual depletion of crude oil resource and the potential surge in the natural gas production in the coming decades. The control over reaction activity and selectivity for the conversion CO and CH_4 in the Fischer–Tropsch synthesis and oxidative coupling of methane (OCM) have received tremendous attention and have been proved challenging. This dissertation focuses on the catalytic conversion of CO (Fischer–Tropsch synthesis) using supported cobalt based bimetallic nanoparticle model catalysts and the oxidative coupling of methane with noble metal promoted metal oxide catalysts.

Using colloidal synthesis, a series of cobalt based bimetallic nanoparticles Co–M (M = Mn, Ru, Rh, and Re) with well-defined sizes, shapes, and compositions were obtained. Detailed synthesis procedures were presented and key synthetic parameters were discussed. The as-synthesized nanoparticles were subjected to extensive in-situ X-ray spectroscopy studies using ambient pressure X-ray photoelectron spectroscopy (AP-XPS) and X-ray absorption spectroscopy (XAS) under catalytic relevant conditions. Composition wise, the results indicate the surface concentration of Co on the as-synthesized Co–M bimetallic particles is slightly less than the bulk atomic Co %. While oxidation treatment led to a slight increase of the surface Co, major effect was seen after the reduction treatment where surface segregation of the second metal resulted in a drastic decrease of the surface Co content. The effect is more pronounced at elevated reduction temperatures. Under reaction conditions, the surface compositions remained similar to those after the reduction treatment at high temperatures. Among the bimetallics tested, the Co–Mn system is relatively less susceptible to surface reconstructions induced by oxidation and reduction treatments. In addition, the reducibility of Co was also shown to be modified depending on the second metal present and Re was proved to be most efficient in leading to a facile reduction of Co. Catalytic performance of the bimetallic catalysts supported on mesoporous silica MCF–17 indicates a positive effect in the catalytic activity for Co–Rh and Co–Mn systems, while Co–Re and Co–Cu showed decreased activity. Less pronounced promotion effect of the second metal on the product distribution was observed with only a slight increase in the selectivity towards C_{5+} products. The selectivities for CH_4 and C_{5+} of the various Co–M

bimetallic catalysts generally resemble those of pure Co catalysts. Although in extremely low selectivity, alcohols were also formed with Co–Rh and Co–Cu bimetallic catalysts. The appearance of longer chain alcohol such as propanol, which was not present for pure Co catalysts, is an evidence for potential synergistic promotion.

For oxidative coupling of methane (OCM), the promotion effect of noble metals (Pt, Ir, and Rh) on the performance of Mn_xO_y-Na_2WO_4/MCF–17 catalysts was investigated. The introduction of noble metals had little effect on the surface area and phase composition of the original catalyst but led to a more reduced nature of the surface oxide species. Catalytic study revealed an enhanced selectivity towards both C_2 and C_3 hydrocarbons as compared to the undoped Mn_xO_y-Na_2WO_4/MCF–17 catalyst in the order of Rh-doped > Ir-doped > Pt-doped samples together with a lower olefin to paraffin ratio. A more optimized strength of interaction between the carbon intermediates and the catalyst surface was suggested, which in combination with the improved reducibility of Mn and W species are believed to be responsible for the improved performance.

In addition, monodispersed leaf-like manganese–tungsten–oxide (Mn–W–O_x) nanoparticles and hydroxylated hexagonal boron nitride (*h*-BN) were synthesized and used as novel catalysts in OCM reaction. Preliminary results indicate that the MCF–17 supported Mn–W–O_x nanoparticle catalyst showed a CH_4 conversion of 5.4% and C_2 selectivity of 42% with good stability over time. On the other hand, hydroxylated *h*-BN exhibited good activity (~20% CH_4 conversion) with moderate selectivity towards C_2 hydrocarbons (20%–30%). However, the hydroxylated *h*-BN catalysts faced serious deactivation, which was not eliminated by lowering the reaction temperature or the oxygen concentration in the reaction gas feed.

Table of Contents

Abstract **1**

Table of Contents ..... **i**

Acknowledgements ..... **iii**

Chapter 1 Introduction **1**

1.1 Background and Motivation 1

1.1.1 Heterogeneous Catalysis 1

1.1.2 Nanoscience and Nanotechnology 1

1.1.3 Impact of Nanoscience on Heterogeneous Catalysis 2

1.2 Fabrication of Bimetallic Nanoparticles 3

1.3 Promotion Effects in Heterogeneous Catalysis 5

1.4 Fischer–Tropsch Synthesis over Co Catalysts 6

1.5 Oxidative Coupling of Methane (OCM) 7

1.5.1 Utilization of Natural Gas 7

1.5.2 Direct Methane Conversion and Oxidative Coupling of Methane (OCM) 8

1.6 Summary of Dissertation 11

1.7 References 12

Chapter 2 Experimental **16**

2.1 Material Synthesis 16

2.1.1 Synthesis of Single Metallic Nanoparticles 16

2.1.2 Colloidal Synthesis of Co–M Bimetallic Nanoparticles (M = Mn, Cu, Ru, Rh, Re) 16

2.1.3 Synthesis of Mesoporous Silica Support MCF–17 Using Microemusion Templating Method 16

2.1.4 Fabrication of MCF–17 Supported Metal Nanoparticle Catalysts 17

2.1.5 Synthesis of Noble Metal Doped M–Mn_xO_y–Na_2WO_4/SiO_2 (M =Pt, Ir, Rh) Catalysts 18

2.2 Material Characterization 18

2.2.1 Electron Microscopy (EM) 18

2.2.2 X-Ray Based Techniques 21

2.2.3 Inductively Coupled Plasma Atomic Emission Spectroscopy (ICP–AES) 25

2.2.4 N_2 Adsorption 27

2.3 Catalytic Measurements 28

2.3.1 High Pressure Steady–State Reactor for the Fischer–Tropsch Reaction 28

2.3.2 Ambient Pressure Steady–State Reactor for Oxidative Coupling of Methane (OCM) 29

2.4 References 30

Chapter 3 Cobalt Based Bimetallic Nanoparticles for the Hydrogenation of Carbon Monoxide: Synthesis, Catalytic Performance, and In–Situ X–Ray Spectroscopy Study 32

3.1 Introduction 33

3.2 Experimental 34

3.3 Results and Discussion 39

3.3.1 Synthesis of Co–M (M = Rh, Mn, Cu, Re, Ru) Bimetallic Nanoparticles 39

3.3.2 Synchrotron Based X–Ray Spectroscopic Studies 41

3.3.3 High Pressure Reactor Studies 51

3.4 Conclusions 55

3.5 References 56

Chapter 4 Oxidative Coupling of Methane (OCM): Effect of Noble Metal (M = Pt, Ir, Rh) Doping on the Performance of Mesoporous Silica MCF–17 Supported Mn_xO_y-Na_2WO_4 Catalysts 60

4.1 Introduction 61

4.2 Experimental 61

4.3 Results and Discussion 63

4.3.1 Characterizations 63

4.3.2 Catalytic Measurements 70

4.4 Conclusions 73

4.5 References 73

Chapter 5 Preliminary Study of Manganese–Tungsten–Oxide (Mn–W–O_x) Nanoparticles and Hydroxylated Hexagonal Boron Nitride (*h*-BN) Catalysts in Oxidative Coupling of Methane (OCM) 75

5.1 Introduction 76

5.2 Experimental 77

5.3 Results and Discussion 79

5.3.1 Manganese–Tungsten–Oxide (Mn–W–O_x) Nanoparticles 79

5.3.2 Hydroxylated Hexagonal Boron Nitride (*h*-BN) 82

5.4 Conclusions and Future Work 84

5.5 References 85

Acknowledgements

The research contained within this dissertation was supported by the Director, Office of Science, Office of Basic Energy Sciences, Division of Chemical Sciences, Geological, and Biosciences, U.S. Department of Energy, under Contract DEAC02-05CH11231.

First of all, I would like express my deepest gratitude to my PhD advisor Prof. Gabor A. Somorjai for the opportunity to study in the group and for his generous and continuing support throughout my pursuing for the degree. The research philosophy and decades of experience he conveyed to me are invaluable and will continue to play an important role in my career ahead. His guidance also extends beyond academic research and shaped me as a person. I enjoyed his mentorship as well as the stories he shared with us during the subgroup meetings.

In addition, I would like to especially thank Dr. Gérôme Melaet, who was both a friend and a mentor. The training he gave me was priceless and equipped me with skills and knowledge to explore in the field of catalysis. I would also like to thank the other member of the 'Team W', Dr. Walter T. Ralston, without whom I could not have enjoyed my days in the lab that much. I will always remember our own catalysis subgroup meetings in the hallway and the little talks we had in our offices. I truly learned a lot from them and will cherish our friendship for the years to come.

I am grateful to Dr. Selim Alayoglu, Dr. Kwangjin An, and Mr. Cheng-Shiuan Li for their impressive knowledge and guidance on the material synthesis, to my officemate Dr. Yonatan Horowitz for his insightful discussions and all the cheer-ups, and to Ms. Inger Coble for all of her support that made my life in the lab easy. I am also grateful to all my friends in the Somorjai group for the past five years, Ji Su, Rong Ye, Christophe Deraedt, Bing Yuan, Lynda Han, Tyler Hurlburt, Jayeon Baek, Yongju Yun, Nate Musselwhite, Feifei Shi, Zhongwei Zhu, Lindsay Carl, Griffin Kennedy, and many others for their help and tolerance. The group felt like a big family with them around.

Outside the Somorjai group, I will miss the days I spent together with my friends Chenlu Xie, Zheyue Yang, Hoduk Cho, and Sumin Lee, when we studied together in the library and made it through quantum mechanics and statistical mechanics.

My acknowledgement would not be complete without my dad Zonghuai and mom Liping. Thank you for always being so considerate and supportive, especially during the hard time. Our weekly video call always made me feel refreshed and prepared me for the challenges both at school and in life.

Last but not least, my PhD life could have been dull and much tougher if not for the love and company from my Fiancée Zeqiong Zhao. The feeling of knowing you will always be by my side is heartwarming and encouraging. I am looking forward to spending my life with you in the years ahead.

Chapter 1 – Introduction

1.1 Background and Motivation

1.1.1 Heterogeneous Catalysis

Catalysis is of vital importance and is ubiquitously used in a wide range of applications. From the catalytic converter in automobiles to production of plastics for packaging and construction, from pharmaceutical products to fuels for transportation, it helps to shape the world and improve the quality of human's life in every way possible. Catalysis can generally be classified into three fields, homogeneous, heterogeneous, and enzymatic. Among them, heterogeneous catalysis in which catalysts and reactants are in different phases, benefits from the easy regeneration and excellent recyclability of the catalyst as well as its tolerance for wide range of operating conditions and is therefore widely used in industrial applications.

Modern heterogeneous catalysis dates from the middle of 18th century, when platinum containing catalysts were used in the production of oleum, and has made considerable achievements in the 20th century [1, 2]. During the course of development, it has been drastically expanding its influence and is now playing a pivotal role in various important fields such as energy, environment, and healthcare. Reactions that have made their names in the history and contributed tremendously to our society, such as ammonia synthesis and Fischer–Tropsch reaction, all owe themselves to heterogeneous catalysis. Now, novel heterogeneous catalysts and catalytic processes are being continuously developed to both improve the imperfect and conquer the impossible.

Heterogeneous catalysis in the 21st century has shifted its focus from simply boosting the catalytic turnover to pursuing 100% reaction selectivity [3, 4], aiming for greener and more efficient catalytic processes that will make better use of the increasingly precious natural resources and alleviate environmental pollution by wasteful and harmful byproducts. For this purpose, rational design of both the catalysts and catalytic processes is indispensable. Thanks to the emergence of nanoscience and advanced characterization techniques, understanding and control of catalytic structures can now be achieved on the atomic level [5], which greatly facilitates the catalyst development.

1.1.2 Nanoscience and Nanotechnology

The history of nanoscience dates back to ancient times where colloidal gold nanoparticles were used as pigments for esthetic and curative purpose or as essential ingredients in making glasses that can change color upon light irradiation, as those used in the famous Lycurgus cup back in the 4th century [6]. Until the 16th to 17th century, very little understanding, if any, was made towards neither the formation nor the properties of the nanoparticle colloidal that had been used. In the year of 1857, Michael Faraday reported the famous synthesis of gold colloidal by reducing an aqueous solution containing $AuCl_4^-$ with phosphorous in CS_2 [6]. The discovery has been inspiring and influencing the synthesis of metal nanoparticles ever since. Then in 1959, Richard P. Feynman gave his iconic talk named '*There's Plenty of Room at the Bottom*' and envisioned manipulating and controlling objects at atomic scale [7], which marked the beginning of the bloom of nanoscience in the second half of the 20th century. Particularly, the last few decades saw a

boom in nanoscience research both in terms of fundamental knowledge and practical applications.

Modern nanoscience and nanotechnology describes itself as the investigation and manipulation of matter with at least one dimension in the size range of 1-100 nm [8], which lies between the size of macro or bulk systems and individual atoms. It has been the focus of numerous academic researches and tens of thousands of papers and patens are published every year. Scientific disciplines that actively involves the use and development of nanomaterials and related technology span from photonics, catalysis, and information science to manufacturing, neuroscience, and even military [8].

Discoveries made in this field have being changing our lives in various ways and is expanding its influence in a massive scale with an ever increasing pace. Commercial products based on discoveries from nanoscience and technology are readily available: silver nanoparticles as antibacterial agent [9], nanoparticle-based sunscreens [10, 11], and nanoparticle-enhanced food packaging with antimicrobial ability and better mechanical properties [12], to name a few. The primary application market for nano-enabled products are pharmaceutical industry, electronics, energy conversion and storage, chemical production and processes, automotive industry, and environmental applications, with hundreds of billions of dollars of revenue each year which will continue to increase in the decades to come [13].

1.1.3 Impact of Nanoscience on Heterogeneous Catalysis

Most of the fascinating performance and exciting applications of nanomaterials originate from the new properties evolved with their small dimensions. According to the quantum size effect, nanoparticles with diameter of one to a few tens of nanometers display unique physical and chemical properties that are very different from those of bulk or molecular compounds [6]. These properties are usually dependent on the size and shape of the particles and are affected by their special arrangement (e.g. formation of nanoparticle superlattice). This effect stems from the fact that the de Broglie wavelength of the electron is of the same order as the size of the nanoparticle, which resembles themselves to the model of particle in the box and subject them to quantum mechanical rules. One of the famous example of the properties resulting from the quantum size effect is the size-dependent emission spectrum of quantum dots [14]. Other interesting properties include lowered melting temperature, size-induced metal-insulator transition, and size-dependent magnetic susceptibility [15].

The introduction of nanoparticle catalysts also has a huge impact on heterogeneous catalysis. The pioneering work by Haruta *et al.* for the first time showed that highly dispersed Au nanoparticles supported on various transition metal oxides can exhibit exceptionally high activity in low temperature CO oxidation even below 0 ºC [16, 17], which is in sharp contrast to the traditional belief about gold. This unusual activity was later attributed to the availability of a high concentration of low-coordinated sites and the presence of oxidized Au species on nano-sized gold [18, 19].

The utilization of nanocatalysts has many unique advantages. First of all, due to the high specific surface area of nanoparticles, the amount of catalyst needed can be substantially reduced, which is especially important for catalysts containing noble metals.

In addition, nanoparticles also have substantially more coordination-unsaturated sites such as edges and kinks, which are often found to possess higher activity than atoms on terraces. Moreover, nanoparticles are more flexible and can reconstruct more readily than large clusters [3], which is essential for the rearrangement of adsorbed reactant molecules and is a vital step in the total catalytic cycle.

The widespread use of nanoparticles in heterogeneous catalysis has stimulated the advancement in the characterization techniques to probe into that small dimension with extreme sensitivity and accuracy as well as atomic-level resolution [5, 20, 21]. For example, the development of electron microscopy (EM) enables us to visually see the size, shape, and surface structure of the nanoparticles, which is impossible with conventional light microscopes. Since catalysis is essentially a surface process, the invention of scanning probe microscope (SPM) is extremely powerful in examining the surface of the catalyst atom by atom. Some of the commonly used characterization techniques include transmission electron microscopy (TEM), scanning electron microscopy (SEM), atomic force microscopy (AFM), scanning tunneling microscopy (STM), X-ray photoelectron spectroscopy (XPS), small angle x-ray scattering (SAXS), X-ray diffraction (XRD), *etc*.

In addition, as synchrotron radiation source becomes readily available and techniques like differential pumping are widely adopted, in-situ characterization methods such as ambient pressure-XPS (AP-XPS), near edge X-ray absorption fine structure (NEXAFS) spectroscopy, environmental TEM, and high-pressure STM have all been realized, which endowed us the power to in-situ observe reaction processes and study catalyst properties under reaction conditions to gain molecular-level understanding.

1.2 Fabrication of Bimetallic Nanoparticles

As mentioned in the previous section, metal nanoparticles play a vital role in modern catalysis. By introducing a second metal to single metallic nanoparticles, bimetallic nanoparticles are formed, which provides more dandles in tuning the catalytic performance. Utilization of bimetallic nanoparticle catalysts has many advantages. First of all, by incorporating inexpensive heteroatoms into noble metal nanoparticles, the use of scarce precious metals can be cut. In addition, through careful design, the second metal could potentially serve as a new type of active site, which will lead to a bifunctional catalyst capable of catalyzing reactions that are not possible with its single metallic counterpart. Furthermore, novel properties could evolve from the promotion and synergistic effect between the two components of the bimetallic system, giving birth to new capabilities of the catalyst.

In addition to the size, shape, and exposing facets that are commonly controlled for single metallic nanoparticles, the arrangement of atoms within bimetallic nanoparticles adds another layer of complexity, based on which three types of bimetallic structure can be distinguished (Fig. 1–1) [22]. The first type is core/shell, where atoms of one element forms an inner core and a shell of heteroatoms completely covers its surface. The second type is called heterostructure, in which both metals form their own clusters but share a limited number of interface. The last type of bimetallic structure is alloy, which is substantially different from the core/shell and the heterostructure. In an alloy, atoms of different metals

are homogeneously mixed and held together by metal-metal bonds, and depending on the types of alloy, can be completely random or have long-range orders [23].

The synthesis of bimetallic nanoparticle is controlled by many aspects and several variables can be adjusted to direct the growth of the nanoparticle towards the desired direction. Despite the intrinsic mixing pattern of the two metals, the composition, shape, and structure of the bimetallic nanoparticles can be controlled via the reaction temperature and time, use of surface capping agent, types of precursor and reducing agent as well as their concentration, *etc*. These variables all together would tailor the reaction thermodynamics and kinetics.

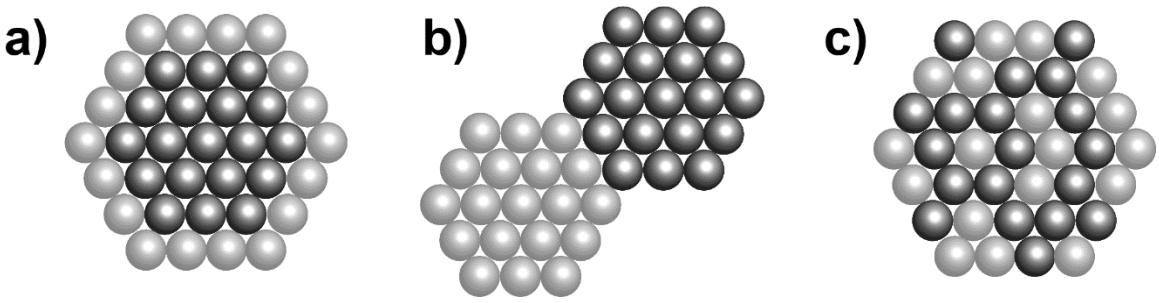

Fig. 1–1. Three types of bimetallic nanostructures: a) core/shell, b) heterostructured, and c) alloy.

Synthetic methods for bimetallic nanoparticles can be classified in various ways. From experimental point of view, three types of techniques are commonly used: co-reduction, thermal decomposition, and seeded growth [22, 24]. In co-reduction, metal salts of different elements are reduced simultaneously. Therefore, the nature of the precursor (its redox potential) and the power of the reducing environment (reducing agent, temperature, and exotic ions) are vital in controlling the final product. Other components in the reaction media such as solvents and surface capping agents could also contribute to the final results. With proper design, all three types of bimetallic nanostructures could be prepared using the co-reduction method.

When thermal decomposition is used, metal precursors, usually organometallic compounds such as metal carbonyls, are subject to a high temperature reaction media, where they are decomposed to form nanoparticles. In this approach, coordinating the decomposition of different precursors is the key. Since the metals are in zero-valence, no reducing agent is necessary. Therefore, decomposition rates of metal precursors are usually adjusted by the reaction temperature, addition of proper catalysts, and using precursors with different ligands. However, methods that combine both the reduction and decomposition of different metal precursors have also been reported.

In both co-reduction and thermal decomposition methods, depending on the nucleation and growth pattern, either continuous growth or crystal coalescence could occur [25]. In the continuous growth mode, both metal precursors are reduced simultaneously in a controlled manner to form nuclei, to which freshly reduced metal atoms are added during the growth period to form the final nanoparticle. On the other hand, if explosive nucleation occurs, small crystallites of both metals would form in large quantity within a short period of time, exhausting the monomer concentration and forcing the growth to go into a coalescence mode. If the nucleation rate of one metal is substantially higher, seed clusters

containing only that metal will be formed first and serve as the seed for the growth of the second metal.

Seeded growth describes a strategy where pre-prepared metal 'seeds' are used to modulate the growth of the second metal. This method is most powerful in producing core/shell and heterostructured nanoparticles. Small lattice mismatch and strong affinity between the seed and the second metal would facilitate epitaxial growth. In addition, attention must be paid to suppress the homogeneous nucleation of the second metal by keeping the reduction mild and in near-equilibrium conditions. Galvanic replacement represents a special case of seeded growth, where the redox potential of the second metal is higher than that of the seed. Therefore, during the course of reaction, the seed will serve as a sacrificial template to reduce the second metal ions, from which concave and hollow bimetallic nanostructures could be obtained. The amount of the second metal and the replacement process need to be carefully controlled to avoid excessive consumption of seed atoms and destruction of the seed structure.

It should be noted that the real situation is rather complex and to attribute the formation of bimetallic nanoparticles to a certain method or phenomenon alone is impractical. In fact, some of the methods discussed above are closely connected, and in most cases, two or more are actually involved in the formation of bimetallic nanoparticles.

1.3 Promotion Effects in Heterogeneous Catalysis

Catalyst promoters are compounds that are added intentionally in small quantity into the real catalyst to enhance its performance. They will effectively improve the activity, selectivity, or stability of the catalyst while having little or no catalytic effect by themselves. They are usually incorporated via impregnation methods (co-impregnation or subsequent impregnation) or introduced as the catalyst support. Promoters are essential components of the working catalyst and are widely used in catalyst design.

Promotion effects in heterogeneous catalysis can be classified into two major categories: structural and electronic [26], although other forms of promotion also exist such as selective site blocking and suppression of non-selective gas phase reactions [27]. Structural and electronic promotion effects are generally concentration dependent and can take place at the same time or even interplay with each other during a catalytic process.

Structure promoters typically function by tailoring the interaction between the active species and catalyst supports [26]. Higher activity and stability of the catalyst could be achieved by increasing the dispersion of surface active species and preventing the agglomeration and sintering of nanoparticle catalysts. In some cases, structural promoters work by suppressing compound formation between the active component and catalyst support, thus improving the lifetime of the catalyst. An example of structural promotion is the addition of Al_2O_3 in iron catalysts for ammonia synthesis. The introduction of Al_2O_3 enhances both the activity and stability of the catalyst by increasing the iron surface area and reduce the loss of potassium from the surface [27].

Electronic promotion basically works by altering the electronic environment around the active species through either donation or withdraw of electrons [26]. As a result, catalysts often see an improved reducibility and interaction with reactant molecules and/or

key surface intermediates, thus enhancing both the reaction activity and selectivity. Potassium in Fe catalysts used in ammonia synthesis is an excellent example of electronic promotion [28, 29]. The addition of K greatly enhances the catalytic turnover due to a lowered ammonia adsorption energy, which decreases the number of active sites blocked by the ammonia product, and an increased N_2 adsorption energy, which lowers the activation barrier for nitrogen dissociative chemisorption.

Co Fischer-Tropsch catalyst promoted with Ru represents a case of simultaneous structural and electronic promotion. The addition of Ru results in the formation CoRu bimetallic domains with intimate contact between the two metals. Such Co surface sites exhibit much stronger resistance to carbon depositions [30], thus retaining their activity during the reaction. In addition, the presence of Ru can enhance the reduction of cobalt oxides through hydrogen spillover, leading to an increase in the exposed Co^0 sites and therefore an increased CO hydrogenation rate [31]. However, it should be mentioned that promotion associated with other noble metals (Re, Pt, Pd, and Ir) mainly results in an increase in the overall reaction rate with less pronounced effect on the hydrocarbon selectivity [31].

1.4 Fischer-Tropsch Synthesis over Co Catalysts

Fischer-Tropsch (F-T) synthesis uses syngas (a mixture of CO and H_2) to produce long-chain hydrocarbons. It was firstly developed by German inventors Hans Fischer and Franz Tropsch in the 1920s and played a crucial role in delivering liquid hydrocarbon fuels for Germany during World War II. Now F-T synthesis is a major part of Gas-to-Liquids (GTL) and Coal-to-Liquids (CTL) technologies which have been industrially practiced in various parts of the world. Some famous plants that are currently operating include the Sasol plant in South Africa and the Shell plant in Malaysia and many others are under different stage of implementation.

Cobalt and iron catalysts are most frequently used for F-T reaction and have been the focus in majority of scientific researches. Other metals such as ruthenium and nickel also exhibit good activity but have obvious drawbacks such as the limited availability of ruthenium and high methane selectivity for nickel catalysts. As F-T synthesis is essentially a surface polymerization reaction, the product distribution follows the Anderson-Schulz-Flory (ASF) model (Eq. 1–1). In Eq. 1–1, W_n is the weight percentage, n is the chain length of the hydrocarbon, and α is the overall chain growth probability which is independent of chain length n.

$$\log\left(\frac{W_n}{n}\right) = n\log\alpha + \log\left(\frac{(1-\alpha)^2}{\alpha}\right) \qquad \textbf{Eq. 1–1}$$

The mechanism of F-T reaction remains elusive due to the complicated network of surface reactions and large array of reaction products. The mechanism for the formation of monomers and the subsequent chain growth step has long been debated and it is likely that multiple routes involving different key intermediates coexist under practical F-T conditions and contribute to the formation of different types of products. However, there is no consensus on which mechanism dominates. The reaction pathway also differs based on the type of catalyst used, adding another layer of complexity. The original mechanism

proposed by Fischer and Tropsch back in the 1920s involves the formation of surface metal carbides and their subsequent hydrogenation to methylene species, which are polymerized to form hydrocarbon products. However, this mechanism has later become less popular for an increasing number of contradictory experimental results. Other mechanisms such as oxygenates and CO-insertion featuring different types of monomers and chain growth patterns have also been suggested [32, 33]. With the aid of surface science techniques, the original carbide mechanism is revived and advanced and the improved carbene mechanism is proposed. On cobalt F-T catalysts, one plausible monomer for chain growth is surface CH_2 species [32, 34–36], its formation however, is actively debated. Both direct CO dissociation [36–38] and hydrogen assisted route [35, 39–41] have been proposed and are supported by a series of experimental and theoractical discoveries. In the former route, CH_2 is formed by the hydrogenation of surface C species originated from the dissociation of chemisorbed CO. While the latter route features H-addition to the molecularly adsorbed CO and the formation of CH_2 monomer through HCO and HCOH intermediates.

Co catalysts are often used for low temperature F-T process, which is usually carried out at temperatures between 200–240 ˚C [42]. Due to their low activity in reverse water gas shift (RWGS) reaction, syngas with H_2/CO ratio close to 2 must be used. The catalysts are usually composed of active Co sites which are commonly believed to be metallic [43, 44], high surface area supports such as alumina and silica, and a small amount of metal or metal oxide promoters.

Co F-T catalysts exhibit strong size effect on catalytic performance. Optimum particle sizes have been reported to be around 8–10 nm for most supported Co catalysts. Larger particles show no change in the intrinsic reaction rate and smaller particles display both lowered activity and selectivity towards long chain hydrocarbons. The reasons behind the poor performance of cobalt particles with small sizes include an increased amount of strongly bonded surface carbon and oxygen acting as site blocking species (easier deactivation) [45], easier reconstruction leading to disappearance of active surface Co sites [46], and lower intrinsic activity at small terraces [47]. Besides the particles size, some of the desired properties of a good Co F-T catalyst include high density of cobalt surface metal sites, low fraction of non-reducible cobalt compound, and stable catalyst structure [31]. The deactivation of cobalt F-T catalysts is believed to result from a combination of several phenomena. Catalyst poisoning by sulfur impurities from syngas, particle sintering due to the high exothermicity of the reaction, formation of polymeric carbon, and oxidation of metallic active sites by steam could all contribute to the initial or long-term deactivation of Co F-T catalysts [48–51].

1.5 Oxidative Coupling of Methane (OCM)

1.5.1 Utilization of Natural Gas

Natural gas consists of more than 90% methane with the rest being ethane and propane. In 2016, the world natural gas reserve is about 186.9 trillion cubic meters, with most being located in the Middle East and Eurasia [52]. When compared based on the energy density, natural gas stores more than 2/3 of the energy that the world oil reserve can generate, making it one of the most important fossil fuels on earth. In addition to the already abundant natural gas reserve, the latest technology advancement such as hydraulic

fracturing and horizontal drilling have unlocked gas resources that were previously considered too difficult or costly to produce. The production of natural gas is also believed to grow rapidly through 2040, with unconventional production such as tight and shale gas becoming increasingly important [53]. Therefore, it is of great importance to develop efficient ways of its utilization.

Currently, natural gas is mainly used as an energy source. It is used as compressed natural gas (CNG) to fuel certain types of transportation, as liquefied natural gas (LNG) for household purpose, and as fuel in the gas turbine to produce electricity. Natural gas is also the largest growing fuel source and is expected to become the second largest energy source by 2040 [53]. It is suggested that by the end of 2040, natural gas will provide a quarter of global energy demand with about 5% of world's total transportation and 30% of world's electricity being powered up and generated by natural gas, respectively.

On the other hand, the demand for natural gas in the chemical industry is estimated to rise by 40% in the next two decades. However, as compared to this rapid increase, the ways CH_4 can be converted chemically are extremely limited. The only commercialized technology so far is through the production of syngas via methane reforming, which will then be utilized in subsequent processes such as ammonia synthesis, Fischer-Tropsch (F-T) synthesis, and methanol production. However, this approach is indirect and consists of multi-step reactions with different optimum operating conditions, making it complex for both fundamental research and process development. For the same reason, it requires immense energy input, making it inefficient and not cost-effective.

1.5.2 Direct Methane Conversion and Oxidative Coupling of Methane (OCM)

With the large and fast-growing world reserve of natural gas resource and a shift from conventional fossil fuels to clean energies, there is a greater interest in develop processes that can convert methane to value-added products both efficiently and cost-effectively. Particularly, direct methane conversion to chemicals and fuels is desperately desired to avoid the complex multi-step reaction and the energy penalty associated with the conventional syngas approach. In addition, by converting methane to chemicals such as hydrocarbons and alcohols, its transportation will become much easier, which is important for accessing remote resources. However, such technologies remain elusive largely due to the high inertness of C-H bonds in methane and difficulty in controlling the reaction selectivity.

Currently, the major technologies for direct methane conversion to value-added chemicals that are under investigation and development include methane aromatization (MA), methane halogenation, direct methane to methanol (DMTM) process, and oxidative coupling of methane (OCM) [54]. It should be noted that only heterogeneous processes involving chain-growth or functionalization of CH_4 are presented here and therefore methane cracking and homogeneous and enzymatic methane conversion are not included.

Methane aromatization (MA) works in non-oxidative conditions and produces valuable aromatic compounds such as benzene and naphthalene. The most commonly used catalysts for this reaction are Mo/ZSM-5 zeolites, while other catalyst systems consisting of a metal oxide MO_x (M = Mo, W, V, Cr) and zeolites have also been studied. It is believed that MA follows a bi-functional mechnism, where CH_4 is firstly activated on the in-situ

formed MoC sites and the oligomerization reaction follows on the acidic sites in zeolites [55]. The main drawbacks of this reaction are the thermodynamic limitation on the reaction yield and coke deposition on acidic sites, which is inevitable and will eventually lead to catalyst deactivation.

$$6CH_4 \rightarrow 9H_2 + C_6H_6 \quad \Delta H_{298K} = +531 \text{ kJ/mol} \qquad \textbf{Eq. 1–2}$$

The concept of direct methane to methanol (DMTM) process is appealing when compared to the energy-intensive CO/CO_2 hydrogenation approach. Substantial efforts have been made to realize and improve the process, which have shown great potential. The most efficient catalysts so far are Fe-ZSM-5 and Cu-ZSM-5. The active sites in these catalysts are usually binuclear and trinuclear metal-oxo species, which resemble the active site in methane monooxygenase (MMO). With Fe-ZSM-5 and Cu-ZSM-5, the reaction proceeds in multiple steps. The first step is the catalyst activation by N_2O/O_2 which helps to form the active metal-oxo species (over 400 °C). The second step is the so-called adsorption of methane (up to about 200 °C) where methane molecules are activated and surface-bound methanol molecules are produced. The final step is methanol extraction by flowing steam through the catalytic bed (up to about 200 °C). In addition, to recycle the catalyst after the reaction, thermal treatment of the catalyst to desorb water molecules is essential (over 400 °C). Problems with DMTM include very low productivity of methanol as compared to CO/CO_2 hydrogenation and complicated process conditions due to the need for the sequential treatment. As the optimal temperature is different for each step, co-feeding of oxidant, methane, and steam in a single step still remains a grand challenge.

Methane halogenation method involves extracting hydrogen from methane with either X_2 or HX (X = Cl, Br) and producing methyl halides (CH3–X with X = Cl, Br) under relatively mild conditions [56, 57]. The primary product methyl halides can further undergo hydrolysis to produce methanol, from which higher hydrocarbons can be synthesized. Disadvantage with this approach are problems with halogenated hydrocarbons and the corrosive nature of the reactants.

Oxidative coupling of methane (OCM) mainly produces C_2 hydrocarbons in the presence of an oxidative reagent and was first developed in the early 1980s [58]. Oxygen is most widely used for this reaction, which is readily available from air. Nitrous oxide is sometimes used as an alternative but is unsuitable for practical applications due to its low availability. Recently, sulfur as a 'soft' oxidant to selectively convert methane to ethylene with metal sulfides as catalysts has also been reported [59], but is still in the proof of concept stage. Besides the coupling reaction, there are several side reactions that take place at the same time under reaction conditions. The main side reactions in OCM are the overoxidation of CH_4 and further oxidation of reaction products due to the lower C-H bond strength in them. The produced CO and CO_2 would inevitably jeopardize the selectivity towards C_2 hydrocarbons.

$$CH_4 + 1/2O_2 \rightarrow 1/2C_2H_4 + H_2O \qquad \Delta H_{298K} = -184.8 \text{ kJ/mol} \qquad \textbf{Eq. 1–3}$$

$$CH_4 + 1/4O_2 \rightarrow 1/2C_2H_6 + 1/2H_2O \quad \Delta H_{298K} = -110.4 \text{ kJ/mol} \qquad \textbf{Eq. 1–4}$$

OCM is particularly attractive for its simplicity when compared to DMTM as it can proceed in a co-feed and continues mode with methane and the oxidizing reagent being the only reactants. It is friendlier to both the reactor and environment as no chemicals with high corrosiveness and toxicity are used. Catalysts in OCM are also more resistant to coke formation as compared to the ones used in MA because of the presence of oxidizing reagent in the reaction mixture.

OCM reactions are carried out at high temperatures, usually between 700 and 1000 ^{o}C at atmospheric pressure, although 'low' temperature OCM has also been achieved at temperatures as low as 500 ^{o}C [60, 61]. The necessity for high temperature is to ensure the activation of the rather inert C-H bond in the methane molecule, while the low pressure is mainly for safety concerns. The reaction gas feed is mostly CH_4-rich to suppress the nonselective gas phase reactions and stay out of the explosion range. The reaction is believed to proceed in the so-called Heterogeneous-Homogeneous (H-H) mechanism [62], where methane is firstly activated on the surface of the catalyst and the generated methyl radicals couple in the gas phase to form ethane, which can be further dehydrogenate to ethylene. The catalyst, on the other hand, is reoxidized with O_2 and H_2O is produced as a side product. One plausible reaction mechanism proposed for Mn_xO_y-Na_2WO_4/SiO_2 catalysts is presented in Fig. 1–2. The existence of methyl radicals has been proved by electron paramagnetic resonance (EPR) [62] and recently directly observed with Synchrotron VUV Photoionization Mass Spectroscopy (VUV-PIMS) [63].

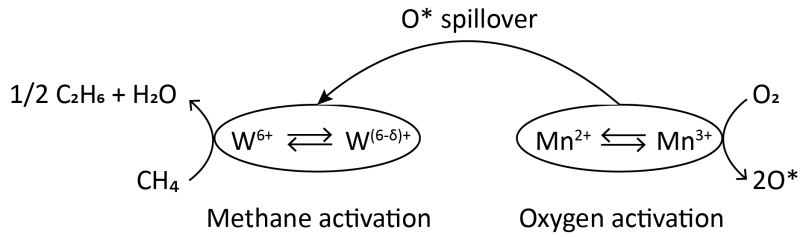

Fig. 1–2. Reaction mechanism on Mn_xO_y-Na_2WO_4/SiO_2 catalysts in OCM reaction.

Based on the H-H mechanism, theoretical calculations have established a correlation between the adsorption energy of methane and its activation energy on oxide surfaces. The results indicated an intrinsic trade-off between activity and C_2 selectivity in the OCM reaction [64]. Surfaces with higher CH_4 adsorption energy favors C-H bond activation, therefore show high activity and CH_4 conversion. On the other hand, these surfaces would also strongly adsorb CH_3 radicals, which facilitate their overoxidation to CO and CO_2, thus lowering the reaction selectivity towards C_2 hydrocarbons.

Some of the preferred properties of a good OCM catalyst are intrinsic basicity, oxygen-anion conductivity and ability to form oxygen vacancies, fast exchange rates between atomic oxygen species on the surface and bulk oxygen-anion vacancies, and low sticking coefficients of CH_3 radicals on the catalyst surface [65]. Most of the OCM catalysts are based on oxides of alkali, alkaline earth, rare earth, and some transition metals. Various promotors and dopants are shown to further improve their activity and selectivity. In addition, catalyst supports are also used to better disperse the active sites and help heat dissipation. As a result, the final catalysts are almost always binary or ternary systems

consisting of host oxides, promotors/dopants, and catalyst supports. Hundreds of catalysts have been tested to date, in which Li/MgO and Mn_xO_y-Na_2WO_4/SiO_2 are two of the most widely studied ones for their outstanding performance with the latter showing better stability over time.

Extensive research has been performed on the Mn_xO_y-Na_2WO_4/SiO_2 catalyst, in which the effect of the preparation methods, elemental concentrations, and the variation of each of its components have been reported. [66] For catalyst preparation, the wet impregnation and the mixture slurry methods are proven to be more efficient in producing high-performance catalysts. [67] As for the catalyst composition, results have indicated that there exist a range of combinations, i.e., 0.4–2.3% for Na, 2.2–8.9% for W, and 0.5–3.0% for Mn, that would allow an optimized C_2 yield. [68] However, in order to achieve the 30% yield target for potential commercial viability, further improvements and modifications to this catalyst system are still needed.

1.6 Summary of Dissertation

Chapter 2 summarizes the main experimental methods that are used in this dissertation for material synthesis and characterization as well as reactor studies. In the material synthesis subsection, experimental procedures for the synthesis of metallic nanoparticles and catalyst supports are provided as well as the fabrication of supported catalysts. In the material characterization part, several key techniques utilized to characterize the synthesized materials are introduced, with emphasize on the working principle and their capability and limitations.

Chapter 3 starts by discussing the synthetic approaches that are developed for Co-based bimetallic nanoparticles, including those of Co-Mn, Co-Cu, Co-Ru, Co-Rh, and Co-Re. The specific procedures for each bimetallic particles differ slightly from one another while being generic and all based on thermal decomposition of metal carbonyls. The structure of the bimetallic nanoparticles is confirmed by transmission electron microscopy (TEM) and a series of in-situ X-ray spectroscopy measurements, including ambient pressure X-ray photoelectron spectroscopy (AP-XPS) and X-ray absorption spectroscopy (XAS), revealed the surface environment of the bimetallic nanoparticles under various conditions relevant to the catalytic measurements. Results from catalytic studies with the synthesized bimetallic catalysts in Fischer-Tropsch reaction are presented and compared to the performance of single metallic Co catalysts.

In Chapter 4, effect of noble metal doping on the performance of mesoporous silica MCF-17 supported Mn_xO_y-Na_2WO_4 catalysts is reported. It is found that doping the Mn_xO_y-Na_2WO_4/MCF-17 catalyst with Pt, Rh, and Ir has little effect on the morphology, surface area, and phase structure but improved the reducibility of tungsten and manganese species. Catalytic study show an enhanced selectivity towards both C_2 and C_3 hydrocarbons with the incorporation of the noble metals, with the Ir-doped catalyst giving the highest C_2 yield.

Chapter 5 describes the synthesis of monodispersed leaf-like manganese–tungsten–oxide (Mn–W–O_x) nanoparticles and hydroxylated hexagonal boron nitride (*h*-BN) nanosheets and their use as novel catalysts in the OCM reaction. Preliminary results showed that when supported on the mesoporous silica support MCF–17, Mn–W–O_x

nanoparticles showed lower activity but higher selectivity towards C_2 hydrocarbons as compared to its impregnated counterpart, although comprehensive comparison between the two catalysts needs further research. The functionalized *h*-BN nanosheets showed good activity in the OCM reaction with moderate selectivity towards C_2 hydrocarbons. In the meantime, the catalyst faced serious deactivation, which was not alleviated by lowering the reaction temperature or the oxygen concentration in the reaction gas feed.

1.7 References

1. Astruc D (2008) In: Astruc D (ed) Nanoparticles and Catalysis. Wiley-VCH, Weinheim, pp 1–48
2. Lloyd L (2011) In: Twigg MV, Spencer MS (eds) Handbook of Industrial Catalysts, 1st ed. Springer US, pp 23–71
3. Somorjai GA, Borodko YG (2001) Catal Letters 76:1–5
4. Grunes J, Zhu J, Somorjai GA (2003) Chem Commun 2257–2260
5. Bell AT (2003) Science 299:1688–1691
6. Daniel MC, Astruc D (2004) Chem Rev 104:293–346
7. Feynman RP (1960) Eng Sci 23:22–36
8. Bardosova M, Wagner T (2015) Nanomaterials and Nanoarchitectures. Springer, Dordrecht
9. Kim JS, Kuk E, Yu KN, Kim JH, Park SJ, Lee HJ, Kim SH, Park YK, Park YH, Hwang CY, Kim YK, Lee YS, Jeong DH, Cho M-H (2007) Nanomedicine Nanotechnology, Biol Med 3:95–101
10. Perugini P, Simeoni S, Scalia S, Genta I, Modena T, Conti B, Pavanetto F (2002) Int J Pharm 246:37–45
11. Popov AP, Priezzhev AV, Lademann J, Myllylä R (2005) J Phys D Appl Phys 38:2564–2570
12. Souza VGL, Fernando AL (2016) Food Packag Shelf Life 8:63–70
13. Bhushan B (2017) Springer Handbook of Nanotechnology, 4th ed. Springer Nature, Berlin
14. Murray CB, Norris DJ, Bawendi MG (1993) J Am Chem Soc 115:8706–8715
15. Rao CNR, Kulkarni GU, John Thomas P, Edwards PP (2002) Chem - A Eur J 8:28–35
16. Haruta M, Tsubota S, Kobayashi T, Kageyama H, Genet MJ, Delmon B (1993) J Catal 144:175–192
17. Haruta M, Yamada N, Kobayashi T, Iijima S (1989) J Catal 115:301–309
18. Min BK, Friend CM (2007) Chem Rev 107:2709–2724

19. Lopez N, Janssens TVW, Clausen BS, Xu Y, Mavrikakis M, Bligaard T, Nørskov JK (2004) J Catal 223:232–235

20. Kumar N, Kumbhat S (2016) In: Essentials in nanoscience and nanotechnology, 1st ed. John Wiley & Sons, Inc., Hoboken, NJ, pp 77–148

21. Murty BS, Shankar P, Raj B, Rath BB, Murday J (2013) Textbook of Nanoscience Nanotechnology, 1st ed. Springer-Verlag Berlin Heidelberg

22. Wang D, Li Y (2011) Adv Mater 23:1044–1060

23. Zaleska-Medynska A, Marchelek M, Diak M, Grabowska E (2016) Adv Colloid Interface Sci 229:80–107

24. Sankar M, Dimitratos N, Miedziak PJ, Wells PP, Kiely CJ, Hutchings GJ (2012) Chem Soc Rev 41:8099–8139

25. Gu J, Zhang Y-W, Tao F (Feng) (2012) Chem Soc Rev 41:8050–8065

26. Morales F, Weckhuysen BM (2006) In: Spivey JJ, Dooley KM (eds) Catalysis. The Royal Society of Chemistry, Cambridge, pp 1–40

27. Hutchings GJ (2001) Catal Letters 75:1–12

28. Ertl G, Lee SB, Weiss M (1982) Surf Sci 114:527–545

29. Strongin DR, Somorjai GA (1988) J Catal 109:51–60

30. Iglesia E, Soled SL, Fiato RA, Via GH (1993) J Catal 143:345–368

31. Diehl F, Khodakov AY (2009) Oil Gas Sci Technol 64:11–24

32. Davis BH (2001) Fuel Process Technol 71:157–166

33. Rofer-DePoorter CK (1981) Chem Rev 81:447–474

34. Chen W, Filot IAW, Pestman R, Hensen EJM (2017) ACS Catal 7:8061–8071

35. Moazami N, Wyszynski ML, Rahbar K, Tsolakis A, Mahmoudi H (2017) Chem Eng Sci 171:32–60

36. Van Santen RA, Ciobîcâ IM, Van Steen E, Ghouri MM (2011) Mechanistic Issues in Fischer-Tropsch Catalysis

37. Jin Y, Sun G, Wang Z, Pan H, Xu L, Xu H, Huang W (2017) J Phys Chem C 121:21535–21540

38. Chen W, Zijlstra B, Filot IAW, Pestman R, Hensen EJM (2018) ChemCatChem 10:136–140

39. Inderwildi OR, Jenkins SJ, King DA (2008) J Phys Chem C 112:1305–1307

40. Ojeda M, Nabar R, Nilekar AU, Ishikawa A, Mavrikakis M, Iglesia E (2010) J Catal 272:287–297

41. Kollár M, De Stefanis A, Solt HE, Mihályi MR, Valyon J, Tomlinson AAG (2010)

J Mol Catal A Chem 333:37–45

42. DRY ME (2002) Catal Today 71:227–241

43. Iglesia E (1997) Appl Catal A Gen 161:59–78

44. Khodakov AY, Chu W, Fongarland P (2007) Chem Rev 107:1692–1744

45. Yang J, Tveten EZ, Chen D, Holmen A (2010) Langmuir 26:16558–16567

46. Bezemer GL, Bitter JH, Kuipers HPCE, Oosterbeek H, Holewijn JE, Xu X, Kapteijn F, Van Diilen AJ, de Jong KP (2006) J Am Chem Soc 128:3956–3964

47. Den Breejen JP, Radstake PB, Bezemer GL, Bitter JH, Frøseth V, Holmen A, de Jong KP (2009) J Am Chem Soc 131:7197–7203

48. Saib AM, Moodley DJ, Ciobîc IM, Hauman MM, Sigwebela BH, Weststrate CJ, Niemantsverdriet JW, Van De Loosdrecht J (2010) Catal Today 154:271–282

49. Tsakoumis NE, Rønning M, Borg Ø, Rytter E, Holmen A (2010) Catal Today 154:162–182

50. Moodley DJ, van de Loosdrecht J, Saib AM, Overett MJ, Datye AK, Niemantsverdriet JW (2009) Appl Catal A Gen 354:102–110

51. Van Berge PJ, Van De Loosdrecht J, Barradas S, Van Der Kraan AM (2000) Catal Today 58:321–334

52. BP (2017) BP Statistical Review of World Energy. BP, London

53. ExxonMobil (2017) 2017 Outlook for Energy: A View to 2040. ExxonMobil, Irving, TX

54. Alvarez-Galvan MC, Mota N, Ojeda M, Rojas S, Navarro RM, Fierro JLG (2011) Catal Today 171:15–23

55. Spivey JJ, Hutchings G (2014) Chem Soc Rev 43:792–803

56. Olah GA (1987) Acc Chem Res 20:422–428

57. Olah GA, Gupta B, Farina M, Felberg JD, Ip WM, Husain A, Karpeles R, Lammertsma K, Melhotra AK, Trivedi NJ (1985) J Am Chem Soc 107:7097–7105

58. Keller GE, Bhasin MM (1982) J Catal 73:9–19

59. Zhu Q, Wegener SL, Xie C, Uche O, Neurock M, Marks TJ (2013) Nat Chem 5:104–109

60. Noon D, Seubsai A, Senkan S (2013) ChemCatChem 5:146–149

61. Song J, Sun Y, Ba R, Huang S, Zhao Y, Zhang J, Sun Y, Zhu Y (2015) Nanoscale 7:2260–2264

62. Lunsford JH (1995) Angew Chemie Int Ed 34:970–980

63. Luo L, Tang X, Wang W, Wang Y, Sun S, Qi F, Huang W (2013) Sci Rep

3:DOI:10.1038/srep01625

64. Kumar G, Lau SLJ, Krcha MD, Janik MJ (2016) ACS Catal 6:1812–1821

65. Zavyalova U, Holena M, Schlögl R, Baerns M (2011) ChemCatChem 3:1935–1947

66. Arndt S, Otremba T, Simon U, Yildiz M, Schubert H, Schomäcker R (2012) Appl Catal A Gen 425–426:53–61

67. Wang J, Chou L, Zhang B, Song H, Zhao J, Yang J, Li S (2006) J Mol Catal A Chem 245:272–277

68. Ji S-F, Xiao T-C, Li S-B, Xu C-Z, Hou R-L, Coleman KS, Green MLH (2002) Appl Catal A Gen 225:271–284

Chapter 2 – Experimental

2.1 Material Synthesis

This part summarizes the key materials used across the entire dissertation and the corresponding preparation methods. For Co based bimetallic nanoparticles, only a general description of the synthesis is provided and detailed parameters are provided in section 3.2.2.

2.1.1 Synthesis of Single Metallic Nanoparticles

Single metallic nanoparticles, including those of Co and Rh, are synthesized to serve as reference catalysts when studying the performance of bimetallic nanoparticles. The synthesis was performed according to previously reported recipes using standard Schlenk techniques under argon atmosphere. 5 nm Co nanoparticles were synthesized via a 'hot injection' method [1]. Briefly, a flask containing o-dichlorobenzene and oleic acid was heated to 178 ºC with an oil bath. After temperature stabilization, a solution of cobalt carbonyl $Co_2(CO)_8$ dissolved in o-dichlorobenzene was quickly injected into the hot solution under vigorous stirring. The reaction mixture was then aged for 20 min prior to being cooled down to room temperature.

5 nm Rh nanoparticles were synthesized with a one-step polyol reduction method [2]. Briefly, rhodium(III) acetylacetonate [$Rh(acac)_3$] and poly-(vinylpyrrolidone) (PVP) were mixed in 1,4-butanediol and evacuated at 140 °C for 20 min under magnetic stirring to remove water and oxygen. The Reaction mixture was then heated to 225 °C at a rate of 10 °C min^{-1} and maintained at this temperature for 2 h under Ar protection before being cooled down to room temperature.

2.1.2 Colloidal Synthesis of Co-M Bimetallic Nanoparticles (M = Mn, Cu, Ru, Rh, Re)

Co-based bimetallic nanoparticles, including those with Mn, Cu, Ru, Rh, and Re are synthesized to study the promotion effect of the second metal to the performance of Co Fischer-Tropsch catalysts. Both the size and composition of the nanoparticles are controlled. The general synthetic approach was developed from the synthesis of well-defined monometallic Co nanoparticles and was achieved through high temperature thermal decomposition of metal precursors under air-free conditions. Briefly, metal precursors, including metal carbonyls and acetylacetonates, were decomposed or reduced, respectively, in solvents with high boiling points such as dichlorobenzene (DCB) and diphenyl ether (DPE). Surface capping agents such as oleic acid and oleylamine were used to modulate the growth of the nanoparticles. Detailed synthesis conditions for each type of bimetallic nanoparticles can be found in section 3.2.2.

2.1.3 Synthesis of Mesoporous Silica Support MCF–17 Using Microemusion Templating Method

MCF stands for siliceous mesostructured cellular foam. Its structure consists of uniform spherical cells with thick walls connected by windows with small size distribution (Fig. 2–1a). The size of its pores can range from 10 nm to 50 nm depending on the synthesis conditions, which is relatively large as compared to other types of mesoporous silica such as SBA–15.

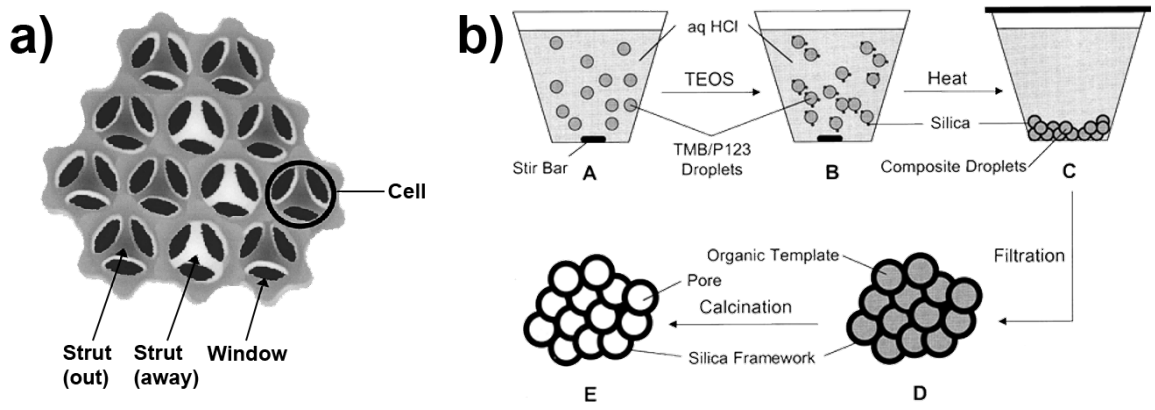

Fig. 2–1. a) Schematic cross section of the pore structure in MCF–17. b) Schematic showing the synthetic procedure for MCF–17. Adapted with permission from reference [3]. Copyright 2000 American Chemical Society

MCF–17 is used as one of the main support materials throughout this dissertation. There are many advantages of using MCF–17 as the catalyst support. Firstly, the large mesopores in MCF–17 provide enough flexibility when incorporating nanoparticles of different sizes. In addition, its chemical inertness and physical strength enable the study of the intrinsic properties of the supported nanoparticle catalysts while offering sufficient stability under reaction conditions. Furthermore, homogeneous distribution of active sites is likely to be achieved thanks to its high surface area and pore volume as well as the ordered pore structure.

The preparation of MCF–17 is achieved using a microemusion templating method (Fig. 2–1b) [3]. In a typical synthesis, a block copolymer Pluronic P123 (poly(ethylene oxide)-block-poly(propylene oxide)-block-poly(ethylene oxide), EO20-PO70-EO20) was firstly dissolved in an aqueous solution containing hydrochloric acid and 1,3,5-trimethylbenzene (TMB), which acted as the organic swelling agent. Under sufficient stirring, tetraethyl orthosilicate (TEOS) was added dropwise and the reaction mixture was aged at 40 ºC for 20 h. The milky solution was then transferred into a polystyrene bottle and heated to 100 ºC to carry out the hydrothermal reaction for 24 h. The mixture was allowed to cool down to room temperature and the white precipitate was collected by simple filtration. After being washed with deionized water and dried sufficiently, the white power was calcined at 550 °C for 4 h in air to obtain the final product.

2.1.4 Fabrication of MCF–17 Supported Metal Nanoparticle Catalysts

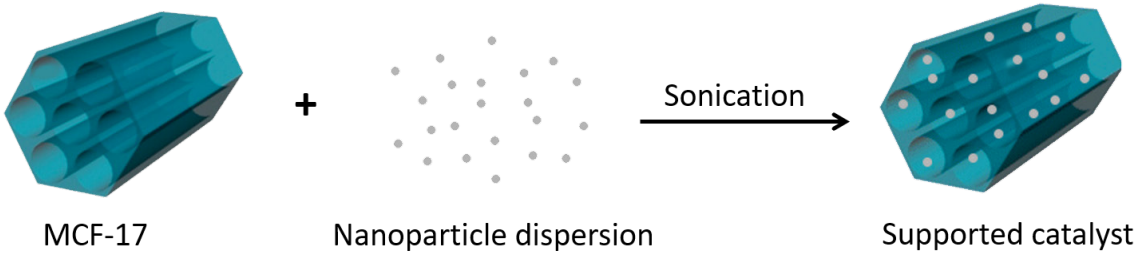

Fig. 2–2. Scheme of the fabrication of MCF–17 supported nanoparticle catalysts

Loading nanoparticles into mesoporous supports such as MCF–17 could help achieve a homogeneous distribution of the active components and greatly enhance their stability. In a typical process, MCF–17 powder and nanoparticle dispersion were mixed together to achieve the desired loading. The resulting mixture was sonicated for an extended amount of time, where nanoparticles would be continuously driven into the pores of the support both due to the agitation induced by sonication and the presence of capillary force inside the pores. The flask being sonicated was shaken repeatedly during the course of sonication in order to achieve a good contact between the nanoparticles and the support material. The supported catalysts were then collected by centrifuging and washed with ethanol and acetone to remove the nanoparticles that are loosely attached on the surface of the support. The final catalysts are dried and stored until further use.

2.1.5 Synthesis of Noble Metal Doped M-Mn_xO_y-Na_2WO_4/SiO_2 (M = Pt, Ir, Rh) Catalysts

The preparation of noble metal doped Mn_xO_y-Na_2WO_4/MCF-17 catalysts is carried out with a sequential wet impregnation method. Briefly, MCF-17 is impregnated with manganese (II) acetate and sodium tungstate and dried at 80 °C overnight. To ensure the same level of manganese and tungsten content, the obtained material was divided into three portions with each being impregnated with a certain metal precursor (rhodium(III) acetylacetonate [$Rh(acac)_3$], platinum(II) acetylacetonate [$Pt(acac)_2$], and Iridium(III) acetylacetonate [$Ir(acac)_2$]) dissolved in chloroform. After sufficient drying, the final product was obtained by calcination at 750 °C in air for 1 h with a heating rate of 1 °C/min.

2.2 Material Characterization

This part gives an overview of the characterization techniques used to study the materials listed in the previous section. General principles of operation are provided as well as their capabilities and limitations.

2.2.1 Electron Microscopy (EM)

2.2.1.1 Transmission Electron Microscopy (TEM)

In TEM, a beam of electrons are accelerated to high energies and hit an ultrathin specimen. The transmitted electrons are used to form an image of the specimen, which is then magnified and focused onto an imaging device for visual inspection with a series of electromagnetic lenses and apertures (Fig. 2–3a). The interaction takes place in many forms (Fig. 2–3b), based on which different imaging and analytical modes are available.

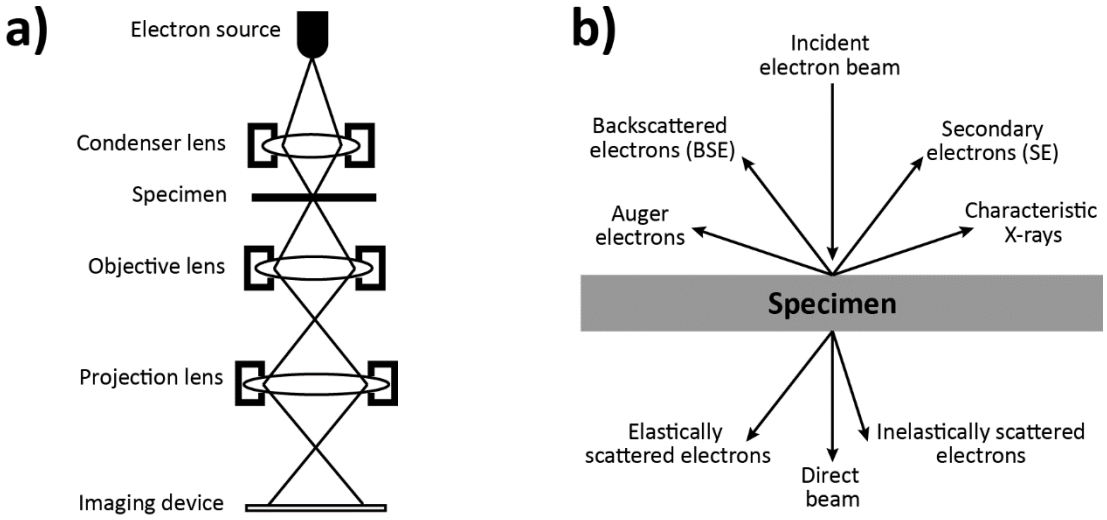

Fig. 2–3. a) Schematic showing the main components and image forming process in TEM. b) Different types of signals generated by the interaction between the electron beam and the specimen in TEM.

The first and the most important benefit of using TEM is its ability to allow us to examine features with sizes that are well below the resolution of a conventional optical microscope due to the substantially shorter de Broglie wavelength of electrons (~ 2.7 pm at an acceleration voltage of 200 kV) than that of the visible light. This is crucial since the understanding of material properties requires imaging at the atomic level.

Depending on the electrons being detected, both bright-field (BF) and dark-field (DF) imaging modes are available. In the BF mode, the direct beams are used to form the image (Fig. 2–3b). Under this mode, thicker regions or regions with a higher atomic number will appear darker as less electrons are directly transmitted in these areas. On the other hand, if the elastically scattered electrons are selected, dark-field (DF) images are formed. Since the cross section of this type of scattering is a strong function of the atomic number Z and the thickness of the specimen, thicker areas with heavy atoms will appear brighter due to stronger elastic scattering. In situations where diffraction contrast is strong and undesired, electrons scattered at very high angles are collected with a high-angle annular dark field (HAADF) detector and used for imaging [4]. The resulting images are called Z-contrast or HAADF images and has the advantage of little or no diffraction effects.

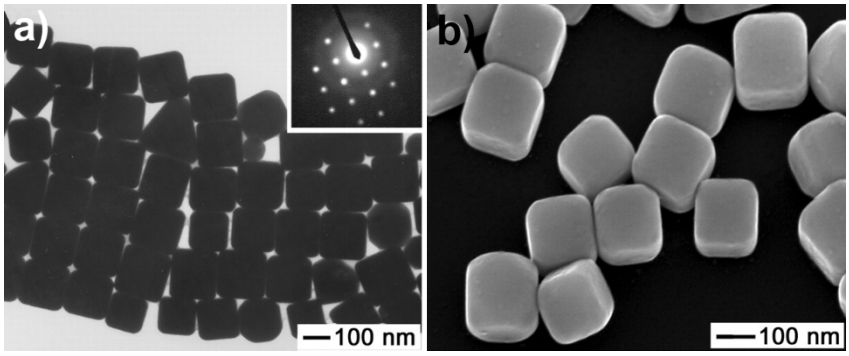

Fig. 2–4. a) TEM bright field (BF) image (Inset: electron diffraction pattern) and b) SEM image of slightly truncated silver nanocubes. Note the substantially more depth of view in the SEM image.

Adapted with permission from reference [5]. Copyright 2002 American Association for the Advancement of Science

Despite being a powerful imaging technique, X-ray energy dispersive spectroscopy (EDS), which is readily available in TEM, provides important information on the nature of the specimen. When performing EDS analysis, TEM is often operated in scanning transmission electron microscopy (STEM) mode, where electrons are focused to a fine spot and scan across the sample area. Sample atoms are ionized by the tightly focused electron beam, where core-level electrons are ejected and holes are created. Electrons from outer levels then fill the holes via a cascade of electron transitions, resulting in the emission of characteristic X-rays. EDS spectra are thus obtained by plotting the X-ray counts versus its energy. Since each element has its unique electron configuration, EDS spectra can be used to identify and quantify different elements contained in the specimen. In addition, by acquiring a spectrum at every pixel in a digital STEM image, elemental mapping of the corresponding area can be obtained, which directly shows the elemental distribution across the sample.

2.2.1.2 Scanning Electron Microscopy (SEM)

SEM also uses electrons to form images of the specimen. As compared to its TEM counterpart, SEM works with lower acceleration voltages and thicker specimens and form 3D images with great depth of view. An example comparing images taken by TEM and SEM is given in Fig. 2–4. In SEM, electrons are focused to a fine spot of a few nanometers and are scanned across the sample in a rectangular raster pattern, similar to the STEM mode in TEM. Various signals created from the interactions between electrons and the specimen are measured, which are then used for image formation and elemental analysis.

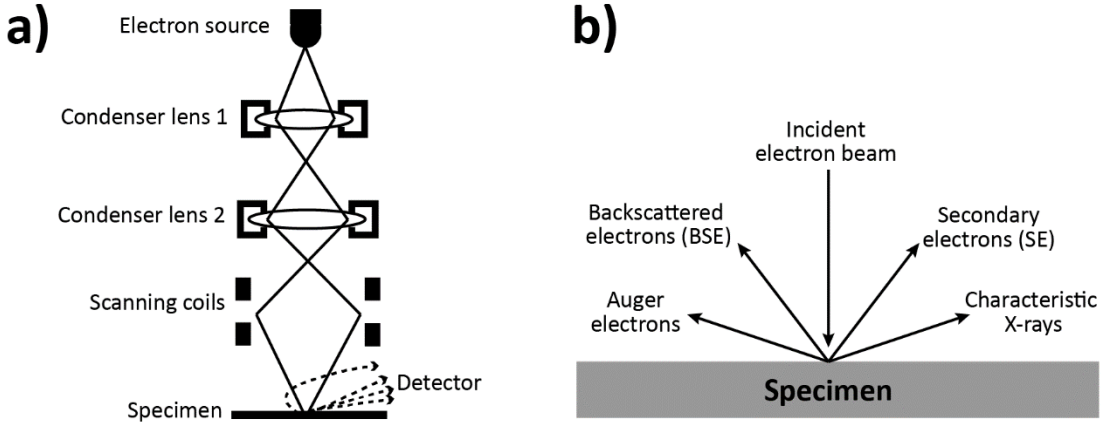

Fig. 2–5. a) Schematic showing the main components and image forming process in SEM. b) Different types of signals generated by the interaction between the electron beam and the specimen in SEM.

There are several imaging modes available in SEM depending on the electron signals being detected. Among them, secondary electrons (SEs) and backscattered electrons (BSEs) are the most important for image recording. By convention, emitted electrons with energy equal to or less than 50 eV are considered SEs, while the energy of BSEs can vary between 50 eV to the energy of the incident beam [6]. Secondary electrons are generated by excitation of electrons from the specimen through inelastic collision with the incident beam or BSEs. Due to the short inelastic mean free path (IMFP) of electrons

in this energy range inside solid materials, SEs from only the surface of the specimen can be detected. In addition, SE yield is highly dependent on the surface tilt of the specimen, making SEs ideal to probe the surface topology. BSEs, on the other hand, are produced through a series of energy loss processes and are scattered through large angles. The maximum information depth of BSEs is of the order of half the electron range. In BSE mode, the contrast is largely affected by the backscattering coefficient, which is highly dependent on the atomic number Z of the specimen. Therefore, phases with different values of Z can be recognized in this mode in addition to the surface topology as BSE emission is also sensitive to the local tilt of the specimen surface [6].

2.2.2 X-Ray Based Techniques

2.2.2.1 X-Ray Powder Diffraction (XRD)

XRD uses the diffraction of X-rays by crystal lattices to gain information on the phase structure of a material. A beam of monochromatic X-ray will be scattered upon interaction with the target material. Depending on the wavelength and incident angle of the X-ray as well as the lattice structure of the target material, interference of the scattered waves will occur on different extents. This process is described by the Bragg's Law (Eq. 2–1), where n is an integer, λ is the characteristic wavelength of the X-ray, d is the interplanar spacing between rows of atoms, and θ is the angle of the X-ray beam with respect to the lattice plane. When the Bragg condition is satisfied, the scattered waves remain completely in phase and constructively interfere, resulting in the maximum intensity of diffraction in that direction (Fig. 2–6a). A diffraction pattern is obtained by recording the intensity of diffraction as a function of θ. By convention, 2θ is used due to the way XRD experiments are performed (Fig. 2–6b). These diffraction patterns serve as chemical fingerprints specific to the materials under investigation. By comparing the measured XRD spectra with the standard patterns in the database, information such as phase composition and lattice orientation can be obtained. All the reference patterns in this dissertation are taken from the PDF database.

$$2d \sin\theta = n\lambda \qquad \textbf{Eq. 2–1}$$

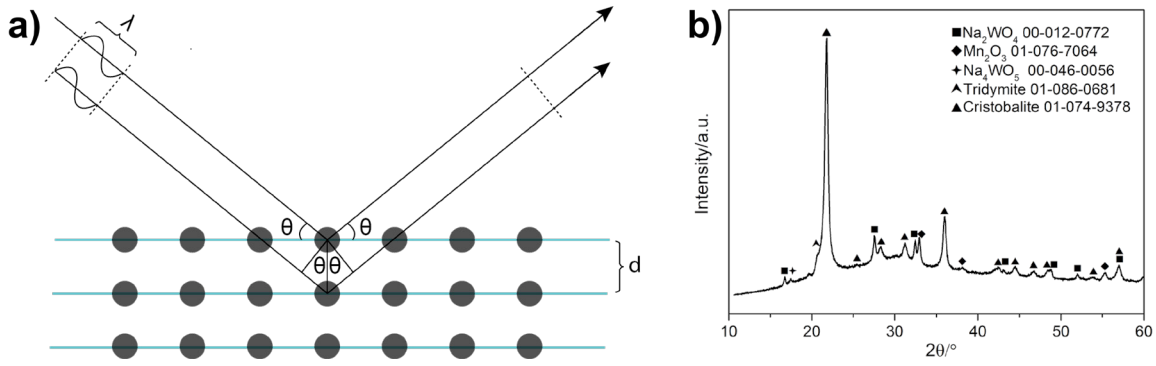

Fig. 2–6. a) Schematic drawing of Bragg diffraction. b) XRD spectrum of fresh Mn_xO_y-Na_2WO_4/MCF-17 catalyst synthesized via a wet impregnation method.

In addition, the peak profile in XRD spectra also contains valuable information. Sherrer equation (Eq. 2–2) relates the average crystallite size to the peak broadening in the XRD spectra [7]. In the equation, θ is the Bragg angle in degrees, λ is the characteristic

wavelength of X-ray in nanometers, β is the broadening of the diffraction peak at half the maximum intensity, often referred to as full width at half maximum (FWHM), in radians, and K is a constant related to the crystallite shape, normally taken as 0.9 for spherical crystals with cubic symmetry [8]. Sherrer equation provides a facile way to assess the crystallite size and can serve complementarily to imaging techniques such as TEM and SEM in some circumstances. It can be used on particles smaller than 100 nm [9], which is quite handy in the field of catalysis considering the fact that a large number of catalysts now consist of nanoparticles in that size range.

$$L = \frac{K\lambda}{\beta \cos\theta} \qquad \textbf{Eq. 2–2}$$

2.2.2.2 X-Ray Photoelectron Spectroscopy (XPS)

Since heterogeneous catalysis is indeed a surface process, surface properties of the catalyst such as its surface elemental composition and oxidation states are valuable information towards understanding its catalytic behavior. X-Ray Photoelectron Spectroscopy (XPS), also known as Electron Spectroscopy for Chemical Analysis (ESCA), is one of the most important techniques to study the catalyst with excellent surface sensitivity.

This technique is based on the well-known photoelectric effect which states that electrons can be ejected from a material when light shines on it (Fig. 2–7). The ejected electrons are called photoelectrons. In XPS, materials under investigation are irradiated with X-rays and the generated photoelectrons are collected and analyzed for their energy and intensity. Plotting the photoelectron counts as a function of its binding energy B.E., as calculated from the incident X-ray photon energy *hv*, the measured kinetic energy of the photoelectron K.E., and the work function of the material Φ_{sample} (Eq. 2–3), yields a typical XPS spectrum.

$$\text{B.E.} = hv - (\text{K.E.} + \Phi_{sample}) \qquad \textbf{Eq. 2–3}$$

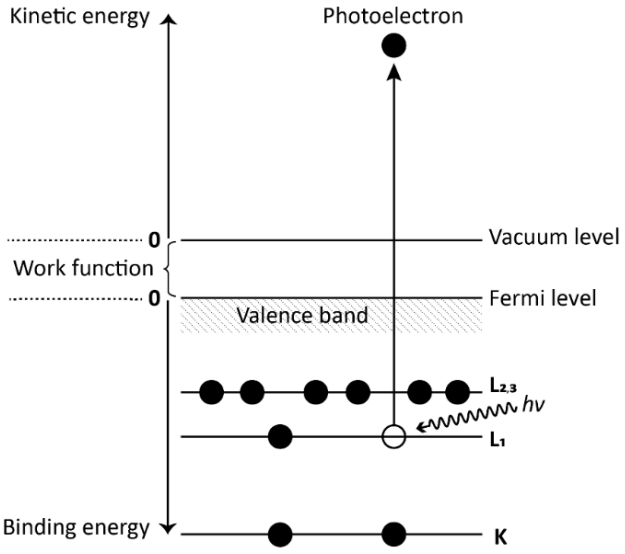

Fig. 2–7. Schematic of the X-ray photoemission process.

Since each element has its own unique electronic structure, the binding energy of the electron serves as its fingerprint and is used for its identification. Compositional analysis is performed by integrating the area under XPS photoemission peaks and correcting it with element-specific sensitivity factors. In addition, since the electron binding energy can be affected by various factors including the oxidation state and coordination environment, a shift in the XPS photoemission peak positions can be used as a sign of changes in the surface chemical environment.

The surface sensitivity of XPS stems from the fact that only photoelectrons generated from the material surface can escape without loss of energy due to the strong inelastic scattering inside the solid. This can be understood using the 'universal curve' of inelastic mean free path (IMFP) of electrons inside solid materials versus their kinetic energy (Fig. 2–8) [10, 11]. Generally, photoelectrons generated in depths greater than three times the IMFP will undergo severe inelastic scattering by the time they reach the surface and barely contribute to the XPS signal. Considering the kinetic energy of photoelectrons in most XPS measurement is typically in the range of a few tens to a few hundreds of eV, the sampling depth of XPS is up to a few nanometers, making it truly a surface sensitive technique.

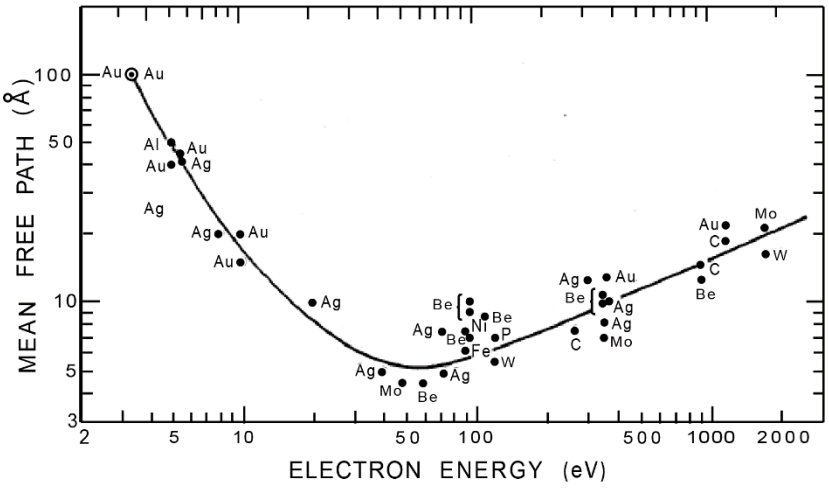

Fig. 2–8. Universal curve of electron IMFPs of various elements as a function of electron energy.

The main components for a typical XPS instrument are X-ray source, vacuum system, and electron energy analyzer. Generally, X-rays are generated by electron bombardment of an anode material, creating holes in the core level which is then refilled by outer shell electrons, thus obtaining characteristic X-ray emissions of the anode material. Commonly used anodes are magnesium and aluminum, with each having its advantages and disadvantages in terms of the photon energy and spectrum resolution.

The reason for the need of vacuum system comes from many aspects. Firstly, X-rays can be absorbed strongly by gas molecules and lead to their ionization, which will result in a significant loss of beam intensity. More importantly, photoelectrons with the kinetic energy typical in most XPS measurements are severely scattered by gas molecules, which would lead to a considerable loss in the signal level. In addition, proper functioning

of electron analyzers also requires vacuum environment. Therefore, most of the XPS experiments are performed under ultra-high vacuum (UHV) conditions.

Hemispherical analyzer is one of the most widely and frequently used electron energy analyzers in XPS studies. It consists of two concentric hemispheres of radii R_1 and R_2, to which potentials are applied to create a controlled electric field between them (Fig. 2–9) [10]. Only electrons with a specific kinetic energy, often referred to as the pass energy, can follow the correct path and reach the detector. A set of electrostatic lenses are used prior to the analyzer to both retard the photoelectrons to the pass energy and focus them to the entrance of the analyzer. XPS spectra are thus obtained by scanning the voltage of the lens system to cover the desired range of photoelectron kinetic energy while fixing the pass energy of the analyzer.

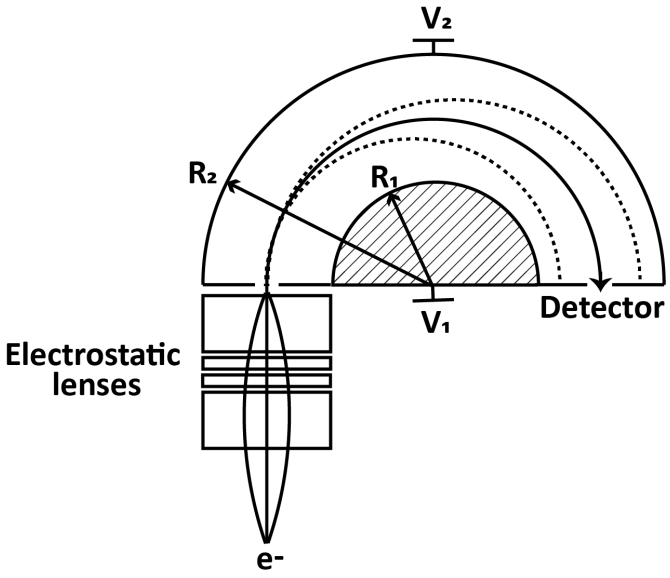

Fig. 2–9. Schematic of the electrostatic lens system and hemispherical electron energy analyzer.

2.2.2.3 Ambient Pressure X-Ray Photoelectron Spectroscopy (AP-XPS)

As is mentioned in the previous section, conventional XPS measurements are carried out under UHV conditions, which hardly resemble the real atmosphere the catalysts experience in a catalytic reaction. Therefore, to follow the true response from the catalyst, measurements being done at reaction relevant conditions are very much desired. To bring this gap, Ambient Pressure X-Ray Photoelectron Spectroscopy (AP-XPS) technique has been developed (Fig. 2–10a).

As compared to the conventional XPS measurement, the development of AP-XPS enables the study of catalyst surfaces under conditions that are more relevant to the real reaction environment (Fig. 2–10b). The use of synchrotron radiation can provide extremely high photon flux, which is several orders of magnitude brighter than lab sources, to ensure high level of excitation and generation of photoelectrons. In addition, the photon energy from a synchrotron source can be varied in a continuous way which enables one to study the depth profile of a material surface. Furthermore, the small beam cross section can substantially improve the spectrum quality, making high resolution imaging possible [12].

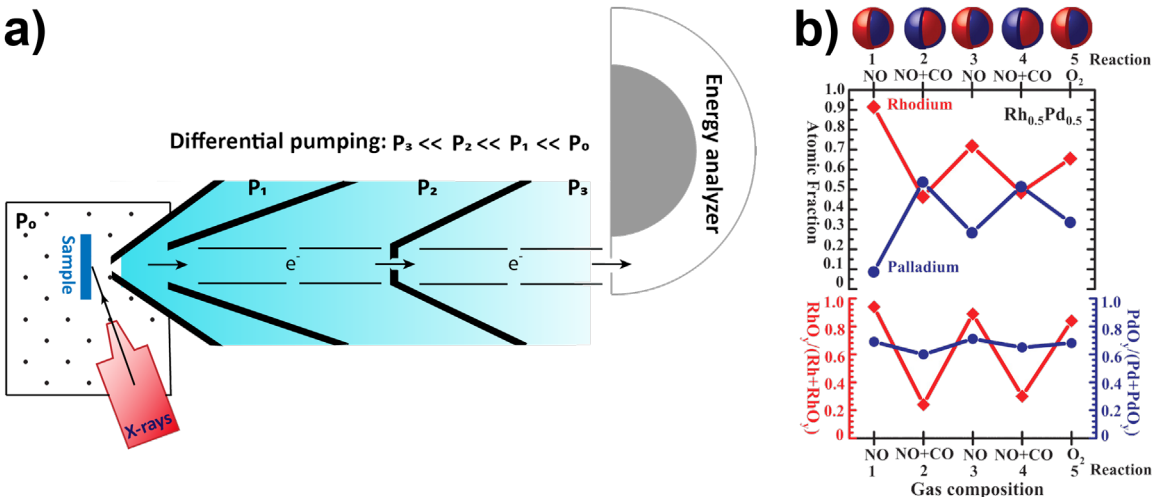

Fig. 2–10. a) Schematic illuctration of the setup of AP-XPS apparatus. b) An example of AP-XPS spetra obtained with $Rh_{0.5}Pd_{0.5}$ nanoparticles under different gas conditions: (Top) Evolution of Rh (Rh^0 + Rh^{2y+}) and Pd (Pd^0 + Pd^{2y+}) atomic fractions at 300°C under oxidizing conditions (100 mTorr NO or O_2) and catalytic conditions (100 mTorr NO and 100 mTorr CO). (Bottom) Evolution of the fraction of the oxidized Rh and Pd atoms under the same conditions as the top part of the figure. Adapted with permission from reference [13]. Copyright 2008 American Association for the Advancement of Science

Because of the use of synchrotron radiation and the presence of gas molecules, special designs have been made to the AP-XPS apparatus (Fig. 2–10a). First of all, since the storage ring where the X-ray beam comes from is kept under UHV, a special window, usually made from Si_3N_4, is used to introduce the beam into and separate it from the working chamber [12]. Secondly, due to the interaction between photoelectrons and gas molecules through elastic and inelastic collisions, the signal level will decrease exponentially as moving way form the surface. Therefore, photoelectrons need to be collected at distances comparable to their mean free path from the surface. In additional, the pressure on the other side of the collection window/aperture need to be reduced effectively so that they can reach the energy analyzer, which is usually kept in UHV conditions. For this purpose, small apertures, usually in conical shapes, are placed close to the surface at a distance equal to or less than the mean free path of the photoelectrons and differential pumping is utilized to reduce the collision rate between the electrons and gas molecules. Modern AP-XPS spectrometer also uses an electrostatic lens to focus the electrons emitted into the differentially pumped chambers, which substantially increases the number of photoelectrons that can be collected [14]. With proper design, the working pressure inside the AP-XPS chamber can reach as high as several Torrs.

All the AP-XPS measurements in this dissertation are performed at the ambient pressure photoemission endstation at Advanced Light Source beamline 9.3.2. A detailed description of the design and specifications of this endstation can be found in the literature [15].

2.2.3 Inductively Coupled Plasma Atomic Emission Spectroscopy (ICP-AES)

Atomic emission spectroscopy (AES) uses the phenomenon that atoms of specific elements emit light of their characteristic wavelength when they are subject to an excitation

source. The elemental specificity comes from the fact that each element has their own unique electronic structure. When energy is absorbed from external sources, electrons in lower orbitals are excited to more energetic levels, creating an excited state of the atom. When returning to the ground state, electrons refill the less energetic level, emitting light with the energy equal to the difference of the orbitals involved in the electronic transition (Fig. 2–11a), which differs for each element and serves as its fingerprint during AES measurements. The quantification in AES is done by measuring the intensity of atomic emission from the sample of interest and compare it to a calibration curve created with a series of samples of known concentration.

Discovered by Bunsen and Kirchhoff back in the mid-18th century, AES has now become a versatile and one of the most frequently used techniques for measuring the concentration of a specific or a group of elements in a sample matrix, especially after the introduction of the inductively coupled plasma (ICP) as the excitation source in the 1970s [16].

The ICP torch consists of three concentric quartz tubes: outer, intermediate, and inner tube (Fig. 2–11b) [16]. A two- or three-turn induction coil wraps around the torch and produces an intense oscillating magnetic field around the coil via an RF generator. With the aid of an electric discharge, the ionization of the carrier gas, typically argon, is initiated and a plasma with a temperature of up to 6000 K is formed around the coil, which is sustained by inductive heating. Due to the extremely high temperature within the coil, cooling gas is flown between the outer and intermediate tube for thermal isolation.

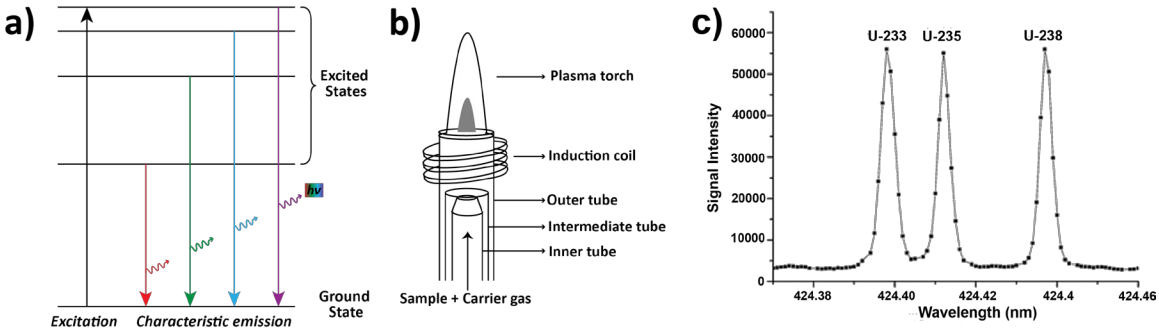

Fig. 2–11. a) Schematic showing the excitation and emission process in AES. b) Schematic showing the structure of the inductively coupled plasma (ICP) assembly. c) An example of a high resolution ICP-AES spectrum of a mixture containing comparable amounts of ^{233}U (424.398 nm), ^{235}U (424.412 nm), and ^{238}U (424.437 nm). Adapted with permission from reference [17]. Copyright 2011 The Royal Society of Chemistry

The use of ICP provides significantly more energy than the conventional flame sources, making it especially powerful in multielement analysis. Other benefits of using this technique include high analytical precision with RSDs easily down to below 1%, low detection limit of 0.1 to 50 ppb for most elements, and high dynamic range of up to six orders of magnitude [16, 18]. With its high precision, robustness, and versatility, ICP-AES is now widely utilized in geochemical analysis, environmental analysis, analysis of biological and medical samples, and many other fields.

2.2.4 N_2 Adsorption

Porous materials are widely used in catalysis as both catalyst support and catalyst itself. Despite the chemical nature, their properties are largely affected by the overall pore structure. Therefore, information such as surface area, pore volume, and pore size distribution are of great importance and need to be routinely measured. Gas adsorption is the main characterization technique that is universally used for this purpose. The adsorption mainly occurs as physisorption via van der Waals forces. Among all the probe gases that are available, nitrogen adsorption at 77K remains the most versatile and widely-used [19].

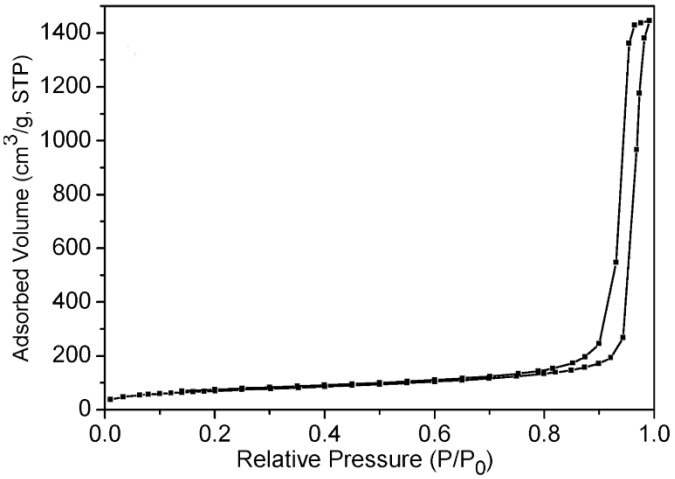

Fig. 2–12. An example of N_2 adsorption isotherm of mesoporous silica MCF-26. Adapted with permission from reference [20]. Copyright 2007 American Chemical Society

N_2 adsorption measures the amounts of N_2 adsorbed on the surface of a porous material as a function of the relative pressure at liquid nitrogen temperature (Fig. 2–12). Using the adsorption isotherm obtained, information such as surface area and pore size can be derived with various empirical models.

The calculation of surface area is commonly based on the well-known BET theory (Eq. 2–4) [21], which describes multilayer adsorption on top of the monolayer assumption originally used in the Langmuir theory. In Eq. 2–4, W is the adsorption quantity, p is the equilibrium pressure, p_0 is the saturation pressure, W_m is the monolayer adsorption quantity, and C is a constant related with the heat of adsorption for the first layer and heat of liquefaction of the probe gas. A plot of $\frac{1}{W[(p_0/p)-1]}$ as a function of the relative pressure $\frac{p}{p_0}$ yields a straight line (In reality, the linear relationship is maintained only in the range of $0.05<\frac{p}{p_0}<0.35$) and monolayer adsorption quantity W_m can be calculated from its slope and intercept. The measured surface area S is then given by Eq. 2–5 [22], where N_A is the Avogadro's number, A is the cross sectional area and M is the molecular weight of the adsorbate molecule.

$$\frac{1}{W[(p_0/\mathrm{p})-1)]} = \frac{C-1}{W_m C}\left(\frac{p}{p_0}\right) + \frac{1}{W_m C} \qquad \textbf{Eq. 2–4}$$

$$S = \frac{W_m N_A A}{M} \qquad \textbf{Eq. 2–5}$$

The analysis of pore size is based on a phenomenon called capillary condensation, where gas condenses in a pore at vapor pressure below the saturation pressure p_0 of the pure liquid. The process is described by the Kelvin equation (Eq. 2–6), which relates the pore size r to the vapor pressure p when condensation occurs. In the equation, γ and V_m stand for the surface tension and the molar volume of liquid nitrogen, respectively. With an appropriate isotherm and the assumption of independent cylindrical pores, the BJH model is one of the most popular ways of deriving the pore size distribution.

$$\ln\frac{p}{p_0} = \frac{-2\gamma V_m}{rRT} \qquad \textbf{Eq. 2–6}$$

2.3 Catalytic Measurements

2.3.1 High Pressure Steady-State Reactor for the Fischer-Tropsch Reaction

The Fischer-Tropsch reaction is carried out in a home-built steady state flow reactor. A scheme of the reactor is shown in Fig. 2–13a. All the gas feeds into the reactor are controlled and monitored by carefully calibrated mass flow controllers (MFCs). A carbonyl trap filled with Cu catalyst is heated and placed at the early stage of the CO line to remove the volatile iron and nickel carbonyls, which would otherwise contaminate the reactor.

The reactor tube is made from 316 grade stainless steel and the catalyst packing is shown in Fig. 2–13b. Catalysts are firstly mixed with SiC for heat dissipation purpose and then loaded into the center of the tube to form a 1 cm catalytic bed. A small amount of sand is packed on both sides of the bed to reduce the reactor empty space and further helps heat dissipation.

The reactor is heated to the desired temperature with an electric tube furnace and the temperature around the catalytic bed is monitored with a K-type thermocouple. Reaction pressure is adjusted in the range of 1-20 bar by a PID-controlled pressure regulator. The reactor effluent first goes through a wax trap, where heavier hydrocarbon with higher boiling point will condense and be removed from the stream, and is then sampled into an on-line Agilent 5975C series GC-MS for analysis. The GC-MS system is equipped with two capillary columns (HP-PLOT Q and HP-PLOT MoleSieve). A thermal conductivity detector (TCD) and a flame ionization detector (FID) equipped with a methanizer are used for the quantification of the reaction products.

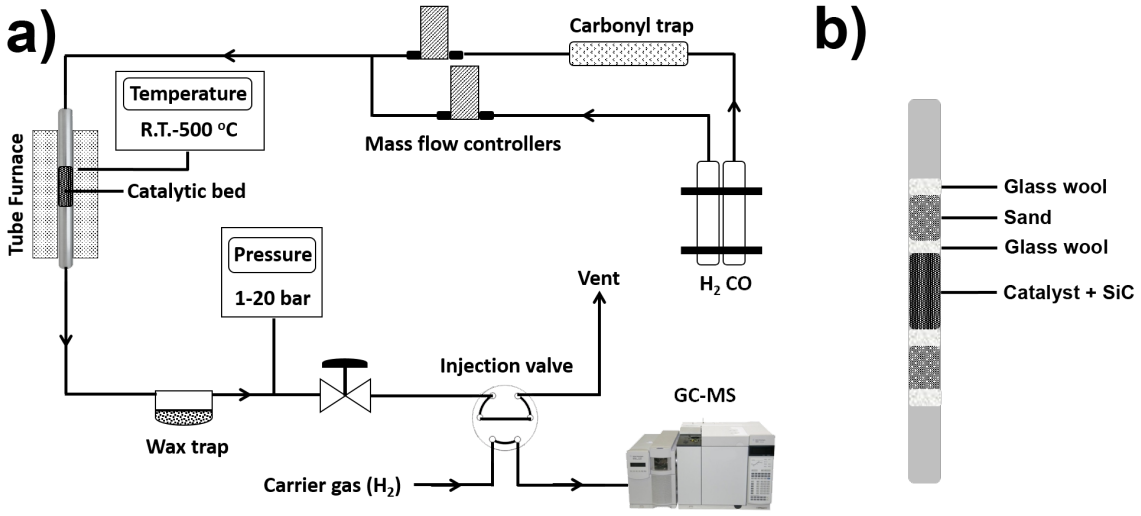

Fig. 2–13. Schemes of a) reactor and b) catalyst packing for the Fischer-Tropsch reaction.

2.3.2 Ambient Pressure Steady-State Reactor for Oxidative Coupling of Methane (OCM)

OCM reaction is performed under atmospheric pressure in a home-built fixed-bed flow reactor similar to the one used for the Fischer-Tropsch reaction. The catalysts are sieved to an average grain size of 150–250 um, mixed with quartz sand to promote heat dissipation, and then packed in the center of a quartz reactor tube. Additional quartz sand is packed on both sides of the catalytic bed to reduce the empty space of the reactor and minimize the undesired gas phase reactions.

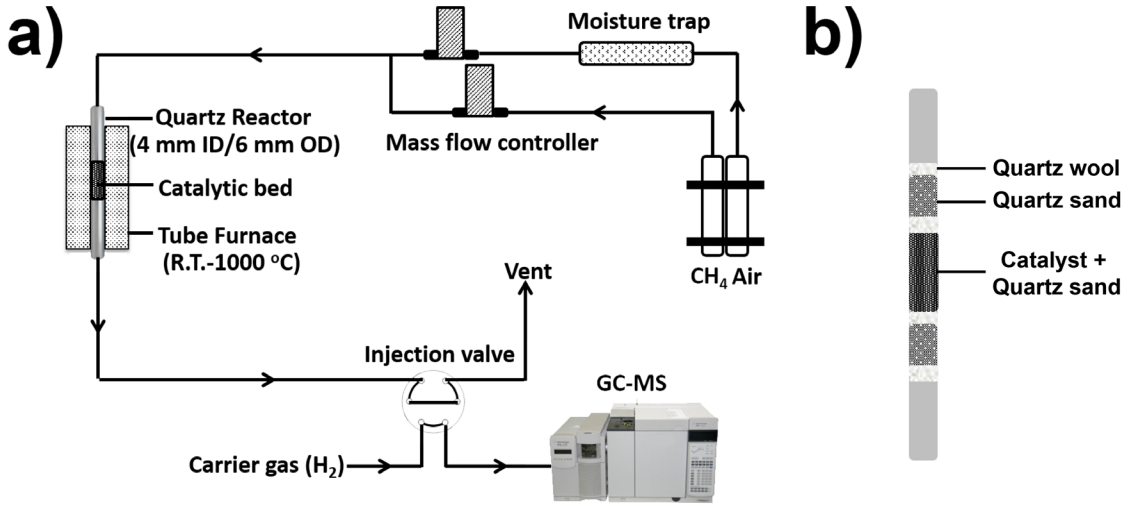

Fig. 2–14. Schemes of a) reactor and b) catalyst packing for OCM Reaction.

High purity methane and synthetic air are fed into the reactor using carefully calibrated MFCs. Moisture traps are installed in the gas lines to reduce the water content. The reactor is heated to the desired reaction temperature with a heating rate of 8 °C/min by an electric tube furnace. Gas lines following the reactor exit are heated to a temperature

above 100 ºC to prevent water condensation. Outlet gas is sampled and separated using an on-line GC–MS (Agilent 7890A-5975C) equipped with two capillary columns (HP-PLOT Q and HP-PLOT MoleSieve). The gaseous composition is analyzed by a thermal conductivity detector (TCD) and a flame ionization detector (FID) detector equipped with a methanizer.

2.4 References

1. Iablokov V, Beaumont SK, Alayoglu S, Pushkarev V V, Specht C, Gao J, Alivisatos AP, Kruse N, Somorjai GA (2012) Nano Lett 12:3091–3096
2. Zhang Y, Grass ME, Habas SE, Tao F, Zhang T, Yang P, Somorjai GA (2007) J Phys Chem C 111:12243–12253
3. Schmidt-Winkel P, Lukens WW, Yang P, Margolese DI, Lettow JS, Ying JY, Stucky GD (2000) Chem Mater 12:686–696
4. Williams DB, Carter CB (2009) Transmission Electron Microscopy-A Textbook for Materials Science, 2nd ed. Springer US, New York
5. Sun Y, Xia Y (2002) Science 298:2176–2179
6. Reimer L (1998) Scanning Electron Microscopy-Physics of Image Formation and Microanalysis, 2nd ed. Springer-Verlag Berlin Heidelberg, Berlin Heidelberg
7. Patterson AL (1939) Phys Rev 56:978–982
8. Langford JI, Wilson AJC (1978) J Appl Crystallogr 11:102–113
9. Monshi A, Foroughi MR, Monshi MR (2012) World J Nano Sci Eng 2:154–160
10. Chusuei CC, Goodman DW (2003) In: Meyers RA (ed) Encyclopedia of Physical Science and Technology, 3rd ed. Academic Press, Cambridge, pp 921–938
11. Seah MP, Dench WA (1979) Surf Interface Anal 1:2–11
12. Salmeron M, Schlogl R (2008) Surf Sci Rep 63:169–199
13. Tao F, Grass ME, Zhang Y, Butcher DR, Renzas JR, Liu Z, Chung JY, Mun BS, Salmeron M, Somorjai GA (2008) Science 322:932–934
14. Bluhm H, Hävecker M, Knop-gericke A, Kiskinova M, Schlögl R, Salmeron M (2007) MRS Bull 32:1022–1030
15. Grass ME, Karlsson PG, Aksoy F, Lundqvist M, Wannberg B, Mun BS, Hussain Z, Liu Z (2010) Rev Sci Instrum 81:53106
16. Rosenberg E, Panne U (2014). In: Gauglitz G, Moore DS (eds) Handbook of Spectroscopy, 2nd ed. Wiley-VCH, Weinheim, pp 507–581
17. Krachler M, Carbol P (2011) J Anal At Spectrom 26:293–299
18. Broekaert JAC (2014) In: Gauglitz G, Moore DS (eds) Handbook of Spectroscopy, 2nd ed. Wiley-VCH, Weinheim, pp 583–645

19. Sing K (2001) Colloids Surfaces A Physicochem Eng Asp 187–188:3–9

20. Han Y, Lee SS, Ying JY (2007) Chem Mater 19:2292–2298

21. Brunauer S, Emmett PH, Teller E (1938) J Am Chem Soc 60:309–319

22. Lowell S, Shields JE, Thomas MA, Thommes M (2004) Characterization of Porous Solids and Powders: Surface Area, Pore Size and Density, 1st ed. Springer Netherlands, Dordrecht

Chapter 3 – Cobalt Based Bimetallic Nanoparticles for the Hydrogenation of Carbon Monoxide: Synthesis, Catalytic Performance, and In-Situ X-Ray Spectroscopy Study

Abstract

General synthesis schemes for size- and composition-controlled bimetallic Co-M (M = Mn, Cu, Ru, Rh, Re) nanoparticles are developed using high temperature, thermal decomposition methods with standard air-free techniques. Characterizations were carried out on the single particle level using scanning/transmission electron microscopy to confirm the bimetallic nature of the nanoparticles. In-situ synchrotron X-ray spectroscopy (ambient pressure X-ray photoelectron spectroscopy (AP-XPS) and X-ray absorption spectroscopy (XAS)) followed the near surface composition and oxidation states of the nanoparticles during oxidative and reductive pre-treatments as well as reaction conditions of Fischer-Tropsch synthesis. The effect of the second metal on the Co reduction and its surface concentration was studied as well as the performance of the catalysts in CO hydrogenation (Fischer-Tropsch process) reaction at industrially relevant conditions of 20 bar and 250 °C to understand the effect of a promoter in intimate contact with Co.

3.1 Introduction

With a growing demand for clean production of fuels, lubricants, and chemical products, along with a shift from petroleum to natural gas based feedstocks, the conversion of single carbon (C_1) molecules to larger hydrocarbon products is an industrially and environmentally important process. Specifically, the reaction of CO and H_2 to form long chain hydrocarbons is known as the Fischer-Tropsch (F-T) synthesis. This reaction has been known for almost 100 years [1–4] and still plays a vital role in the gas-to-liquids (GTL) technology today. The major drawback to F-T synthesis is the lack of control over the product selectivity, and fundamental research in the field of heterogeneous catalysis hopes to overcome this issue.

Iron and cobalt are the two main catalysts used in industrial F-T synthesis applications [5], with cobalt catalysts typically used for their higher chain growth probability and lower operation temperature as compared to iron. To exert control over the product selectivity in F-T synthesis, mechanistic details and surface structures of the active Co catalyst are needed such that an improved catalyst formulation can be made.

A typical heterogeneous catalyst is usually prepared by dispersing the active metal on a high surface area support (SiO_2, Al_2O_3, TiO_2, *etc.*) to obtain better dispersion and high metallic surface area. In the case of Co particles, sizes below 8-10 nm have been shown to decrease in activity in F-T synthesis [6–8], making the catalyst preparation essential to achieve the best catalytic performance. Recent work has shown the difficulty in measuring Co particle size from ensemble measurements [9] and therefore we have chosen to study the F-T reaction by using colloidal synthesis procedures to prepare size-controlled Co nanoparticles which can be imaged before loading into the support [8, 10]. In addition to the Co size, the support can also influence the catalysis – known as the strong metal support interactions (SMSI) [11, 12]. In a previous work form our group, we have found that when the size of the Co nanoparticles are controlled, TiO_2 support enhances the Co activity by almost a factor of 2 compared to SiO_2 supports, even at reduction temperatures which produce mainly CoO instead of Co metal. This TiO_x enhancement was attributed to the decoration of Co by TiO_x species at higher reduction temperatures and CoO wetting the TiO_x surface at lower reduction temperatures [13].

Beyond the Co catalyst and its support, in an industrial setting additional elements are added to boost the Co performance in various ways [14–16]. The secondary species added in addition to the main catalyst are known as *promoters* [17]. Promoters are added for example, to help increase the turn over frequency (TOF) or modify the selectivity towards a certain reaction product.

There can be multiple "modes" of promotion occurring: electronic promotion, structural promotion, and synergistic promotion [18, 19]. *Electronic promoters* modify the band structure of the Co surface, which has far reaching effects, such as changing the adsorption and reaction properties of both H_2 and CO molecules. In order for electronic promotion to be occurring, the Co and promoter must be in direct chemical contact; electronic promoters essentially provide an alternative energetic reaction coordinate for the F-T reaction (bimetallic or alloy vs single metal [20, 21]). *Structural promoters* help to create additional metallic sites for the reaction, thereby increasing the total number of

active sites. Structural promoters typically regulate the interaction between the Co and the oxide support, and can also help to stabilize or prevent deactivation of the catalyst over time. The product selectivity would remain mostly unchanged from a structural promoter (Re, Pt) [22]. Finally, *synergistic promoters* will indirectly influence the Co catalysts. This can take the form of spillover from adjacent sites to create new reaction products not observed on cobalt alone or the promoter element may work in tandem with the Co catalyst.

With the high degree of control afforded by colloidal chemistry techniques, well-defined Co nanoparticles can be produced [23] and here we extend the colloidal synthesis methods to prepare bimetallic Co-M nanoparticle catalysts. The preparation of Co-M bimetallic catalysts allows us to study the effect of a transition metal promoter in intimate contact with Co. In addition, the colloidal method allows for both control of the particle size and composition. These nanoparticle catalysts are model analogues to classical impregnation catalysts, with the advantage being the concentration and distribution of the promoter can be precisely controlled.

Certain parameters need to be identified in order to understand how the addition of a promoter element affects the Co F-T catalysis. The size and structure of the Co particles, the location of the promoter in relation to Co, and the oxidation states of both the promoter and cobalt need to be well-characterized to draw meaningful conclusions from the catalytic studies.

3.2 Experimental

3.2.1 Synthesis of Size-Controlled Co Nanoparticles

Monodisperse cobalt single-metallic nanoparticles were synthesized accoding to a previously reported recipe [23] using standard Schlenk techniques under an argon atmosphere. After evacuation of oleic acid (130 mg, 99% pure) in a 250 ml round bottom flask for 10 min, anhydrous o-dichlorobenzene (99%, DCB, 15 ml) was added under Ar. Under vigorously stirring, the solution was heated to the desired temperature as monitored by a submerged K-type thermocouple. Once reaching the desired temperature, $Co_2(CO)_8$ (430 mg, stabilized with 1-5% hexane) in DCB (3 ml, 0.5 M) was injected quickly into this solution using an air-tight syringe. The brown solution immediately turned black indicating the formation of colloidal particles. This colloidal suspension was then aged for 20 min prior to being removed from heat. Additional DCB (10 mL) was added to the suspension to quench the reaction and cold air was used to help cool down the reaction flask. Absolute ethanol (KOPTEC, 200 proof) was then injected to precipitate the nanoparticles, which were then extracted by centrifugation (4300 rpm). The nanoparticles were re-dispersed in chloroform and stored until further use.

3.2.2 Synthesis of Co-M Bimetallic Nanoparticles

The synthesis of bimetallic nanoparticle is controlled by many aspects and several variables can be adjusted to tailor the reaction process. Despite the intrinsic physiochemical properties (see Table 3–1) and mixing patterns of the two metals, the resulting bimetallic nanoparticles are affected by the reaction temperature and time, use of surface capping agent, types of precursor and their concentration, *etc*.

Table 3–1. Some physicochemical properties of the metals in Co-based bimetallic nanoparticles reported

Metal	Lattice structure pm	Electronegativity	Reduction potential E^0/V [24]	Surface energy[c] J·m^{-2} [25, 26]	Cohesive energy kJ·mol^{-1} [27]	M–M dissociation energy kJ·mol^{-1} [28]
Co	a = 250.7, c = 406.95 (hcp) a = 353.7 (fcc) [29] a = 609 (ε-Co)[a]	1.88	Co^{2+}/Co: -0.28	2.775, 3.035, 3.791 (hcp) 3.23 (fcc 111)	424	≤ 127 50 ± 8 (–Mn) 161.1 ± 16.4(–Cu) 218.0 ± 16.4(–Au)
Rh	a = 380.34 (fcc)	2.28	Rh^{3+}/Rh: 0.758	2.472, 2.799, 2.899 (fcc)	554	235.85 ± 0.05
Mn	a = 891.25 (bcc)[b]	1.55	Mn^{2+}/Mn: -1.185 Mn^{3+}/Mn^{2+}: 1.5415	3.100 (fcc 111)	282	61.6 ± 9.6
Re	a = 276.1, c = 445.6 (hcp)	1.9	Re^{3+}/Re: 0.300	4.214, 4.628, 5.985 (hcp)	775	432 ±3 0
Cu	a = 361.49 (fcc)	1.91	Cu^{2+}/Cu: 0.3419	1.952, 2.166, 2.237 (fcc)	336	201
Ru	a = 270.59, c = 428.15 (hcp)	2.2	Ru^{3+}/Ru^{2+}: 0.2487 Ru^{2+}/Ru: 0.455	3.928, 4.236, 4.856 (hcp) 2.90 (fcc 111)	650	193.0 ± 19.3

[a]While the hcp structure is the most stable phase for bulk Co at room temperature, experimental data show that ε-Co is the most often found crystal structure in nanoparticles prepared by wet chemistry. It consists of a complex cubic primitive structure ($P4_132$), isotypic relative to the beta phase of manganese, with 20 atoms present in the elemental cell [30].

[b]Mn exhibits complex phase structures and only the lattice parameter for the bcc phase is presented here.

[c]Facet order for surface energy: hcp: (0001), $(10\text{-}10)_a$, $(10\text{-}10)_b$; fcc: (111), (100), (110); bcc: (111), (100), (110).

Herein, the synthesis of Co-M (M = Rh, Mn, Cu, and Re) bimetallic nanoparticles is achieved through high temperature, thermal decomposition methods using standard air-free techniques that are developed from the synthesis of well-defined monometallic Co nanoparticles [23,31]. Two types of metal precursors are commonly utilized in this process – metal carbonyls and metal acetylacetonates. Surfactants, such as oleic acid and polyvinylpyrolidone (PVP), are used to control the particle size as well as to improve the stability and dispersity of the nanoparticles.

When carbonyls are used as the metal source, the metals are in zero valent (metallic) states, and the reaction proceeds via either a concurrent or a stepwise decomposition of the two different metal carbonyls of interest [32]. In the case of Co-Rh bimetallic nanoparticles [33], the protocol is developed based on the size-controlled synthesis of monometallic Co nanoparticles using $Co_2(CO)_8$ without trioctylphosphine oxide (TOPO), which was identified as a catalytic poison [23]. In this approach, oleic acid is used as the capping agent to stabilize the nanoparticles, and solvents with moderate to high boiling points, e.g. dichlorobenzene (DCB) or diphenyl ether (DPE), are used to ensure a rapid and complete decomposition of the carbonyl precursors. It is crucial to decompose the precursors such that the correct relative concentrations of the metal species in solution prevent the formation of separated monometallic particles during nucleation and growth. However, $Co_2(CO)_8$ and $Rh_6(CO)_{16}$ have distinctly different thermal stabilities – $Rh_6(CO)_{16}$ exhibits no major weight loss up to temperatures of 145°C [34], while $Co_2(CO)_8$ undergoes facile decomposition under 100°C. To accommodate the difference in the decomposition temperature of the two carbonyl precursors, $Rh_6(CO)_{16}$ is firstly pre-decomposed before $Co_2(CO)_8$ is injected into the hot mixture. This will create the proper relative concentration of Co and Rh, ensuring the formation of bimetallic particles.

In a typical synthesis, hexarhodium(0) hexadecacarbonyl [$Rh_6(CO)_{16}$, Rh, 57–60 %] and oleic acid (99 % pure, 50 μL) were put into a 50 mL three-neck round bottom flask. After evacuation and refill of argon (Ar), anhydrous o-dichlorobenzene (DCB, 99 %, 4 mL) was added into the flask under continuous flow of Ar. The flask was then placed into an oil bath at 180 ºC and kept at this temperature for 2 h under stirring. The temperature of the reaction was monitored by a K-type thermocouple submerged in the reaction mixture. Dicobalt octacarbonyl [$Co_2(CO)_8$, stabilized with 1–5 % hexane, 130 mg] in DCB (1 mL) was then injected quickly into the reaction mixture using a 25 mL gas tight syringe. The colloidal solutions were aged for 10 min before removing from the oil bath. Additional DCB (4 mL) was added into the flask to quench the growth of the nanoparticles and cold air was used to help cool down the reaction flask. After mixing with absolute ethanol (KOPTEC, 200 proof), the nanoparticles were extracted by centrifuging at 4300 rpm for 10 min. Finally, the nanoparticles were re-dispersed and stored in chloroform (Fisher Scientific, ACS grade). This synthesis protocol can be generalized to other Co-M systems: Co-Re, Co-Mn, and Co-Ru bimetallic nanoparticles can all be prepared using this method, although slight modifications such as the change of solvent from DCB to DPE are necessary to account for the variance in the decomposition behavior of different metal carbonyl precursors (see Table 3–2).

If acetylacetonates (acac) are used as the starting material, the synthesis is often carried out in conjunction with reduction to produce nanoparticles in their metallic states. In this case, solvents that can provide reducing environment at high temperatures, such as

oleylamine and ethylene glycol, are often employed. Additional reducing agents can also be used to facilitate the reduction process. Based on a previously reported recipe by Alayoglu *et. al.* [35], 11 nm bimetallic Co-Cu nanoparticles with different compositions were synthesized with $Co(acac)_2$ and $Cu(acac)_2$ as the metal precursors and oleylamine as the reducing agent and coordinating solvent.

In a typical synthesis, $Co(acac)_2$ (Aldrich, ⩾99.0% pure) and $Cu(acac)_2$ (Aldrich, 99.9% pure) were dissolved in oleylamine (5 mL, Aldrich) in a 50 mL round-bottom flask at 50 °C. After evacuation/refilling with Ar for three times, the solution was purged by bubbling Ar for 15 min. The reaction flask was then submerged in a molten salt bath preheated to 230 °C. The solution turned black in approximately 2 min, indicating the formation of colloidal particles. This colloidal suspension was aged at 230 °C for 10 min prior to being removed from heat and allowed to cool down to room temperature naturally. The nanoparticles were precipitated with acetone, collected by centrifugation, and re-dispersed in hexane until further use.

The detailed conditions for the synthesis of Co-M bimetallic nanoparticles (M = Rh, Cu, Mn, Re, Ru) are summarized in Table 3–2.

Table 3–2. Synthesis conditions for Co-M bimetallic nanoparticles

	Precursors	Solvent/ Surfactant	Temp. /°C	Time /min	Morphology	Size /nm	Composition
Co-Rh	$Co_2(CO)_8$[a]	Dichlorobenzene	180	120	Spherical	5.7 ± 0.6	$Co_{98}Rh_2$
	$Rh_6(CO)_{16}$	(DCB), oleic acid	180[b]	10		5.2 ± 0.3	$Co_{90}Rh_{10}$
						4.9 ± 0.4	$Co_{84}Rh_{16}$
Co-Cu	$Co(acac)_2$	Oleylamine	230	10	Spherical	10.6 ± 1.3	$Co_{70}Cu_{30}$
	$Cu(acac)_2$					11.5 ± 1.1	$Co_{50}Cu_{50}$
						10.4 ± 1.8	$Co_{10}Cu_{90}$
Co-Mn[c]	$Co_2(CO)_8$[a]	DCB, oleic acid	181	10	Spherical	3.7 ± 0.3	$Co_{90}Mn_{10}$
	$Mn_2(CO)_{10}$[a]						
Co-Re	$Co_2(CO)_8$[a]	DPE, oleic acid	235	10	Near-	7.1 ± 0.8	$Co_{74}Re_{26}$
	$Re_2(CO)_{10}$		235[b]	10	spherical		
Co-Ru	$Co_2(CO)_8$[a]	DPE, oleic acid	235	20	Spherical	6.6 ± 0.6	$Co_{92}Ru_8$
	$Ru_3(CO)_{12}$		181[b]				

[a]Dissolved in DCB before injection. [b]Injection temperature. [c]$Mn_2(CO)_{10}$ was injected 1 min after $Co_2(CO)_8$ injection.

3.2.3 Preparation of Supported Co, Rh, and Co-Rh Bimetallic Nanocatalysts

The as-synthesized monometallic and bimetallic nanoparticles are supported on MCF-17 type mesoporous silica via sonication. The MCF-17 (BET surface area: ~710 m^2/g) was synthesized in house according to a previously reported method. In a typical process,

MCF- 17 powder was dispersed in chloroform in a 50 mL Erlenmeyer flask before adding nanoparticle dispersions to achieve the desired loading. After being sonicated for 1 h, the suspensions were centrifuged at 4300 rpm and washed with 75 vol% ethanol in acetone for five times. The final catalysts were dried overnight at 100 ^{o}C in the oven and stored in a sealed glass vial until further use.

3.2.4 Inductively Coupled Plasma Atomic Emission Spectroscopy (ICP-AES)

The elemental composition of the Co-Rh bimetallic nanoparticles and the metal loading of the supported catalysts were determined using inductively coupled plasma atomic emission spectroscopy (ICP-AES). ICP-AES measurements were performed on a PerkinElmer ICP Optima 7000 DV spectrometer. Samples for ICP-AES measurements were prepared by digesting the nanoparticles or the supported catalyst in aqua regia and diluting with deionized water. The residual solid was filtered out after centrifugation.

3.2.5 Electron Microscopy Measurements

Transmission electron microscopy (TEM) measurements of the nanoparticles were performed using a JEOL JEM-2100F TEM operated at 200 kV. Scanning transmission electron microscopy-energy dispersive X-ray spectroscopy (STEM-EDS) and scanning transmission electron microscopy/electron energy loss spectroscopy (STEM-EELS) spectra were collected with an INCA EDS spectrometer and a GIF Tridiem EELS spectrometer operating at 200 and 120 kV, respectively. Size distributions were evaluated by counting an assortment of over 200 particles from different TEM images.

3.2.6 Synchrotron Based X-Ray Spectroscopy

All synchrotron based X-ray spectroscopy studies were conducted at the Advanced Light Source in Lawrence Berkeley National Laboratory. The surface composition and oxidation states of the nanoparticles under relevant conditions were determined using Ambient-pressure X-ray photoelectron spectroscopy (AP-XPS) and soft X-ray absorption spectroscopy (XAS) measurements conducted at beamlines 9.3.2 and 8.0.1/6.3.2, respectively. Samples for AP-XPS and XAS measurements were prepared by drop-casting dilute nanoparticle dispersions onto a native SiO_2 terminated n-doped Si wafer.

In the AP-XPS experiments, the nanoparticle samples were measured under ultra-high vacuum (UHV) conditions followed by oxidation (100 mTorr O_2), reduction (100 m Torr H_2), and reaction conditions (CO/H_2 = 2:1, 100-200 mTorr) at various temperatures. In all samples, the Co 2p region was obtained using 940 eV photons for determination of the Co oxidation state on the surface. Rh and Re oxidation states were obtained by fitting the Rh 3d and Re 4f spectra collected at 450 eV and 350 eV, respectively. To obtain relative surface concentrations for the Co-Rh system, the Co 3p and Rh 3d regions were measured at energies of 210 and 450 eV, while for the Co-Mn and Co-Re systems, the Co 3p, Mn 3p, and Re 4f regions were collected at a photon energy of 350 eV. All spectra were corrected with respect to the Fermi edge at their corresponding photon energies. Relative concentrations of each element probed by AP-XPS were calculated by fitting a Shirley background using CasaXPS software and then integrating. The results were corrected for the X-ray photon flux and photoionization cross sections [36] for each core level at the corresponding photon energies.

3.2.7 Catalytic Testing

For catalytic testing purposes, the synthesized nanoparticles were supported in mesoporous silica MCF-17 [37] and tested in a stainless steel fix-bed reactor. Metal loadings are in the range of 4-5 wt%, with the exception of Co-Re having a loading of 7.7 wt%. Approximately 70 mg of the Co-M/MCF-17 catalyst was mixed with 300 mg SiC as a diluent. Before the reaction, catalysts were subjected to an oxidation pretreatment under flowing O_2 at 350 °C for 1 hour to remove the surface capping agent and other carbon impurities, followed by an *in-situ* reduction with H_2 at 450°C for 1 hour. The F-T reaction was carried out at 20 bar with $H_2/CO = 2:1$ and a small amount of Ar was used as an internal standard for GC analysis. Catalysts were aged at 190 °C under the reaction atmosphere for 24 hours or longer until the conversion stabilized. Then the reaction temperature was increased to the target value and the reactant and product concentrations were measured at the outlet of reactor using an Agilent 7890A-5795C GC-MS system. Two capillary columns (HP-PLOT Q and HP-PLOT MoleSieve) were used for proper separation and a thermal conductivity detector and a flame ionization detector were utilized for the detection of reaction products.

3.3 Results and Discussion

3.3.1 Synthesis of Co-M (M = Rh, Mn, Cu, Re, Ru) Bimetallic Nanoparticles

TEM and high-angle annular dark-field (HAADF) images of the synthesized bimetallic nanoparticles are shown in Fig. 3–1. The as-synthesized bimetallic nanoparticles are mostly spherical in shape due to the absence of shape directing agents in the reaction mixture and are in the size range of 4–10 nm. Specifically, Co-Rh bimetallic nanoparticles are generally spherical with three different compositions, i.e. $Co_{98}Rh_2$, $Co_{90}Rh_{10}$, and $Co_{84}Rh_{16}$, as determined from ICP-AES. The average sizes of the nanoparticles are in the vicinity of 5 nm. The spherical, nanocrystalline Co-Cu nanoparticles were also synthesized with three different compositions: $Co_{70}Cu_{30}$, $Co_{50}Cu_{50}$, and $Co_{10}Cu_{90}$. They were 10 nm in size with narrow size distributions. This result was attributed to the use of the high temperature nitrate salt bath, which could provide a rapid and uniform heating environment during the reaction; but with increasing Cu content the size distribution gets larger. STEM-EDS phase map at Co and Cu K lines indicates the existence of Cu-rich cores and Co-rich shells. No stray monometallic nanoparticles were produced through this approach. STEM-EELS also confirms that the Co in the shell is slightly oxidized, whereas the Cu-rich cores remains metallic [38].

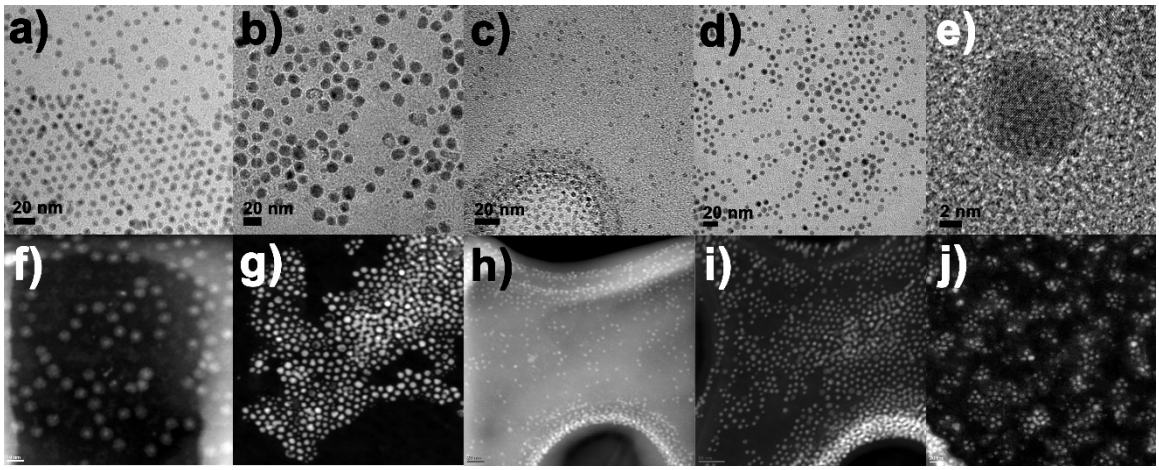

Fig. 3–1. TEM (top) and high-angle annular dark-field scanning transmission electron microscopy (STEM–HAADF) (bottom) images of: **a, f)** Co-Rh, **b, g)** Co-Cu, **c, h)** Co-Mn, **d, i)** Co-Re, and **e, j)** Co-Ru bimetallic nanoparticles.

As for Co-Mn, the bimetallic nanoparticles are about 3.7 ± 0.3 nm in size and their spherical shape could be clearly seen from the TEM images. STEM-EDS spectroscopy measurements on these nanoparticles suggest an average bulk composition of $Co_{90}Mn_{10}$. The near-spherical Co-Re nanoparticles are typically 7.1 ± 0.8 nm in size. STEM-EDS spectroscopy measurements indicate an average composition of 74% Co and 26% Re.

In the case of Co-Ru, STEM-EDS analysis confirmed the formation of bimetallic nanoparticles, which are 6.6 ± 0.6 nm in size and mostly rich in Co. In spite of its low concentration, Ru-rich domains could be clearly observed within the individual nanoparticles, as shown in Fig. 3–2b, yet no monometallic nanoparticles were observed during the characterization. An average atomic composition of $Co_{92}Ru_8$ was obtained by EDS spectroscopy. The morphology, size, and composition of the synthesized nanoparticles are summarized in Table 3–2.

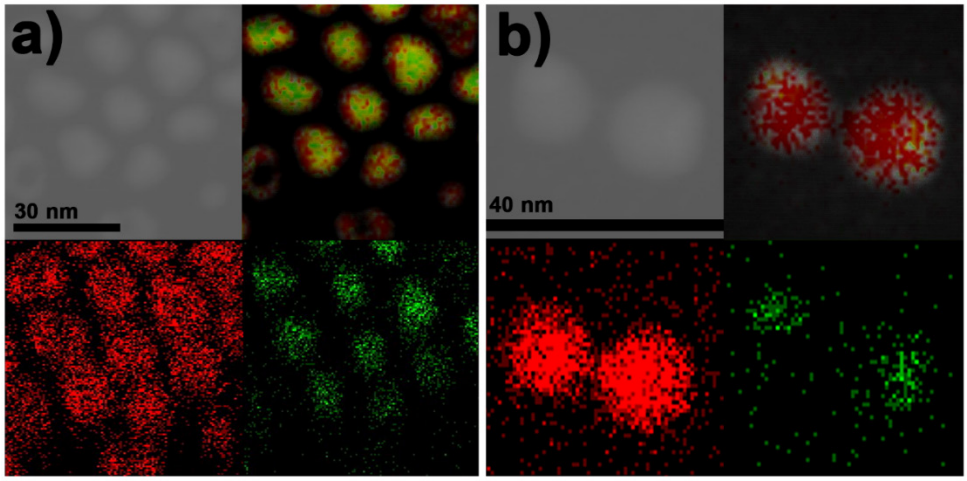

Fig. 3–2. HAADF images and EDS elemental mapping results of a) Co-Cu particles and b) Co-Ru particles; red is cobalt, green is a) Cu or b) Ru.

3.3.2 Synchrotron Based X-Ray Spectroscopic Studies

As compared to the monometallic catalysts, the introduction of a second element alters both the chemical and structural properties of the bimetallic nanoparticles, especially their surfaces. The presence of the second component, due to its difference from Co in reducibility, oxygen affinity, surface energy, electronegativity, and many other physicochemical properties (Table 3–1), will subject the surface of the bimetallic nanoparticles to various dynamic processes, such as surface enrichment of certain components [39]. These effects are more pronounced at elevated temperatures and pressures and also when reactive gasses are present. Therefore, it is crucial that one studies bimetallic nanoparticles under working conditions of the catalysts in order to better correlate the characterization results to the catalytic behavior.

Various spectroscopic techniques have been utilized to study nanoparticle catalysts *in-situ* [40–44]. Among them the synchrotron based X-ray spectroscopies are of great importance in acquiring information on the chemical composition, oxidation states, and coordination environment of both the nanoparticle surface and bulk [45].

Ambient-pressure X-ray photoelectron spectroscopy (AP-XPS) is one of the few techniques that can provide information on the structure and chemical state of the surface of the bimetallic nanoparticles under conditions that approach those of the actual catalytic reaction [46]. In addition to AP-XPS studies, X-ray absorption spectroscopy (XAS) was carried out to provide information on the near surface regions, about 2–3 nm [47]. Complimentary XAS can confirm the oxidation state assignments from AP-XPS and can provide additional information about the local bonding environment. Based on the available X-ray energies of the beamline, various transition metal L edges can be probed for both surface structure (electron yield detection) and bulk structure (fluorescence yield detection) of the bimetallic nanoparticle. The data is grouped by the various bimetallic systems studied. A brief summary of the conditions and photon energies used for data collection can be found in the experimental section.

A summary of surface concentration of Co under various conditions for Co-Mn, Co-Rh, and Co-Re bimetallic nanoparticles as obtained from AP-XPS measurements is presented in Fig. 3–3 followed by a detailed discussion case by case. A complete list of conditions can be found in Table 3–4. In general, the surface concentration of Co on the as-synthesized Co-M bimetallic particles is slightly less than the bulk atomic Co %. Because of the colloidal preparation of the Co-M nanoparticles, a capping agent is left on the surface and is removed by exposure to oxygen [10, 33]. The oxidation treatment also slightly increased the surface Co concentration, which however, remains lower than the bulk Co composition. Upon reduction, surface Co content in both Co-Mn and Co-Rh nanoparticles readily decreases, while Co-Re showed an initial increase in the surface Co concentration. Further elevating the reduction temperature led to a drastic decrease in surface Co for all the bimetallic particles tested. The introduction of reactant gases had little effect on the surface composition with only a slight decrease in Co content for Co-Mn and Co-Rh nanoparticles.

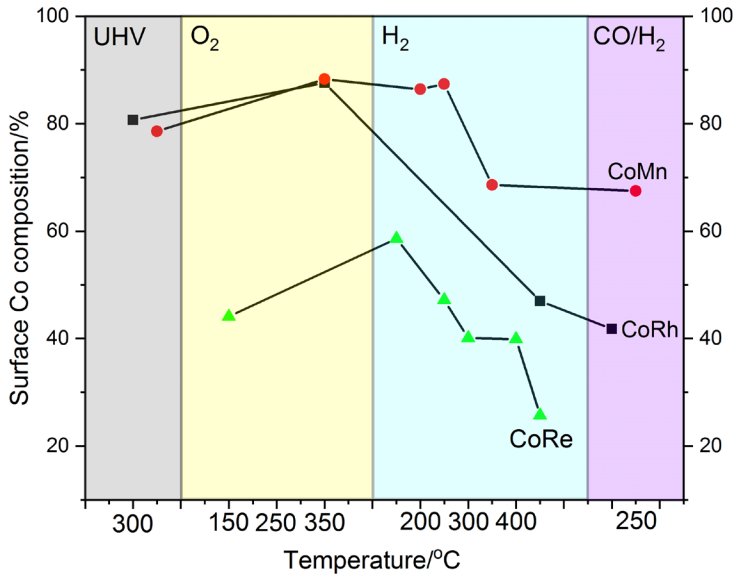

Fig. 3–3. Surface concentration of Co under various conditions as obtained from AP-XPS measurements. The surface concentration of Co on the as-synthesized Co-M (M = Mn, Rh, Re) bimetallic particles is slightly less than the bulk atomic Co %. Treatment with oxygen slightly increased the surface Co concentration, which however, remained lower than the bulk Co content. Reduction treatment led to a decrease of surface Co content in both Co-Mn and Co-Rh nanoparticles, while Co-Re showed an initial increase in the surface Co concentration. Increasing the reduction temperature resulted in a drastic decrease in surface Co for all the bimetallic particles. The introduction of reactant gases had little effect on the surface composition with only a slight decrease in Co content for Co-Mn and Co-Rh nanoparticles.

3.3.2.1 Co-Rh: A Case Study

The surface composition of the Co-Rh bimetallic nanoparticles is determined from the Co 3p and Rh 3d spectra obtained at photon energies of 210 and 450 eV, respectively. The atomic percent of surface Co and Rh on Co–Rh_10 nanoparticles is plotted as a function of different conditions (UHV at 300 °C, O_2 at 350 °C, H_2 at 450 °C, and $CO:H_2$ = 1:2 at 230 °C) and is shown in Fig. 3–4. It can be seen from Fig. 3–4a that the surface of the nanoparticle is Co rich (88 at.%) after the oxidation treatment. However, when reduced with pure H_2 at 450 °C, Rh diffuses out and the surface becomes enriched with Rh (53 at.%). When the reaction gas feed ($CO:H_2$ = 1:2, total pressure is 100 mTorr) is introduced, Rh remains on the surface of the nanoparticles, indicating the existence of a Rh rich shell under reaction conditions.

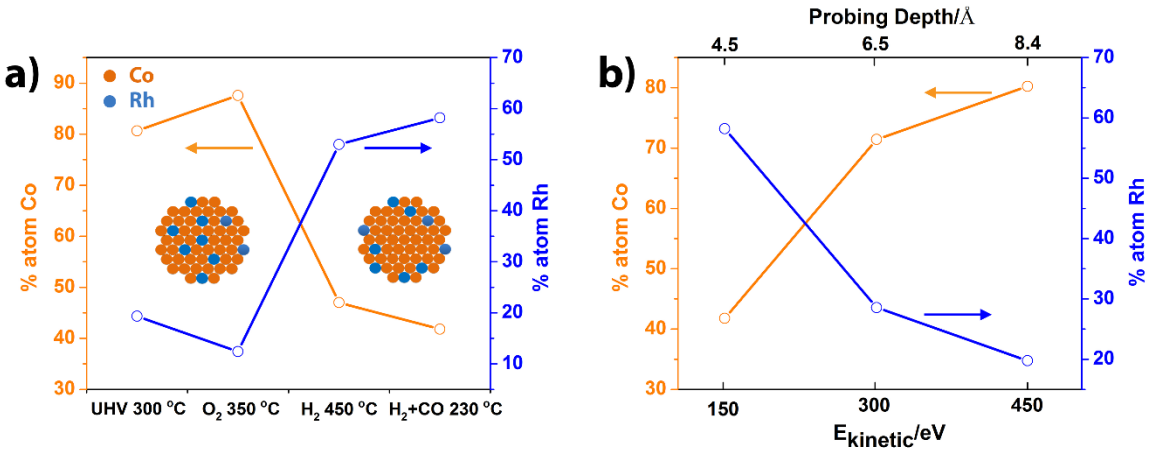

Fig. 3–4. a) Surface compositions of Co-Rh_10 nanoparticles under various conditions showing the formation of a Rh-rich shell under reducing and reaction conditions. The schematic represents the cross section of the nanoparticle. b) Depth profile of surface compositions of Co-Rh_10 nanoparticles under reaction conditions ($CO:H_2$ = 1:2 at 230 ºC) confirming the existence of a Rh-rich shell. The total pressure of the system is 100 mTorr. Penetration depth is obtained from the inelastic electron mean free path calculated using PTT2M formula [48] and relevant kinetic energies of photoelectron. The incident photon energies used for collecting the Co 3p and Rh 3d spectra were: 210 eV, 360 eV, and 510 eV for Co 3p and 450 eV, 600 eV, and 750 eV for Rh 3d level.

The near surface compositions with different probing depths were also studied using AP-XPS thanks to the tunability of the synchrotron X-ray source. For this purpose, the spectra of Co 3p and Rh 3d levels were collected with different photon energies (210, 360, and 510 eV for Co 3p and 450, 600, and 750 eV for Rh 3d level) so that each core level can be probed with a similar kinetic energy of photoelectrons and thus giving a similar probing depth. The AP-XPS depth profile indicates a drastic decrease of Rh concentration from the surface to the bulk. (see Fig. 3–4b) This observation supports the fact that Rh is enriched at the surface of the nanoparticle under reaction conditions.

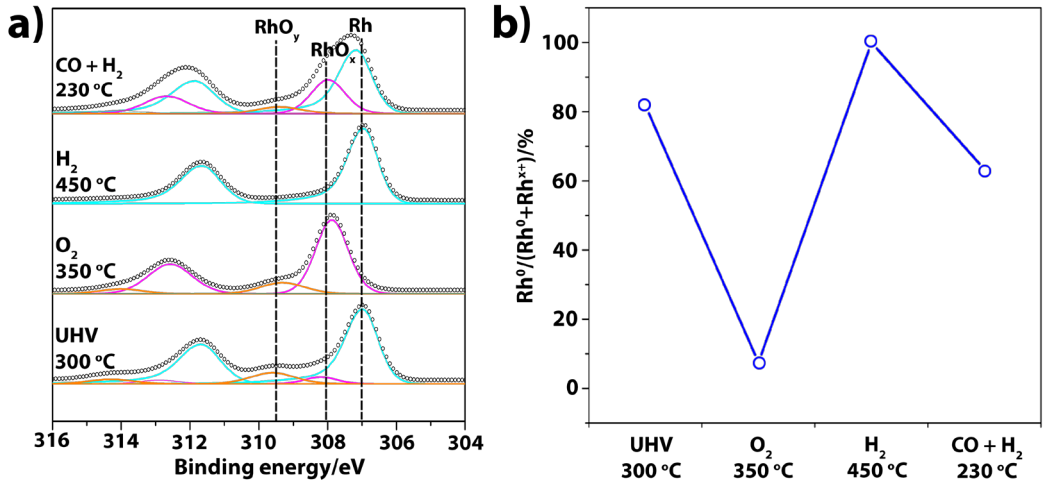

Fig. 3–5. a) AP-XPS spectra of Rh 3d level and b) percentage of metallic Rh on the catalyst's surface under various conditions for Co-Rh_10 nanoparticles. The Rh 3d spectra were obtained with incident photon energy of 450 eV. The total pressure of the system is 100 mTorr.

Rh 3d spectra of Co–Rh_10 nanoparticles under various conditions are shown in Fig. 3–5a. The spectra of Rh $3d_{5/2}$ peak can be deconvoluted into three components: 307.0, 308.1, and 309.2 eV, which correspond to Rh^0, Rh^{1+}, and Rh^{3+}, respectively [49, 50]. Quantification of different oxidation states of Rh is shown in Fig. 3–5b. It can be seen from Fig. 3–5b that Rh was almost fully oxidized and only ~8 % of the total surface Rh is metallic after the oxidation treatment. After treating with pure H_2, the surface Rh was fully reduced to its metallic state. The spectrum under reaction conditions ($CO:H_2$ = 1:2 at 230 ^oC) showed an increase in the amount of the oxidized Rh as compared to the one obtained under pure H_2 condition, with ~63 % of the surface Rh being metallic, which is likely to be caused by the surface O species from the dissociation of CO molecules.

The detailed analysis of the oxidation state using Co 3p spectra is complicated due to the incompletely resolved spin–orbit components of the 3p level. However, information can be gained by comparing with the previously published results. The low olefin to paraffin ratio of our catalyst more closely resembles that of a Co/SiO_2 catalyst reduced at 450 ^oC than a Co/SiO_2 catalyst reduced at 250 ^oC [51]. This ratio is indicative of metallic Co, as the hydrogenation activity of metallic cobalt is higher; in addition, the 450 ^oC reduction temperature was shown to fully reduce Co to Co metal [51].

In summary, the surface composition of Co-Rh bimetallic nanoparticles is very sensitive to oxidation and reduction pretreatments. Reducing environments (H_2 or H_2:CO = 2:1) tend to reconstruct the surface of the nanoparticle to form Rh-rich shells. Under reaction conditions, Rh was shown to be in a mixed oxidation states of Rh^0, Rh^{1+}, and Rh^{3+} with a metal (Rh^0) to oxide (Rh^{1+} + Rh^{3+}) ratio of about 3/2, while Co is believed to be more metallic than oxidized.

3.3.2.2 Co-Re: A Case Study

The as-synthesized Co-Re nanoparticles contain a mixture of Co^0 and Co^{2+}, while the Re in the particles is mostly metallic with a small fraction of Re^{2+}. Upon O_2 treatment at 150 °C, the Co is oxidized to a combination of Co^{2+} and Co^{3+} species (Fig. 3–7a), with CoO content being close to 64% – calculated as % CoO/(CoO +Co_3O_4). The Re in the nanoparticles is also oxidized readily with more than 90% being in its highest oxidation state Re^{7+}. As compared to the bulk composition, the Co-Re system has a much lower surface Co content after the oxidation treatment.

The effect of Re on the reduction and the relative amount of exposed Co surface was studied by increasing the sample temperature under H_2 atmospheres. Upon exposure to H_2 at temperatures as low as 150 °C, Co-Re particles showed an initial increase in the surface concentration of Co, an increase in the amount of CoO (brown peak in Fig. 3–7a) *vs*. Co_3O_4 (blue peak in Fig. 3–7a), and a decrease of highly oxidized Re^{7+} and Re^{6+} species. The increase in the CoO content is also obvious from the much intensified CoO satellite feature (yellow peak in Fig. 3–7a) centered at around 787 eV. It is worth mentioning that only 1 $Re^{\delta+}$ species [52, 53] was found necessary for fitting the Re 4f spectra, but an additional high binding energy peak (46.7 eV, gray peak in Fig. 3–6b) not reported in the literature was needed to complete the fitting. We attribute this peak to a highly oxidized Re species (Re^{X+}) in a different chemical environment than its Re^{7+} (yellow peak in Fig. 3–6b) counterpart in Re_2O_7.

With increasing temperature under H_2, the Re continues to reduce with the major species present being Re^{7+}, Re^{6+} and Re^0; the Re^{4+} and Re^{2+} have small but fairly constant concentrations during the reduction process. At 250 °C, the spinel Co_3O_4 completely disappears, with metallic Co (green peak in Fig. 3–7a) appearing along with a corresponding metallic Re peak (Fig. 3–6a). The amount of surface Co continues to decrease as the temperature is increased for the Co-Re system: at 150 °C under H_2 there is 59% surface Co, but at 450 °C the amount of Co has decreased to 26%. Co oxidation state also decreases as the reduction temperature is raised, which is evidenced by the increase of the metallic Co peak at the expense of the CoO content and the weaker satellite feature associated with CoO at higher reduction temperatures. At 450 °C, the Co is fully reduced and the majority of Re is metallic with decreasing concentrations of Re^{2+}, Re^{4+}, and Re^{6+}.

In summary, as in the case of Co-Rh, Co-Re bimetallic nanoparticles readily reconstruct upon oxidation and reduction treatments. Surface Co content exhibits a slight initial increase when switching from O_2 environment to H_2 atmosphere, but showed drastic decrease when the reduction temperature is further raised. Oxidation state analysis confirms a facile reduction of Co with the presence of Re, with the disappearance of Co_3O_4 and appearance of metallic cobalt component at temperatures as low as 250 ºC.

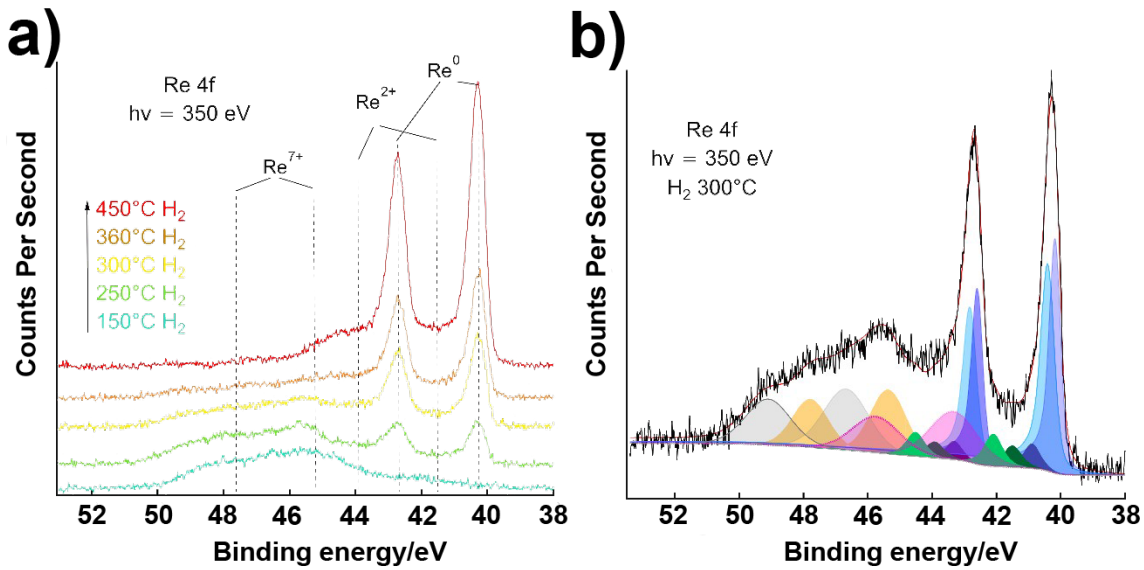

Fig. 3–6. a) Re 4f spectra under 100 mTorr H_2 and increasing temperature (bottom to top) and b) example Re 4f peak deconvolution; $4f_{7/2}$ and $4f_{5/2}$ peaks are the same color, split by 2.42 eV. Table 3–3 lists the binding energy, fwhm values, and other fitting parameters.

Table 3–3. Rhenium AP-XPS fitting parameters

	Re^0_a	fwhm	Re^0_b	fwhm	$Re^{\delta+}$	fwhm	Re^{2+}	fwhm	Re^{4+}	fwhm	Re^{6+}	fwhm	Re^{7+}	fwhm	Re^{X+}	fwhm
$4f_{7/2}$	40.32	0.35	40.41	0.47	40.78	0.65	41.49	0.69	42.20	0.62	43.33	1.5	45.19	1.7	46.7	1.8

$Re^0_{a,\,b}$ have Doniach-Sunjic lineshapes (0.1, 300) [54]; the rest of the Re peaks have Gaussian-Lorentzian product lineshapes GL(70); the $4f_{5/2}$ peaks were restricted to a 2.42 eV spin-orbit splitting, equal fwhm, and area constraint of 4:3 for $4f_{7/2}$: $4f_{5/2}$ [55]; the binding energy positions were taken from literature [52–54].

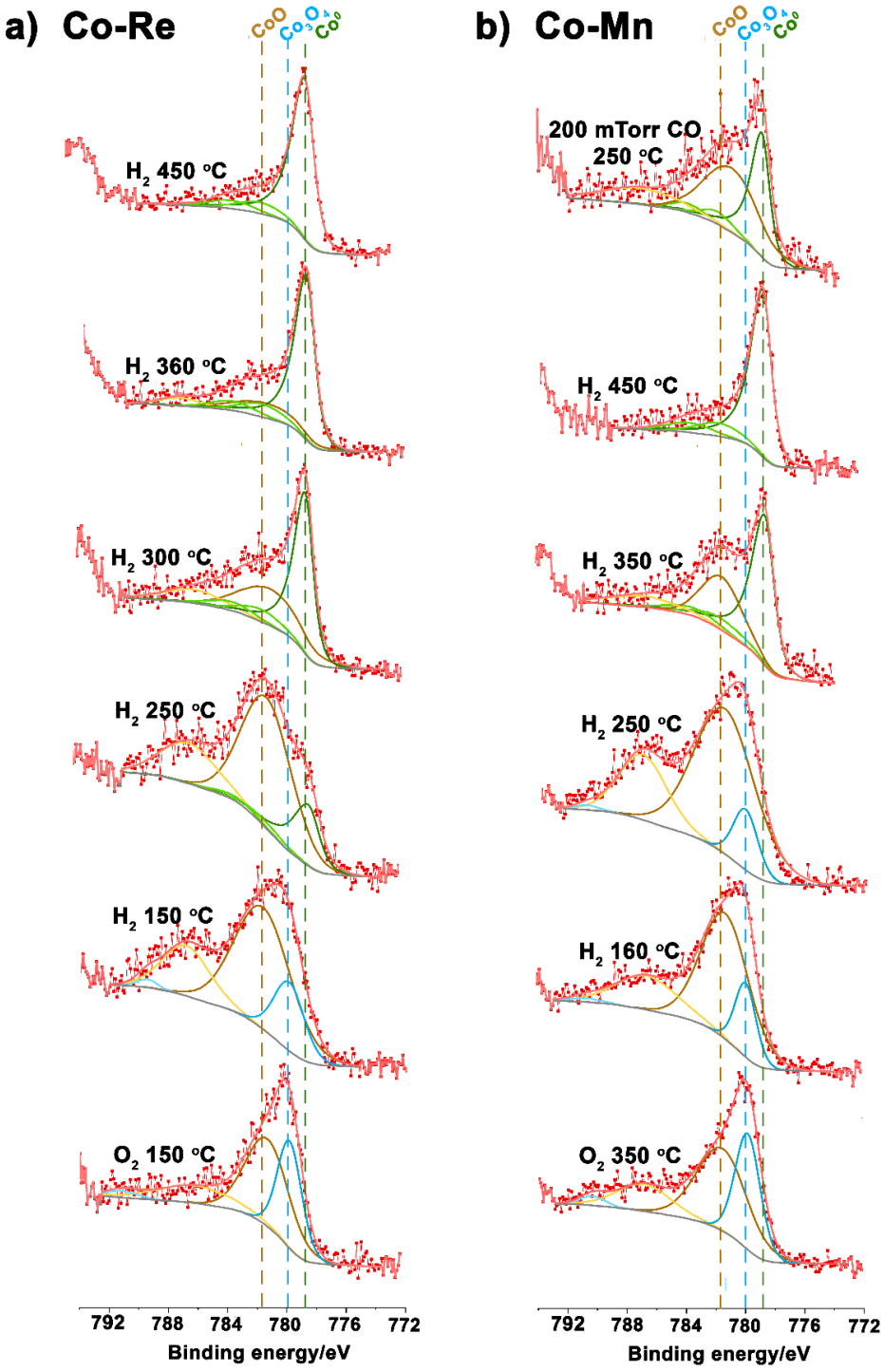

Fig. 3–7. Co 2p spectra for a) Co-Re and b) Co-Mn bimetallic nanoparticles under different conditions. Co^0 plasmon loss peaks are shown in light green and CoO/Co_3O_4 satellite features are shown in light yellow/light blue, respectively. GL (30) lineshapes were used for the fittings except for the metallic Co peaks, where a LF (1.3, 2.5, 100, 10) lineshape was used to account for the asymmetry of the metallic Co peak [56].

3.3.2.3 Co-Mn: A Case Study

The as-synthesized Co-Mn nanoparticles are found to have a mixture of Co^0 and Co^{2+} species, which is similar to Co-Re nanoparticles. The surface concentration of Co is slightly less than the bulk atomic Co %, as is the case for Co-Rh nanoparticles. When subject to oxidation treatment, both Co^{2+} and Co^{3+} species are formed with ~64% CoO – calculated as % CoO/(CoO +Co_3O_4), while Mn^{3+} was shown to be the dominant oxidation state for Mn.

With regards to the reduction treatment, the Co-Mn system is more stable under H_2 than the Co-Re, as no major changes to the particles occur until 350°C. Upon switching to reducing atmospheres (H_2 160 °C), the percentage of CoO increases to 83% at the expense of Co_3O_4. Further increasing the temperature leads to higher percentages of CoO, but no metallic Co is observed until reaching 350 °C (Fig. 3–7b). At 350 °C the surface is partially reduced to ~ 65% Co^0 and reaches 100% Co^0 at 450 °C. However, once the Co begins reducing to Co^0, the surface concentration begins to decrease. The Mn^{3+} species also show no signs of change until 350 °C, at which the Mn $2p_{3/2}$ peak shifts to lower binding energy and the Mn^{2+} satellite [57] becomes visible (Fig. 3–8). Due to the low amount of Mn present, XAS is preferred over AP-XPS to determine the concentration and relative types of Mn species present in the nanoparticle samples (see subsequent paragraphs). After the reduction, the Mn surface concentration has increased from 12% under O_2 to ~ 31% under H_2.

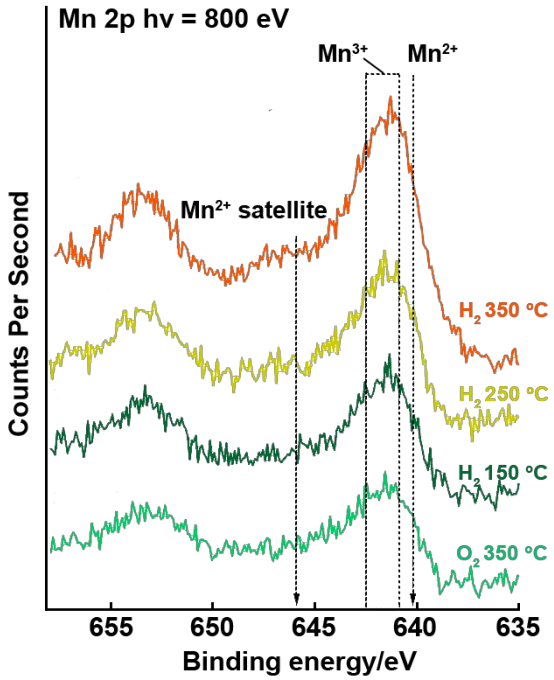

Fig. 3–8. AP-XPS spectra of the Mn 2p region. Spectra were obtained with an incident photon energy of 800 eV. Dashed lines indicate the approximate peak positions of the various metallic and oxidized species.

Subsequent introduction of the reactant gas after the reduction treatment gave similar surface compositions for Co-Mn as those obtained under H_2 at elevated

temperatures. The Mn concentration is 32% under 200 mTorr CO at 250 °C, which is a 1% increase from the 350 °C H_2 condition. Metallic Co also decreases upon exposure to CO going from 65% Co^0 to 42% Co^0, as shown in Fig. 3–7b.

In addition, XAS measurements of Co-Mn nanoparticles followed both the Mn $L_{3,2}$ and Co $L_{3,2}$ edges, which provide important information in identifying the structure and oxidation states of Mn and Co present on the surface of the Co-Mn particles. Fig. 3–9 shows representative L edge spectra of Co and Mn.

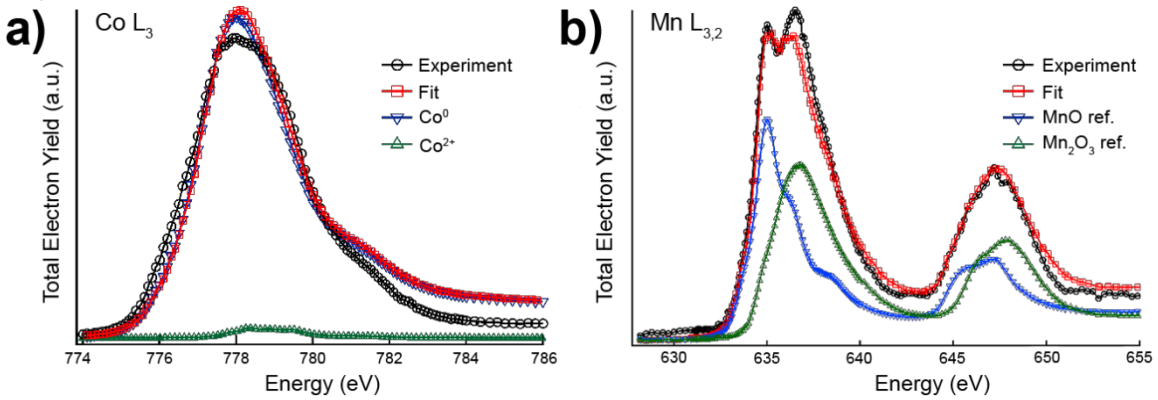

Fig. 3–9. XAS of Co-Mn nanoparticles showing: a) Co L_3 TEY spectra and b) Mn $L_{3,2}$ TEY spectra along with their respective reference materials (triangular markers) and linear combination best fit (squares markers, red).

A linear combination of reference materials was used to fit the near edge XAS spectra; the oxidation state of cobalt was generally greater than 90% Co^0, with the remaining Co as Co^{2+}. The Mn spectra (Fig. 3–9b) could be deconvoluted as 56% MnO and 44% Mn_2O_3. It should be noted the complimentary nature of the XAS and AP-XPS data; Mn 2p XPS spectra have complex peak deconvolutions and satellite features, whereas the XAS linear combination fitting of reference compounds accurately reproduces the experimental Mn $L_{3,2}$ data with much higher confidence levels.

In summary, Co-Mn bimetallic system is generally less susceptible to reconstructions and change in oxidation states induced by oxidation and reduction treatments. In addition, the change in Co surface concentration is found to coincide with the reduction of Co to its metallic state, which takes place at temperatures as high as 350 ^oC. According to AP-XPS results, the surface of the nanoparticles remains enriched of Co under both the pretreatment and reaction conditions.

A complete list of surface concentration and oxidation states of Co under various conditions (UHV, H_2, O_2, and CO+H_2) for the Co-M bimetallic systems discussed above is summarized in Table 3–4.

Table 3–4. Surface concentrations and oxidation states of Co under various conditions for different Co-based bimetallic nanoparticles

		$Co_{90}Rh_{10}$ / %		$Co_{90}Mn_{10}$ / %			$Co_{74}Re_{26}$ / %		
Atmosphere[a]	Temp. / °C	Co/(Co+M)	Co^0	Co/(Co+M)	Co^0	$CoO/(CoO+Co_3O_4)$	Co/(Co+M)	Co^0	$CoO/(CoO+Co_3O_4)$
UHV	300	80.7	-						
	350			78.6	93.3	100	-	76.0	100
O_2	150						44.1	0	64.3
	350	87.6	-	88.3	0	64.0			
H_2	150						58.6	0	83.1
	160			86.4	0	82.7			
	250			87.4	0	89.8	47.2	21.6	100
	300						40.1	60.2	100
	350			68.6	65.2	100			
	360						39.9	80.0	100
	450	47.0	-	-	1	-	25.7	1	-
CO[b]	250			67.5	42.3	100			
$CO+H_2$[c]	230	41.8	-						

[a]The total pressure in the AP-XPS chamber is 100 mTorr, if not otherwise specified.
[b]The total pressure is 200 mTorr.
[c]$CO:H_2$ = 1:2

3.3.3 High Pressure Reactor Studies

The synthesized bimetallic Co-M nanoparticles were tested for the F-T reaction to ensure the synthesis produced real, active Co catalysts which can be considered model analogues of bimetallic impregnation catalysts. The Co-M nanoparticles were supported on MCF-17, oxidized at 350 °C, reduced *in-situ* at 450 °C, and aged for 24 hours at 190 °C prior to collection of any steady state data. All the metal loadings are between 4-5 wt%, with the exception of Co-Re which has a loading of 7.7 wt% due to the much larger atomic mass of Re versus Co.

3.3.3.1 Reaction Activity

Fig. 3–10 shows the turn-over frequency (TOF) of the Co-M bimetallic catalysts plotted against the nanoparticle size. As has been discussed in section 1.4 of Introduction, the intrinsic activity of Co F-T catalyst is size-dependent with the optimum particle sizes being around 8–10 nm for most supported Co catalysts. Larger particles show no change in the intrinsic reaction rate and smaller particles display lowered activity. Therefore, any comparison with pure Co catalysts and discussion on the promotion effect must be deconvolute the potential size effect. For this purpose, TOFs of both pure 5 nm and 10 nm Co (black filled dots) are given as reference states for bimetallic nanoparticles with similar sizes. In addition, AP-XPS Co surface area after reduction has been used to normalize the bimetallic reaction rate data (except Co-Cu, see below for discussion).

It is immediately evident that the Co-Rh particles seem to have positive enhancements in the catalytic activity, as well as the Co-Mn catalyst. Interestingly, Co-Re shows a marked decrease in activity; contrary to many reports in literature of gains in activity [16, 58], the Co-Re nanoparticles are 2-3 times less active than similar sized pure Co particles. Further microscopic evidence of the spent catalysts is needed to determine if the Re or remaining Re^{2+} is blocking Co sites, if the Re has helped to disperse and stabilize ultra-fine Co particles, rendering them less active [59, 60], or in the absence of those factors that this is an electronic effect due to the Re additive in the nanoparticle. The loss of activity of the Co-Re system may be related to the Co:Re ratio; the literature sources mentioned above use Co:Re ~ 100, a much smaller concentration of Re than used here. The Co-Cu TOFs are normalized by the surface sites of pure Co particles of the same size (10 - 11 nm) as it is known that Co and Cu are not miscible [61] and have been shown to phase segregate during pretreatments [35]. When normalized in this way, the Co-Cu catalysts are less active than their pure Co counterparts by almost 2 orders of magnitude; this is most likely caused by aggregation of Co into larger particles or by covering of Co by the Cu species [62].

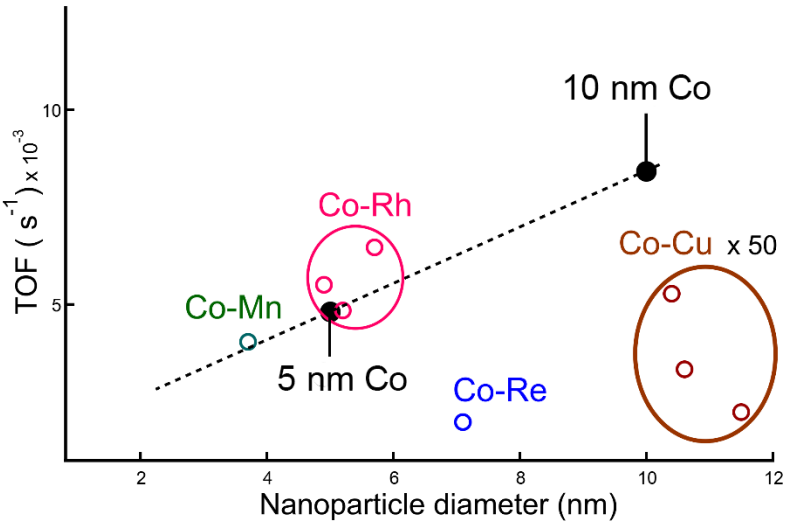

Fig. 3–10. TOF of the bimetallic Co-M nanoparticles plotted as a function of nanoparticle size. The dotted black line is the activity of pure Co nanoparticles in that size regime (black filled dots) [8].

3.3.3.2 CH_4 and C_{5+} Selectivity

The selectivities for CH_4 and C_{5+} of the various Co-M bimetallic catalysts generally resembles those of pure Co with slightly higher selectivity towards C_{5+} products, indicating less pronounced promotion effect of the second metals on the reaction selectivity. C_{5+} is the major product constituting more than 90% of the total reaction products. The C_{5+} selectivity also follows the observed trend for Co with an inverse relationship between CH_4 selectivity and C_{5+} selectivity, as shown in Fig. 3–11. This is in agreement with a variety of literature sources [63, 64]. All the bimetallic nanoparticles seem to obey this inverse relationship, indicating methanation pathways do not seem to be affected by the intimate contact of the promoter and Co. However, a true selectivity comparison here is difficult, owing to the difference in nanoparticle sizes and conversion levels. Future studies will need to address selectivity comparisons and deactivation effects, which are not discussed here.

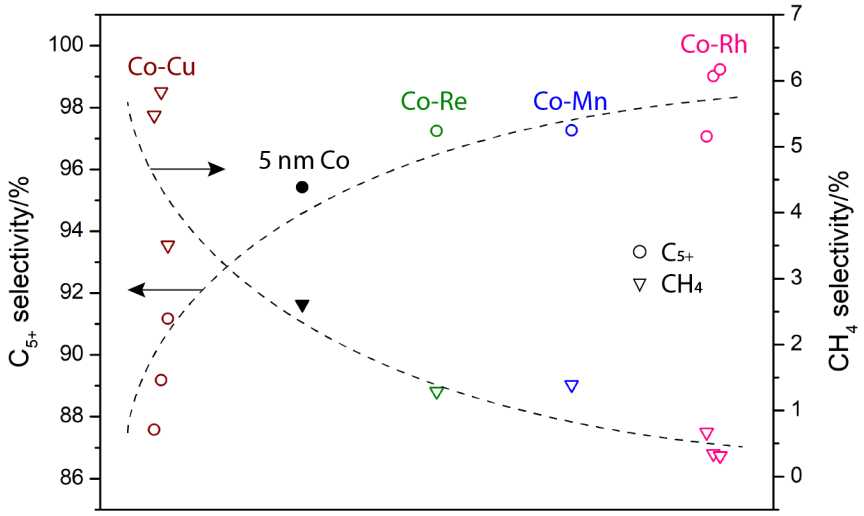

Fig. 3–11. Correlation between C_{5+} selectivity and CH_4 selectivity. All selectivity values are reported as C atom%. The dashed line is a best fit of the data, but is only meant to demonstrate the general trend.

3.3.3.3 Production of Alcohols

Aside from C_{5+}, the alcohol production of Co-M bimetallic catalysts is modified with certain metals when compared with pure Co. Both the Co-Rh and Co-Cu nanoparticle composition series produce longer chain primary alcohols (ROH) compared to their pure Co counterparts. This might be an indication of an interplay between the chain growth ability of Co and alcohol production capability of Rh and Cu and an evidence of synergistic promotion. Fig. 3–12 shows the selectivity to methanol, ethanol, and propanol of the Co-Rh and Co-Cu catalysts. It can be seen form Fig. 3–12 that both bimetallics produce propanol, which is not present when pure Co catalysts are used, and show an increase in the ethanol production. For both Co-Rh and Co-Cu catalysts, ethanol is the major alcohol to be produced, followed by methanol and then propanol. However, at the conversion levels studied here, the alcohol selectivities are extremely low; literature reports typically show much higher alcohol selectivity but at very high conversions with a corresponding loss in activity [65–69].

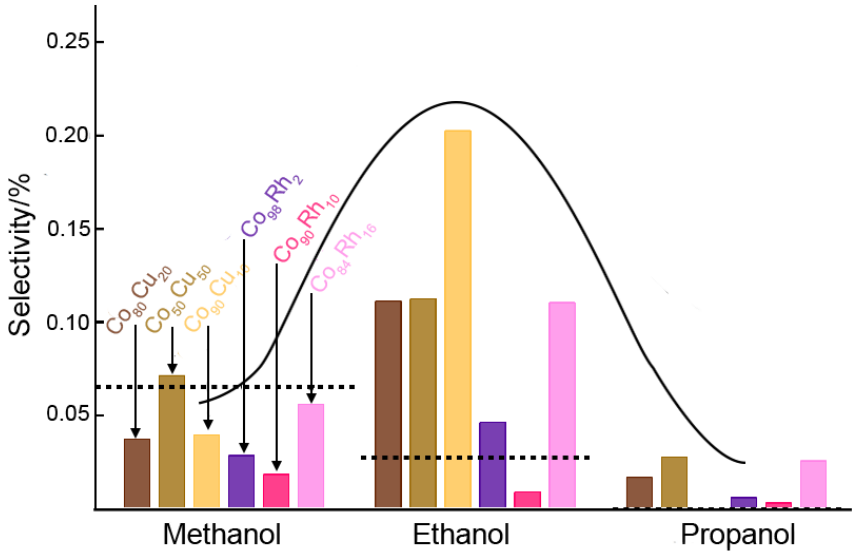

Fig. 3–12. Alcohol selectivity (C atom%) for the Co-Cu and Co-Rh nanoparticle series. The horizontal dashed lines denote the alcohol selectivity of pure 5nm Co particles, whereas the black curve is simply a guide to illustrate the overall trends.

For Co-Rh nanoparticle composition series, alcohol production was evaluated at various reaction temperatures (Fig. 3–13). It was found that for $Co_{84}Rh_{16}$ nanoparticle catalyst, methanol was the first alcohol to be produced at 220 °C. Ethanol and propanol were observed at higher reaction temperatures of 230 °C for ethanol and 240 °C for propanol. The selectivity of each alcohol as well as the total alcohol production increase as the reaction temperature increases. The apparent activation energy for each alcohol was calculated using the Arrhenius equation and the values increase in the order of methanol (E_a = 168.4 kJ/mol), ethanol (E_a = 261.6 kJ/mol), and propanol (E_a = 289.7 kJ/mol). This is in accordance with the fact that larger alcohols are only produced at higher temperatures.

A similar trend in the activation energy of alcohol formation is observed for Co-Cu bimetallic catalysts, with the methanol formation having the lowest and propanol formation having the highest apparent activation energy.

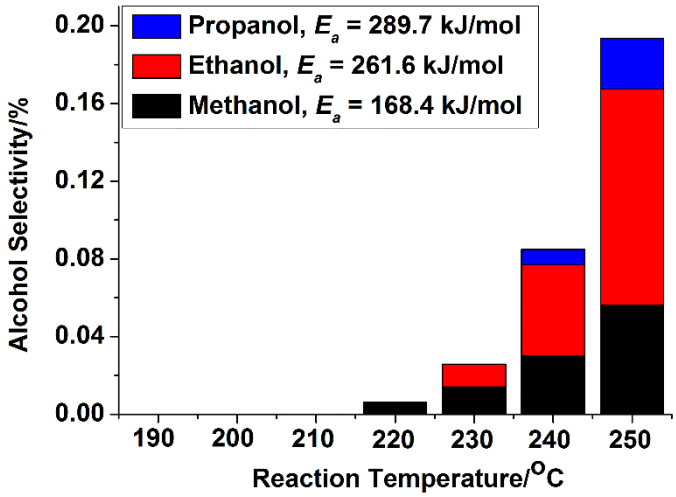

Fig. 3–13. Alcohol selectivity as a function of reaction temperature on $Co_{84}Rh_{16}$/MCF-17 catalyst.

The alcohol selectivity was also correlated with surface compositions obtained from the AP-XPS measurement. The result is shown in Fig. 3–14a. It clearly indicates an optimum surface Rh concentration (~9 at.%) for alcohol production, where a fivefold enhancement in the ratio of alcohols to hydrocarbons (C_1–C_3) was observed as compared to the Co/MCF-17 catalyst. This surface composition corresponds to the situation where approximately every Rh atom is surrounded by six Co atoms. The percentage of larger alcohols such as propanol in the total alcohol production was also found to be dependent on the surface Rh concentration, which maximizes at ~37 at.% of Rh (Fig. 3–14b).

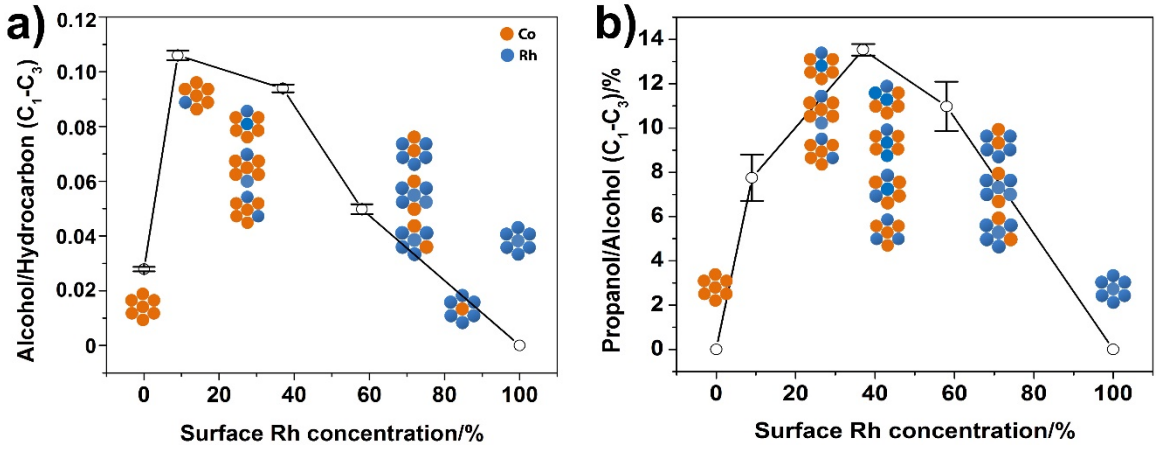

Fig. 3–14. a) The ratio of alcohols to hydrocarbons (C_1–C_3) and b) the percentage of propanol in the total alcohol production as a function of surface Rh concentration under reaction conditions ($CO:H_2$ = 1:2 at 230 °C and the total pressure of the system is 100 mTorr). The particle schematics shown are illustrative in representing possible surface compositions.

In terms of the types of promotional effects observed, the easiest to identify is the synergistic effect of adding Rh or Cu with the increased production of oxygenated species.

Electronic effects and structural effects are difficult to disentangle; all of the nanoparticles undergo surface reconstructions giving more or less exposed Co surface sites (a structural effect) but the location of the promoter after this reconstruction is important to understand whether it is blocking Co or electronically modifying Co in some way. From the initial catalytic results obtained here, it appears that Mn and Rh act as electronic promoters, as they have increased activity compared to pure Co. Re, a known structural promoter, shows a complex behavior as it appears to cover the majority of Co (only 26% Co on the surface after the oxidation and reduction pretreatments) and depresses the activity.

From the catalytic tests, it is evident the bimetallic Co-M nanoparticles can attain high activity and C_{5+} selectivity, depending on the type and amount of promoter added. Here, we have reported the synthesis of a variety of bimetallic nanoparticle systems, but many have high concentrations of the secondary element ($Co_{74}Re_{26}$ for example) which may be poisoning the Co surface. The promoter may be blocking Co sites or interfering with the creation of Co ensemble sites associated with specific reaction pathways. It has been shown that B_5 types of sites are required for CO dissociation and possibly future chain growth [10], and that these sites are more prevalent on larger particles [70]; it may be the case where promotional effects may be more pronounced at larger Co particle sizes (8 - 10 nm or larger). Below this critical size, promoter effects become less important and the catalyst behaviour resembles pure Co.

3.4 Conclusions

In summary, the synthesis of a variety of spherical Co-M bimetallic nanoparticles via thermal decomposition/reduction methods and their characterizations are reported. The new methods developed for synthesizing Co-M particles (M = Mn, Ru, Re, Rh) are general and can potentially be used to produce other types of size and composition controlled bimetallic nanoparticles. A discussion on the choice of metal precursor (carbonyls or acetylacetonate salts) and key reaction parameters is presented along with the specific synthetic requirements for each bimetallic system.

Transmission electron microscopy (TEM) was used to characterize the dispersity of the Co-M nanoparticles, along with single particle STEM-EDS/EELS measurements which confirmed the bimetallic nature of the nanoparticles; no monometallic nanoparticles were observed to have formed during the reported synthesis. Synchrotron based ambient pressure X-ray photoelectron spectroscopy (AP-XPS) and X-ray absorption spectroscopy (XAS) followed the surface and near surface compositions of the nanoparticles as well as the oxidation states of the surface species under oxidizing, reducing, and reactive gas environments. All the bimetallic nanoparticles were shown to undergo surface reconstruction when exposed to different gas environments and generally less cobalt was found on the surface of the nanoparticles under reducing and reaction conditions.

The synthesized nanoparticles were tested for applications in the Fischer-Tropsch reaction, as model catalysts to study the effect of intimate contact of a second metal promoter on cobalt catalysts. The catalytic results are interpreted in terms of the available Co on the surface from AP-XPS, and it was found that Rh and Mn appear to be effective electronic promoters, while Rh and Cu show synergistic promotion through increased levels of oxygenated products. Re effectively promotes the reduction of Co at lower

temperatures, but the Co-Re particles have much lower activity compared to monometallic Co of the same size. A fundamental understanding of the oxidation state, location, and local structure of the Co and promoter is imperative to unravelling the various effects each promoter can have; indeed, even with the simplification of the Co and promoter being in the same nanoparticle, there is still a high degree of complexity. In spite of this, we believe the use of model nanoparticle catalysts will propel the research on additives and promoters to new frontiers in heterogeneous catalysis.

3.5 References

1. BASF (1913) German Patent 293787
2. BASF (1914) French Patent 468427
3. Mittasch A, Schneider C (1916) US Patent 1201850
4. Davis BH, Occelli ML (2006) Fischer-Tropsch Synthesis, Catalysts and Catalysis. Elsevier Science, Boston
5. Anderson RB (1984) The Fischer-Tropsch Synthesis. Academic Press, Orlando
6. Bezemer GL, Bitter JH, Kuipers HPCE, Oosterbeek H, Holewijn JE, Xu X, Kapteijn F, van Dillen AJ, de Jong KP (2006) J Am Chem Soc 128:3956–3964
7. den Breejen J, Radstake PB, Bezemer GL, Bitter JH, Frøseth V, Holmen A, de Jong KP (2009) J Am Chem Soc 7197–7203
8. Melaet G, Lindeman AE, Somorjai GA (2013) Top Catal 57:500–507
9. Yang J, Frøseth V, Chen D, Holmen A (2016) Surf Sci 648:67–73
10. Ralston WT, Melaet G, Saephan T, Somorjai GA (2017) Angew Chemie - Int Ed 56:7415–7419
11. Tauster SJ, Fung SC, Garten RL (1978) J Am Chem Soc 100:170–175
12. Tauster SJ, Fung SC, Baker RTK, Horsley JA (1981) Science 211:1121–1125
13. Melaet G, Ralston WT, Li C-S, Alayoglu S, An K, Musselwhite N, Kalkan B, Somorjai GA (2014) J Am Chem Soc 136:2260–2263
14. Iglesia E, Soled SL, Fiato RA, Via GH (1993) J Catal 143:345–368
15. Iglesia E (1997) Appl Catal A Gen 161:59–78
16. Jacobs G, Das TK, Zhang Y, Li J, Racoillet G, Davis BH (2002) Appl Catal A Gen 233:263–281
17. Ertl G, Knozinger H, Schuth F, Weitkamp J (2008) Preparation of Solid Catalysts. In: Handbook of Heterogeneous Catalysis, 2nd ed. Wiley-VCH, Weinheim
18. Khodakov AY, Chu W, Fongarland P (2007) Chem Rev 107:1692–1744
19. Morales BYF, Weckhuysen BM (2006) Promotion Effects in Co-based Fischer–Tropsch Catalysis. Catalysis 19:1–40

20. Campbell CT (1990) Annu Rev Phys Chem 41:775–837

21. Rodriguez JA, Goodman DW (1991) J Phys Chem 95:4196–4206

22. Alayoglu S, Beaumont SK, Zheng F, Pushkarev VV, Zheng H, Iablokov V, Liu Z, Guo J, Kruse N, Somorjai GA (2011) Top Catal 54:778–785

23. Iablokov V, Beaumont SK, Alayoglu S, Pushkarev VV, Specht C, Gao J, Alivisatos AP, Kruse N, Somorjai GA (2012) Nano Lett 12:3091–3096

24. Lide DR (2004) CRC Handbook of Chemistry and Physics, 84th ed. CRC Press LLC, Boca Raton, FL

25. Skriver HL, Rosengaard NM (1992) Phys Rev B 46:7157–7168

26. Vitos L, Ruban A V, Skriver HL, Kollár J (1998) Surf Sci 411:186–202

27. Kittel C (2005) Introduction to Solid State Physics, 8th ed. John Wiley & Sons, Hoboken, NJ

28. Luo Y-R (2007) Comprehensive Handbook of Chemical Bond Energies. CRC Press LLC, Boca Raton, FL

29. Owen EA, Madoc Jones D (1954) Proc Phys Soc Sect B 67:456–466

30. Puntes VF, Krishnan KM, Alivisatos AP (2001) Science 291:2115–2117

31. Van Embden J, Chesman ASR, Jasieniak JJ (2015) Chem Mater 27:2246–2285

32. Gilroy KD, Ruditskiy A, Peng HC, Qin D, Xia Y (2016) Chem Rev 116:10414–10472

33. Liu W-C, Melaet G, Ralston WT, Alayoglu S, Horowitz Y, Ye R, Hurlburt T, Mao B, Crumlin E, Salmeron M, Somorjai GA (2016) Catal Lett 146:1574–1580

34. Fillman LM, Tang SC (1984) Thermochim Acta 75:71–84

35. Alayoglu S, Beaumont SK, Melaet G, Lindeman AE, Musselwhite N, Brooks CJ, Marcus MA, Guo J, Liu Z, Kruse N, Somorjai GA (2013) J Phys Chem C 117:21803–21809

36. Yeh JJ, Lindau I (1985) Atom Data Nucl Data 32:1–155

37. Schmidt-Winkel P, Lukens WW, Zhao D, Yang P, Chmelka BF, Stucky GD (1999) J Am Chem Soc 121:254–255

38. Beaumont SK, Alayoglu S, Pushkarev VV, Liu Z, Kruse N, Somorjai GA (2013) Faraday Discuss 162:31–44

39. Tao F, Grass ME, Zhang Y, Butcher DR, Aksoy F, Aloni S, Altoe V, Alayoglu S, Renzas JR, Tsung CK, Zhu Z, Liu Z, Salmeron M, Somorjai GA (2010) J Am Chem Soc 132:8697–8703

40. Beitel GA, de Groot CPM, Oosterbeek H, Wilson JH (1997) J Phys Chem B 101:4035–4043

41. Weststrate CJ, van de Loosdrecht J, Niemantsverdriet JW (2016) J Catal 342:1–16

42. Ehrensperger M, Wintterlin J (2014) J Catal 319:274–282

43. Cats KH, Gonzalez-Jimenez ID, Liu Y, Nelson J, van Campen D, Meirer F, van der Eerden AMJ, de Groot FMF, Andrews JC, Weckhuysen BM (2013) Chem Commun 49:4622–4624

44. Navarro V, van Spronsen MA, Frenken JWM (2016) Nat Chem 8:929–934

45. Han HL, Melaet G, Alayoglu S, Somorjai GA (2015) ChemCatChem 7:3625–3638

46. Bluhm H, Hävecker M, Knop-gericke A, Kiskinova M, Schlögl R, Salmeron M (2007) MRS Bull 32:1022–1030

47. Abbate M, Goedkoop JB, de Groot FMF, Grioni M, Fuggle JC, Hofmann S, Petersen H, Sacchi M (1992) Surf Interface Anal 18:65–69

48. Tanuma S, Powell CJ, Penn DR (1994) Surf Interface Anal 21:165–176

49. Grass ME, Zhang Y, Butcher DR, Park JY, Li Y, Bluhm H, Bratlie KM, Zhang T, Somorjai GA (2008) Angew Chem Int Ed 47:8893–8896

50. Muiioz A, Munuera G, Malet P, Gonzalez-Elipe AR, Espinos JP (1988) Surf Interface Anal 12:247–252

51. Melaet G, Ralston WT, Li C-S, Alayoglu S, An K, Musselwhite N, Kalkan B, Somorjai GA (2014) J Am Chem Soc 136:2260–2263

52. Ducros R, Fusy J (1987) J Electron Spectros Relat Phenomena 42:305–312

53. Miniussi E, Hernández ER, Pozzo M, Baraldi A, Vesselli E, Comelli G, Lizzit S, Alfé D (2012) J Phys Chem C 116:23297–23307

54. Greiner MT, Rocha TCR, Johnson B, Klyushin A, Knop-Gericke A, Schlögl R (2014) Zeitschrift fur Phys Chemie 228:521–541

55. Fairley N (2005) CasaXPS. http://www.casaxps.com

56. Biesinger MC, Lau LWMM, Gerson AR, St.C. Smart R (2011) Appl Surf Sci 257:2717–2730

57. Oku M, Hirokawa K, Ikeda S (1975) J Electron Spectros Relat Phenomena 7:465–473

58. Vada S, Hoff A, Ådnanes E, Schanke D, Holmen A (1995) Top Catal 2:155–162

59. Jacobs G, Chaney JA, Patterson PM, Das TK, Davis BH (2004) Appl Catal A Gen 264:203–212

60. Ronning M, Nicholson DG, Holmen A (2001) Catal Lett 72:141–146

61. ASM International (1992) Alloy Phase Diagrams. In: ASM Handbook, Vol.3. Ohio

62. Jacobs G, Ma W, Davis B (2014) Catalysts 4:49–76

63. Logdberg S, Lualdi M, Jaras S, Walmsley JC, Blekkan EA, Rytter E, Holmen A (2010) J Catal 274:84–98

64. Rytter E, Tsakoumis NE, Holmen A (2016) Catal Today 261:3–16

65. Xiang Y, Chitry V, Kruse N (2013) Catal Lett 143:936–941

66. Xiang Y, Chitry V, Liddicoat P, Felfer P, Cairney J, Ringer S, Kruse N (2013) J Am Chem Soc 135:7114–7117

67. Xiang Y, Barbosa R, Kruse N (2014) ACS Catal 4:2792–2800

68. Tsai Y-T, Mo X, Goodwin JG (2012) J Catal 285:242–250

69. Mo X, Tsai YT, Gao J, Mao D, Goodwin Jr. JG (2012) J Catal 285:208–215

70. van Helden P, Ciobîcă IM, Coetzer RLJ (2015) Catal Today 261:48–59

Chapter 4 – Oxidative Coupling of Methane (OCM): Effect of Noble Metal (M = Pt, Ir, Rh) Doping on the Performance of Mesoporous Silica MCF-17 Supported Mn_xO_y-Na_2WO_4 Catalysts

Abstract

Noble metal doped M-Mn_xO_y-Na_2WO_4/SiO_2 (M = Pt, Ir, Rh) catalysts were prepared via a wet impregnation method using mesoporous silica MCF-17 as the support, and their performance in the oxidative coupling of methane (OCM) was studied in a fixed-bed flow reactor. The reaction was carried out at 750 °C under atmospheric pressure with a gas feed composition of CH_4:O_2 = 4:1. The incorporation of the noble metals yielded an enhanced selectivity towards both C_2 and C_3 hydrocarbons as compared to the undoped Mn_xO_y-Na_2WO_4/MCF-17 catalyst in the order of Rh-doped>Ir-doped>Pt-doped samples together with a lower olefin to paraffin ratio. On the other hand, the Ir-doped catalyst showed the highest overall yield for C_2 production. Elemental analysis, N_2-adsorption, and X-ray powder diffraction (XRD) measurements confirmed similar metal loading, surface area, and phase composition for both the undoped and doped catalysts. Electron microscopy analysis showed a near-homogeneous distribution of Na and W but a higher tendency to form aggregates for Mn, with the Rh-doped catalyst being the best in overall elemental dispersion. X-ray photoelectron spectroscopy (XPS) and temperature programmed reduction (H_2-TPR) results indicate a more reduced nature of the surface oxide species in the noble metal doped catalysts as compared to the undoped one. The results also suggest a more optimized strength of interaction between the carbon intermediates and the surface of the noble metal doped catalysts, which in combination with the improved reducibility of Mn and W species and metal dispersion, accounted for the enhanced C_2 production on the noble metal doped Mn_xO_y-Na_2WO_4/MCF-17 catalysts.

4.1 Introduction

Oxidative coupling of methane, in which CH_4 molecules are catalytically transformed into C_2 hydrocarbons in the presence of an oxidizing reagent, possesses the potential capability of directly utilizing natural gas for the production of value added chemicals [1–4]. Different types of catalysts and combinations thereof have been examined for this reaction, and the Mn_xO_y-Na_2WO_4/SiO_2 system is among the very few of those that provide high C_2 yield and excellent stability at the same time [5,6]. Extensive research has been performed on this catalyst system, in which the effect of the preparation methods, elemental concentrations, and the variation of each of its components have been reported [7]. For catalyst preparation, the wet impregnation and the mixture slurry methods are proven to be more efficient in producing high-performance catalysts [8]. As for the catalyst composition, results have indicated that there exist a range of combinations, i.e., 0.4–2.3% for Na, 2.2–8.9% for W, and 0.5–3.0% for Mn, that would allow an optimized C_2 yield [9]. In addition, Yildiz et al. showed that by simply utilizing a mesoporous silica support, the elemental dispersion is improved, resulting in a higher overall C_2 production [10,11].

In spite of the large amount of work performed on this catalytic system in the OCM reaction, the effect of noble metal additives is experimentally less explored. In liquid phase homogenous catalysis, noble metal complexes including that of Pt, Rh, and Ir are widely used as catalysts for C–H bond activation [12,13]. In addition, there have been several theoretical investigations suggesting a potential promotional effect on the CH4 activation and C–C bond coupling on the surface of IrO_2 [14–16]. Therefore, it is reasonable to explore the effect of noble metal doping on the performance of the Mn_xO_y-Na_2WO_4/SiO_2 system.

Herein, we report the investigation on the effect of noble metal doping (M = Pt, Ir, Rh) on the performance of the Mn_xO_y-Na_2WO_4/SiO_2 system. The catalysts were synthesized via a wet impregnation method with mesoporous silica material MCF-17 as the support. Their structural and chemical properties were characterized using techniques including X-ray powder diffraction (XRD), transmission electron microscopy (TEM), scanning transmission electron microscopy-energy dispersive spectroscopy (STEM-EDS), scanning electron microscopy (SEM), inductively coupled plasma atomic emission spectroscopy (ICP-AES), X-ray photoelectron spectroscopy (XPS), N_2-adsorption, and H_2-TPR. The catalytic performance of the M-Mn_xO_y-Na_2WO_4/SiO_2 system (M = Pt, Ir, Rh) was studied in a continuous flow reactor, of which the results are compared and discussed in combination with the information obtained from the characterization studies.

4.2 Experimental

4.2.1 Preparation of Mn_xO_y-Na_2WO_4/MCF-17 Catalysts

The mesoporous silica material MCF-17 was prepared beforehand using a method reported previously [17]. It has cell-like mesopores with tunable sizes that are connected by windows, large surface area and pore volume, and has been used as the catalyst support in various applications, such as Fischer-Tropsch synthesis and alkane isomerization reactions [18–20]. In a typical synthesis, a desired amount of MCF-17 was firstly impregnated with an aqueous solution of manganese (II) acetate (Sigma-Aldrich, ≥99%) at room temperature and then dried in air at 80 °C overnight. Afterwards, the mixture was

impregnated with an aqueous solution of sodium tungstate (Sigma-Aldrich, ≥99%) at room temperature followed by drying in air at 80 °C overnight. The obtained material was calcined in air at 750 °C for 1 h with a heating rate of 1 °C/min. The obtained catalyst is denoted as 'Original'.

4.2.2 Preparation of M-Mn_xO_y-Na_2WO_4/MCF-17 (M = Pt, Ir, Rh) Catalysts

The preparation of noble metal doped Mn_xO_y-Na_2WO_4/MCF-17 catalysts follows a similar procedure described above. After impregnation with manganese (II) acetate and sodium tungstate and dried at 80 °C overnight, the obtained material was then divided into three portions with each being impregnated with a certain metal precursor (Sigma-Aldrich, rhodium(III) acetylacetonate [$Rh(acac)_3$, 97%], platinum(II) acetylacetonate [$Pt(acac)_2$, 97%], or Iridium(III) acetylacetonate [$Ir(acac)_2$, 97%]) dissolved in chloroform [Fisher Scientific, ≥99%]. The calcination process was carried out in air at 750 °C for 1 h with a heating rate of 1 °C/min. The obtained catalysts are denoted as 'Pt-doped' for M = Pt, 'Ir-doped' for M = Ir, and 'Rh-doped' for M = Rh.

4.2.3 Characterizations of M-Mn_xO_y-Na_2WO_4/MCF-17 (M = Pt, Ir, Rh) Catalysts

XRD measurements of the fresh and spent catalysts were performed using a Bruker D2 Phaser Benchtop X-ray powder diffractometer with a Cu x-ray source (Kα 1.54184 Å). 2 theta value was varied from 10° to 60° with a step size of 0.02°.

TEM and STEM-EDS analysis were performed using a JEOL JEM2100F TEM equipped with an Inca Energy Dispersive Spectrometer operated at 200 kV. Samples for TEM analysis were prepared by first dispersing the catalysts in ethanol and then dropping the dispersion on ultrathin lacey carbon TEM grids (Ted Pella, Inc.). SEM images of the fresh catalysts were obtained with a FEI/Philips XL-30 Field Emission ESEM operated at 15 kV. Samples for SEM analysis were prepared by drop-casting the dispersion of the catalysts in isopropanol on a piece of silicon wafer. The loading of the prepared catalysts was determined using ICP-AES on a PerkinElmer ICP Optima 7000 DV spectrometer. Samples for ICP-AES measurements were prepared by first digesting the catalyst powder with nitric acid and hydrofluoric acid and then diluting with deionized water.

The surface composition and oxidation states of the catalysts were examined using PHI 5400 XPS System with an Al X-ray source (Kα 1486.6 eV). A pass energy of 35.75 eV with a step size of 0.05 eV was used. Samples for XPS measurements were prepared by drop-casting the dispersion of the catalysts in isopropanol on a piece of silicon wafer. All samples were dried in a vacuum oven at 85 °C overnight before testing. The binding energies were corrected for charging effect with respect to the Si 2p line at 103.4 eV [21,22]. The spectra were fitted with a Shirley background and the area under the peaks is calibrated using the Relative Sensitivity Factor provided in the CasaXPS library.

The specific surface area and the pore structure of the catalysts were verified using N_2-adsorption at liquid nitrogen temperature on an ASAP 2020 Surface Area and Porosimetry System (Micromeritics). BET and BJH models were used for the determination of surface area and pore size distribution, respectively.

H_2-TPR measurements were carried out to assess the reducibility of the catalysts. A high purity mixture of 5% H_2/Ar (Praxair) flowing at 30 sccm was used as the reducing

gas. The reactor was heated to 850 °C with a heating rate of ~6 °C/min and the composition of the outlet gas was monitored by an online quadrupole mass spectrometer (SRS RGA 200).

4.2.4 Catalytic Measurements

OCM reaction was performed in a home-built fixed bed flow reactor under atmospheric pressure. The catalysts were sieved to an average grain size of 150–250 um. Approximately 60 mg of the sieved catalyst was mixed with quartz sand (Umicore, 99.99%, grain size: 0.2–0.7 mm) and then packed in the center of a quartz reactor tube (Quartz Scientific, 16 inches, 4 mm ID, 6.35 mm OD) with quartz wool. Additional quartz sand was packed on both sides of the catalytic bed to help reduce the empty space of the reactor and promote heat dissipation. Methane (Praxair, 5.0 Research Grade) and synthetic air (Praxair, Ultra Zero) were fed into the reactor using carefully calibrated mass flow controllers (Parker) with a total flow rate of 60 sccm and a composition of CH_4:O_2:N_2 = 4:1:4. The reactor was heated to 750 °C with a heating rate of 8 °C/min by an electric tube furnace. Outlet gas was sampled and separated using an on-line GC–MS (Agilent 7890A-5975C) equipped with two capillary columns (HP-PLOT Q and HP-PLOT MoleSieve). The gaseous composition was analyzed by a thermal conductivity detector (TCD) and a flame ionization detector (FID) detector equipped with a methanizer.

Reaction conversion X is calculated from the difference in the inlet and outlet concentration of methane (Eq. 4–1). The selectivity of the reaction is given by dividing the amount of product i by the total amount of the reaction products (Eq. 4–2). The carbon balance is calculated using the total amount of products plus the unreacted methane divided by the amount of methane fed into the reactor (Eq. 4–3).

$$X = \frac{CH_4^{\,in} - CH_4^{\,out}}{CH_4^{\,in}} \qquad \textbf{Eq. 4–1}$$

$$S_i = \frac{\text{Product } i}{\sum_i \text{Product } i} \qquad \textbf{Eq. 4–2}$$

$$\text{Carbon balance} = \frac{\sum_i \text{Product } i + CH_4^{\,out}}{CH_4^{\,in}} \qquad \textbf{Eq. 4–3}$$

4.3 Results and Discussion

4.3.1 Characterizations

4.3.1.1 Surface Area and Porosity Measurements

The BET surface area and pore structure of the MCF-17 support material and the supported catalysts are reported in Table 4–1. The pristine MCF-17 exhibits a surface area of 566 $m^2 \cdot g^{-1}$, owing to its porous nature. The total pore volume is 1.6 $cm^3 \cdot g^{-1}$ with an average pore size of 16 nm, which are typical among its category. After impregnation and calcination, the catalysts showed a significant loss of surface area and porosity (Table 4–

1). The measured surface areas are among 7–9 m^2/g and the total pore volumes are in the vicinity of 0.020 $cm^3 \cdot g^{-1}$ for all the prepared catalysts. This could be explained by the structural change of the silica support induced by the phase transformation from amorphous SiO_2 to others forms, such as α-cristobalite and tridymite (Fig. 4–5), causing the collapse of the porous structure.

Table 4–1. BET surface area and total pore volume of MCF-17 and the prepared catalysts

	MCF-17	Original	Rh-doped	Ir-doped	Pt-doped
BET surface area/$m^2 \cdot g^{-1}$	566.3 ± 4.9	9.18 ± 0.04	8.91 ± 0.02	8.19 ± 0.03	7.59 ± 0.02
Total pore volume[a]/$cm^3 \cdot g^{-1}$	1.598	0.024	0.024	0.021	0.017
Average pore size[b]/nm	16.6	-	-	-	-

[a]BJH adsorption cumulative volume of pores. [b]BJH adsorption pore size.

BET measurements of the spent samples were also performed and the measured surface area are typically around 4–5 m^2/g for all the catalysts tested, indicating a slight decrease in the surface area after the reaction.

4.3.1.2 Composition Analysis

The elemental compositions of the prepared catalysts as obtained from ICP-AES are shown in Table 4–2. The intended loading of each of the components were chosen to be within their optimal range, as mentioned in the introduction. It can be seen from Table 4–2 that the actual loadings of the catalysts agree well with the theoretical values except for a slightly lower loading for W, yet there are no significant differences among the four catalysts. The determined loadings are 0.72–0.79 wt.% for Na, 2.29–2.51 wt.% for W, and 2.04–2.37 wt.% for Mn. ICP results also confirmed that Rh, Ir, and Pt are successfully incorporated into the catalysts, of which the metal loadings are in the vicinity of 0.12 wt.%.

Table 4–2. Theoretical and determined loadings of the prepared catalysts

Elemental Composition	Theoretical Loading/wt.%	Determined Loading[a]/wt.%			
		Original	Rh-doped	Ir-doped	Pt-doped
Na	0.78[b]	0.73	0.78	0.72	0.79
W	3.13[b]	2.51	2.23	2.29	2.48
Mn	2.00[c]	2.04	2.04	2.23	2.37
Rh	0.10	-	0.13	-	-
Ir	0.10	-	-	0.12	-
Pt	0.10	-	-	-	0.12

[a]As determined from ICP-AES. [b]Corresponds to 5 wt.% of Na_2WO_4. [c]Calculated in terms of elemental Mn.

4.3.1.3 TEM, SEM and STEM–EDS Analysis

TEM and STEM measurements were performed to study the morphology and texture of the catalysts. The first column of Fig. 4–1 shows the TEM images for the fresh catalysts, next to which their dark-field (HAADF) images are also presented. The catalysts are generally in fibrous or rod-like shapes with small spherical and cubic aggregates distributed across the support. The SEM images (Fig. 4–2) also indicate the existence of the particles on the surface of the catalysts. EDS point scans (Fig. 4–3) revealed that the particles are mostly rich in Mn, with some of them also containing notable amount of W.

TEM analysis of the spent samples (Fig. 4–4) revealed plate-like shapes with particles spread across the support with sizes of tens of nanometers. In addition, both TEM and SEM images confirm the lack of porosity in the calcined catalysts, in agreement with the BET measurements.

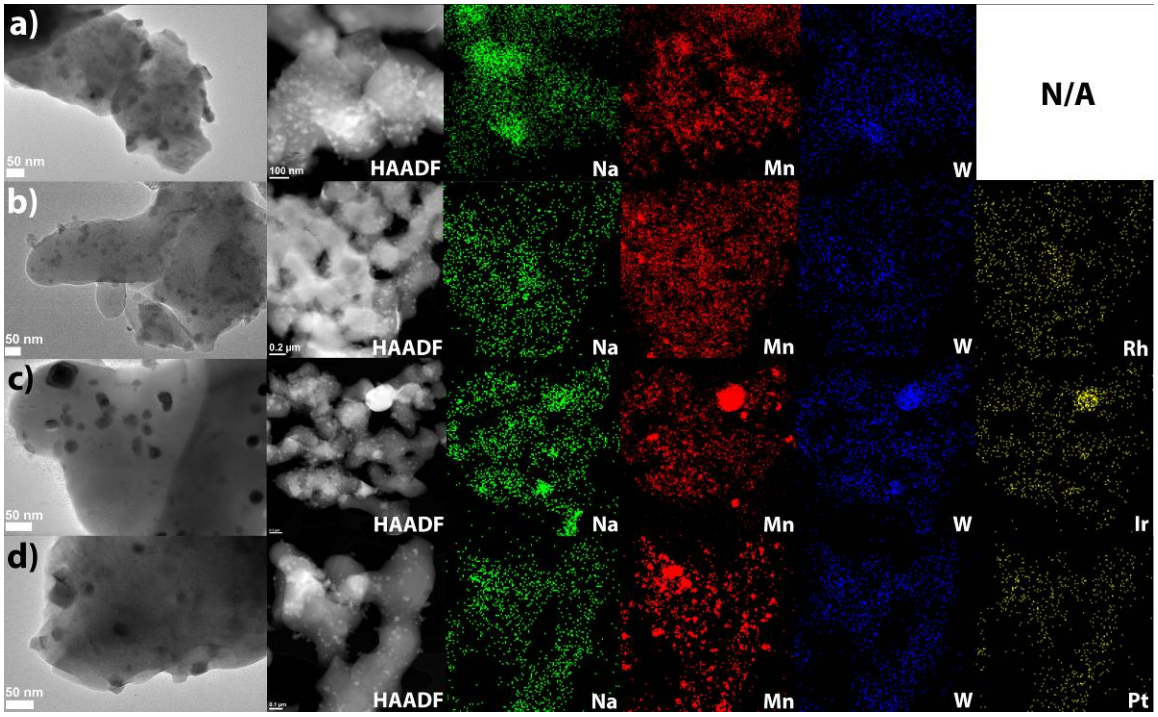

Fig. 4–1. Column 1: TEM images; Column 2: high-angle annular dark-field (HAADF) images; Columns 3-6: EDS elemental mapping results (Na: green, Mn: red, W: blue, and noble metals: yellow) of the fresh M-Mn_xO_y-Na_2WO_4/MCF-17 catalysts: a) Original; b) M = Rh; c) M = Ir; d) M = Pt.

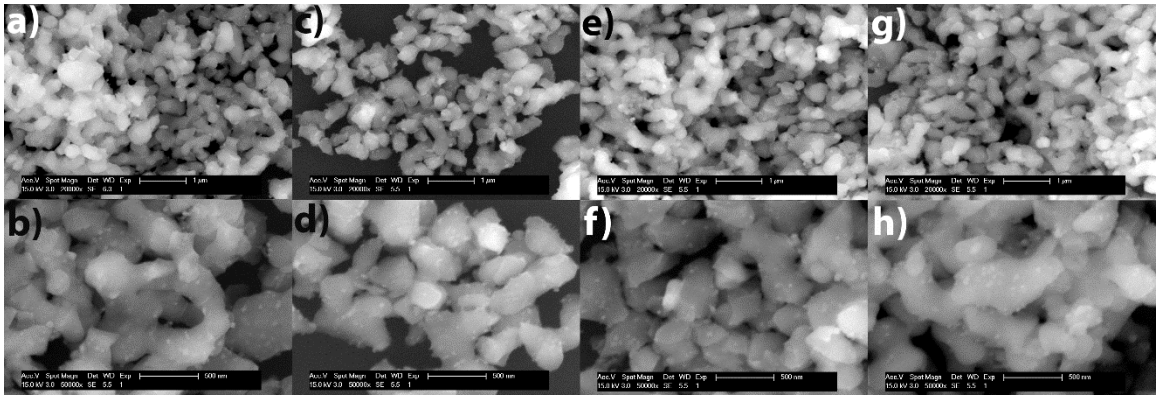

Fig. 4–2. SEM images of the fresh M-Mn_xO_y-Na_2WO_4/MCF-17 catalysts: a, b) Original; c, d) M = Rh; e, f) M = Ir; g, h) M = Pt. Images were aquired at 15 kV using a secondery electron detector.

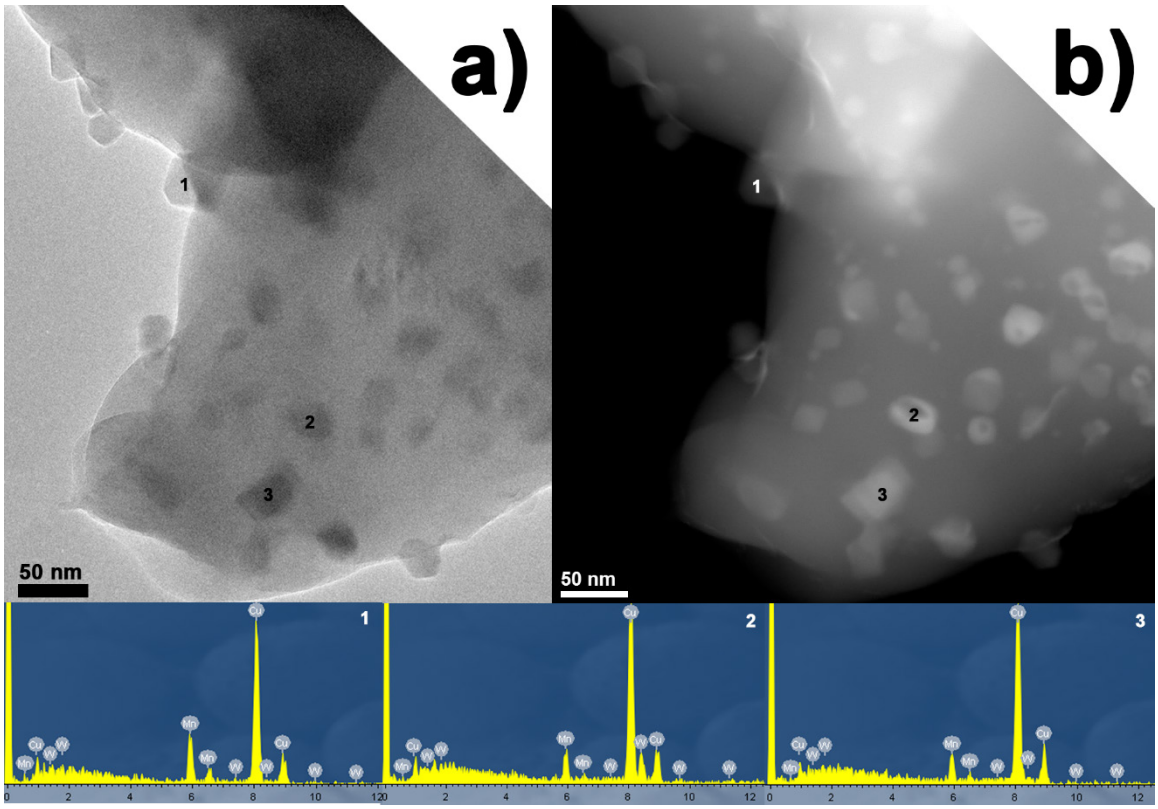

Fig. 4–3. a) TEM and b) STEM images of the fresh Ir-Mn_xO_y-Na_2WO_4/MCF-17 catalyst. 1-3) Locations where point scans were performed and their corresponding EDS spectra.

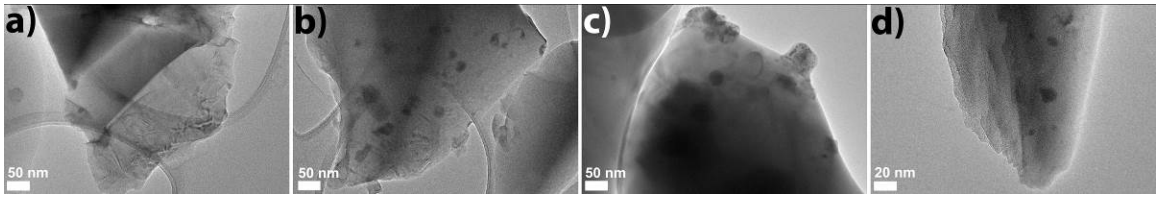

Fig. 4–4. TEM images of the spent M-Mn_xO_y-Na_2WO_4/MCF-17 catalysts: a) Original; b) M = Rh; c) M = Ir; d) M = Pt.

The catalysts were further studied with EDS mapping technique to gain information on the elemental dispersions. In general, the utilization of MCF-17 achieved good overall elemental dispersion, owing to its high surface area and pore volume as well as the ordered pore structure, which could provide significantly more sites than the regular silica-gel to homogeneously distribute the supported metals and inhibit their aggregation to achieve better fixation. More specifically, elemental mapping results (Fig. 4–1, third to sixth columns) indicate a near-homogeneous distribution of W and Na with minor formation of W-rich or Na-rich areas. On the other hand, Mn shows poorer dispersion and has a higher tendency to form small aggregates, particularly for the original and Pt-doped samples. Since the loadings of the noble metals are lower than Mn and W, the signal level is weaker. Nevertheless, results indicate homogeneous distributions of the noble metals, with no obvious aggregation or particle formation of significant sizes observed. This is also in accordance with the fact that no noble metal containing species were observed in the XRD

spectra of the doped catalysts. Among the four catalysts, the Rh-doped sample shows the best overall elemental dispersion, especially for Mn.

4.3.1.4 XRD Measurements

In order to study the phase composition, XRD measurements were conducted on both the fresh and spent catalysts. The diffraction patterns of the fresh samples are shown in Fig. 4–5a. Na_2WO_4 and Mn_2O_3 phases were clearly identified and are the main form of tungsten and manganese oxide, respectively. While most of the tungsten species exist as Na_2WO_4, features due to Na_4WO_5 were also detected. Unlike the amorphous nature of the silica support MCF-17, strong diffraction peaks associated with α-cristobalite were observed in the calcined catalysts. In addition, a small amount of tridymite was also detected, as indicated by the diffraction peak at 20.6°. The transformation of amorphous silica to α-cristobalite during the high temperature calcination process is facile with Na present, especially aided with W, and is well known for the Mn_xO_y-Na_2WO_4/SiO_2 system. [23] The phase transformation is also accompanied by a significant loss of pore volume and surface area, as shown in Table 4–1. It is also noted that no noble metal-containing crystal phases were observed for the doped catalysts, which could be explained by the low degree of metal loading and the insensitivity of X-ray diffraction to small clusters. Despite the slight variation in the intensity of the diffraction peaks, no significant difference in the phase composition was observed among the four catalysts.

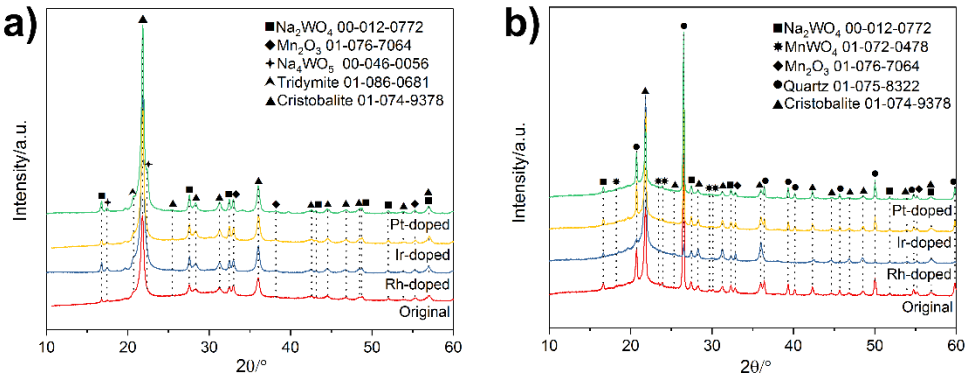

Fig. 4–5. XRD patterns of the a) fresh and b) spent catalysts. Sample names are listed under their corresponding spectra. The file numbers in the PDF database used for phase identification are listed after the name of the compound.

In the spent samples (Fig. 4–5b), $MnWO_4$ was identified in addition to Mn_2O_3, while peaks due to Na_4WO_5 disappeared after the reaction. The transformation of Mn_2O_3 to $MnWO_4$ indicates a partial reduction of Mn^{3+} to the more stable Mn^{2+}, which could be involved in the total catalytic cycle. However, its exact contribution to the catalytic performance is still unclear. One plausible mechanism involves the activation of oxygen and methane on Mn^{2+} and WO_4^{2-} sites, respectively. The spillover of the activated surface oxygens from Mn sites to W sites replenishes the active centers for methane activation and keeps the catalyst active [7,24]. In addition, α-cristobalite remains as the primary silica phase. It should be noted that the appearance of the quartz phase in the spent samples could have mainly originated from the quartz sand residue, which was used to dilute the catalyst

in the catalytic bed, and is therefore not the result of the transformation from other forms of silica during the reaction. Nonetheless, its formation could not be completely ruled out.

Using the Scherrer equation, the average sizes of the catalyst particles could be estimated (Table 4–3). The results indicate the growth of both Mn_2O_3 and Na_2WO_4 particles after the catalytic measurements. Among the four catalysts tested, the Rh-doped catalyst exhibited the biggest change in the Mn_2O_3 particle sizes before and after the reaction, with about 12 nm growth being observed.

Table 4–3. Mean particle diameters[a] of Mn_2O_3 and Na_2WO_4 in fresh and spent M-Mn_xO_y-Na_2WO_4/MCF-17 catalysts.

	Original/nm		Rh-doped/nm		Pt-doped/nm		Ir-doped/nm	
	Fresh	Spent	Fresh	Spent	Fresh	Spent	Fresh	Spent
Mn_2O_3	32.0	34.7	29.8	41.5	36.6	37.1	35.5	39.5
Na_2WO_4	33.8	36.2	36.8	39.9	35.0	39.8	33.3	42.3

[a]As obtained from Scherrer equation with K = 0.9.

4.3.1.5 XPS Analysis

Surface analysis of the prepared catalysts is carried out using XPS. Fig. 4–6 shows the XPS spectra of W 4f and Mn 2p level of the fresh catalysts. Binding energies of W 4f7/2 and Mn 2p3/2 peaks are in the range of 35.0–35.2 eV and 641.7–642.1 eV, which are assigned to the corresponding species in Na_2WO_4 and Mn_2O_3, respectively [22,25]. It is noted that the W 4f and Mn 2p spectra of the doped catalysts (35.0 eV for W 4f7/2 and 641.7 eV for Mn 2p3/2 peaks) shifted ~0.2 eV and ~0.4 eV, respectively, towards lower binding energy as compared to those of the original sample (35.2 eV for W 4f7/2 and 642.1 eV for Mn 2p3/2 peaks), which indicates a more reduced nature of the W and Mn species on the surface of the doped catalysts.

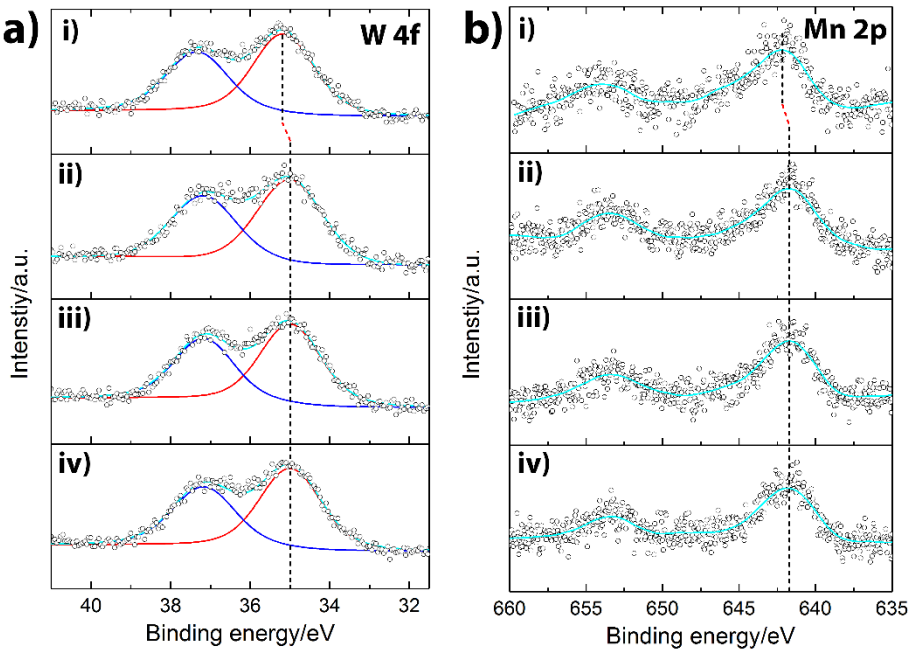

Fig. 4–6. XPS spectra of a) W 4f and b) Mn 2p level for the fresh M-Mn_xO_y-Na_2WO_4/MCF-17 catalysts: i) Original; ii) M = Rh; iii) M = Ir; iv) M = Pt. A spin-orbital splitting of 2.17 eV and an area ratio for W 4f7/2 (red) and W 4f5/2 (blue) peaks of 4:3 were used when fitting the W 4f spectra. Due to the low signal-to-noise ratio, fitting was not performed on the Mn 2p spectra.

Information on the surface compositions are shown in Table 4–4. For the fresh catalysts, comparable amounts of Na were found on the surface of both the doped and undoped samples. As for the Mn concentration, the Rh-doped catalyst showed the highest value, while similar loadings were observed for the others. The Rh-doped catalyst also displayed the highest W concentration among the four catalysts, followed by the Pt-doped and undoped samples, with the Ir-doped one exhibited the lowest surface W content. This is in accordance with the finding from other researchers that the Mn surface concentration increases with the W concentration [9,26]. The most noticeable difference in the surface concentration is observed for Mn, while the variation in the surface W content is less than 10% among the four catalysts. S.-f. Ji et al. reported an optimum surface Mn content of 1.1% for C_2 production on Mn_xO_y-Na_2WO_4/SiO_2 catalysts with similar bulk composition, below which a higher Mn surface concentration would be beneficial [9]. This agrees with the high C_2 selectivity (Fig. 4–8b) for the Rh-doped catalyst, which has the highest surface Rh concentration of 0.84%. Again, due to the quartz sand residue, the surface concentrations reported for the spent catalysts should be taken as their lower limit, and therefore only the change in the surface C concentration could be discussed without ambiguity. The spent catalysts showed significantly more amount of carbon on their surfaces after the reaction, with the increase in the order of Original ≈ Pt-doped > Ir-doped > Rh-doped samples. This is also in agreement with the degree of carbon balance during the reaction. The Rh-doped catalyst showed the best carbon balance of ~98%, followed by the Ir-doped catalyst at ~94%, while the original and Pt-doped catalysts have the lowest value of ~91%.

Table 4–4. Surface compositions[a] of the fresh and spent catalysts.

	C 1s/%		Na 1s/%		Mn 2p/%		W 4f/%	
	Fresh	Spent[b]	Fresh	Spent[b]	Fresh	Spent[b]	Fresh	Spent[b]
Original	9.6	52.3	0.27	0.14	0.53	0.13	0.89	0.65
Rh-doped	9.3	37.8	0.28	0.20	0.84	0.27	1.03	0.71
Pt-doped	8.3	50.1	0.26	0.13	0.56	0.16	0.91	0.50
Ir-doped	12.4	42.7	0.32	0.21	0.56	0.13	0.83	0.68

[a]As obtained from XPS. [b]Due to the quartz sand residue, the surface concentrations reported for the spent catalysts should be taken as their lower limits.

4.3.1.6 H_2-TPR Analysis

Fig. 4–7 shows the H_2-TPR results for the fresh catalysts. The reduction peaks in the range of 300 °C to 650 °C are associated with the reduction of Mn. The broadness of the peak and the shoulder feature indicate the coexistence of different Mn species. The broad feature starting from 700 °C represents the reduction of the W species in the catalysts [23,27]. As compared to the undoped Mn_xO_y-Na_2WO_4/SiO_2 sample, the incorporation of noble metals facilitates the reduction of Mn, as indicated by the higher intensity of the Mn reduction features between 300 °C to 650 °C and their shift to lower temperatures, especially for the Rh-doped catalyst. The change in the reducibility could also be due to a

better dispersion of the MnO_x species [28], as is in accordance with the EDS mapping results. On the other hand, the Pt-doped and Ir-doped catalysts showed the W reduction feature at more than 20 °C lower in temperature than the Rh-doped sample.

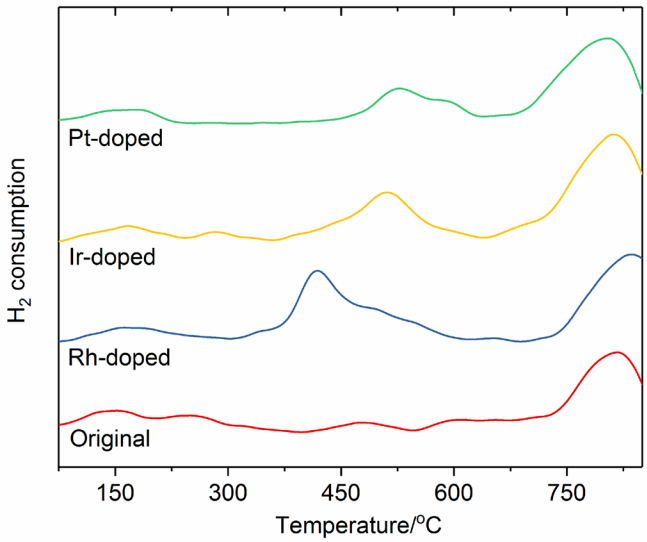

Fig. 4–7. H_2-TPR profiles of the fresh catalysts. Sample names are listed under their corresponding scans. A high purity mixture of 5% H_2/Ar was used as the reducing gas with a flow rate of 30 sccm. The reactor was heated to 850 °C with a heating rate of ~6 °C/min.

4.3.2 Catalytic Measurements

The catalysts, after being pelletized and sieved, were utilized in the OCM reaction. Fig. 4–8a shows the reaction conversion as a function of time on stream. Among the four catalysts tested, the undoped Mn_xO_y-Na_2WO_4/MCF-17 catalyst showed the highest conversion at 15.6%. The introduction of noble metal dopants led to a slight decrease in the CH_4 conversion, with that of the Pt-doped, Ir-doped, and Rh-doped catalysts being at 14.1%, 14.4%, and 9.3%, respectively (Table 4–5). No significant deactivation was observed for the catalysts during the time period (~12 h) tested.

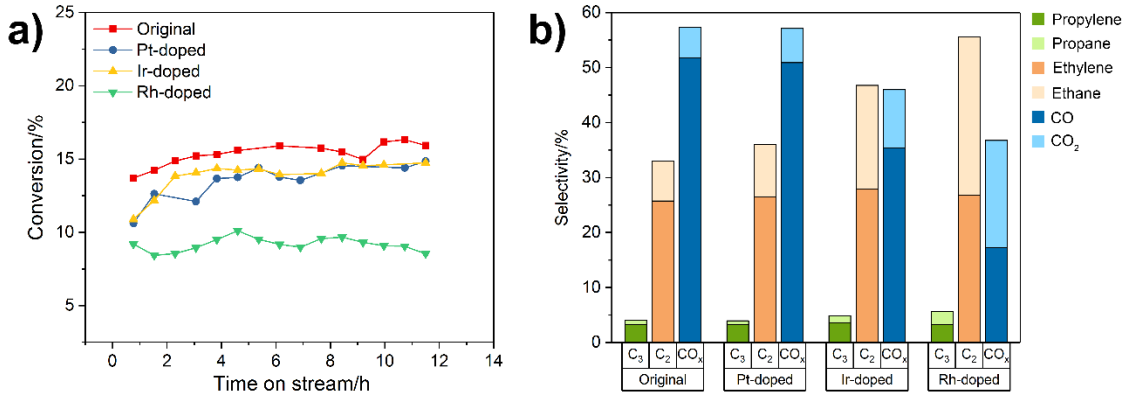

Fig. 4–8. a) Reaction conversion as a function of time on stream and b) reaction selectivity of C_2, C_3, and CO_x for all the catalysts in the OCM reaction. Reaction conditions: feed composition of CH_4:O_2:N_2 = 4:1:4, total flow rate of 60 sccm, and reaction temperature of 750 °C. Selectivity is in terms of carbon.

Table 4–5. OCM activity and selectivity after ~12h of time on stream[a].

Catalysts	CH_4 Conversion/%	Selectivity[b]/%			C_2H_4/C_2H_6	C_3H_6/C_3H_8	CO_2/CO
		C_2	C_3	CO_x			
Original	15.6	33.0	4.0	57.3	3.6	4.4	0.11
Rh-doped	9.3	55.6	5.6	36.7	0.93	1.4	1.1
Ir-doped	14.4	46.7	4.8	46.0	1.5	3.0	0.30
Pt-doped	14.1	36.1	4.0	57.1	2.8	4.7	0.12

[a]Reaction conditions: feed composition of CH_4:O_2:N_2 = 4:1:4, total flow rate of 60 sccm, and reaction temperature of 750 °C. [b]Selectivity is in terms of carbon.

The product distribution for all the catalysts are shown Fig. 4–8b. C_2 hydrocarbons (C_2H_4 and C_2H_6) and CO_x (CO and CO_2) make up the majority of the reaction products (> 90%). A small amount (~4–6% in selectivity) of C_3s (C_3H_6 and C_3H_8), which are due to the further chain growth of C_2 hydrocarbons, are also observed. The incorporation of noble metals improved the selectivity towards both C_2 and C_3 hydrocarbons in the order of Rh-doped>Ir-doped>Pt-doped catalyst. The doped catalysts also showed lower C_2H_4/C_2H_6 and C_3H_6/C_3H_8 ratios as compared to their undoped counterpart. The olefin to paraffin ratio for both C_2s and C_3s follows the same trend, in which the Rh-doped catalyst offers the lowest value, followed by the Ir-doped and Pt-doped catalysts, while the original sample shows the highest percentage of unsaturated products. The decrease in the olefin to paraffin ratio for the noble metal doped catalysts indicates a less favorable ethane dehydrogenation process.

The yield of different products are shown in Fig. 4–9b. It can be seen from Fig. 4–9b that the Ir-doped catalyst showed the highest overall yield for C_2 and C_3 hydrocarbons. The Rh-doped sample, having the highest selectivity, exhibited a smaller degree of improvement on the C_2 yield due to a slightly lower conversion. The Pt-doped and the undoped samples displayed similar activity towards overall C_2 production. Since the catalysts were tested under the same conditions, non-catalytic gas phase reactions should contribute in a similar way. Therefore the difference in the catalytic performance is more likely due to the variation in the surface properties of the catalysts. All the catalytic results are also summarized in Table 4–5.

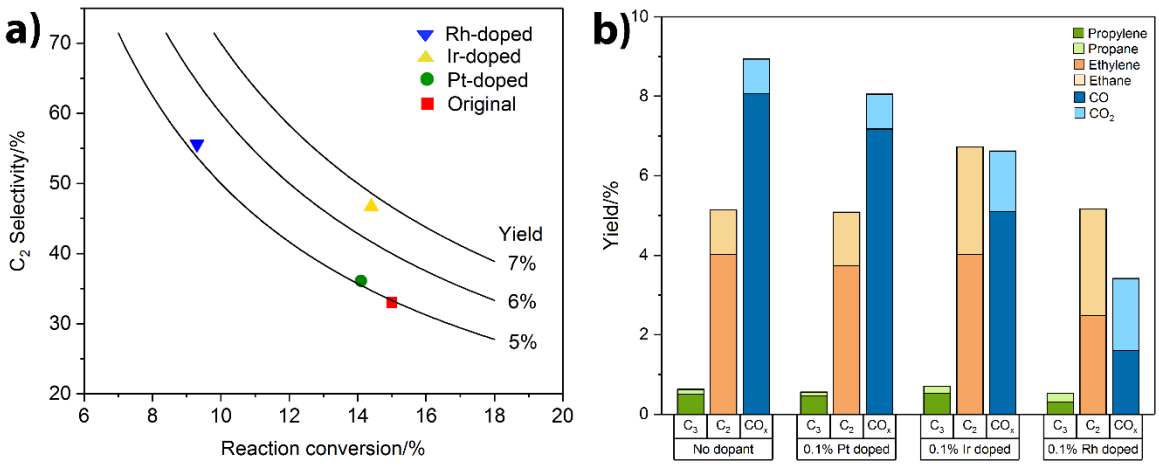

Fig. 4–9. a) Conversion-Selectivity plot and b) Reaction yield for all the catalysts in the OCM reaction. Reaction conditions: feed composition of CH_4:O_2:N_2 = 4:1:4, total flow rate of 60 sccm, and reaction temperature of 750 °C.

Since the ICP-AES (Table 4–2), BET (Table 4–1), and XRD (Fig. 4–5) measurements all showed similar results, the difference in the catalytic behavior, especially the enhancement of C_2 selectivity for the doped catalysts could hardly be explained by the difference in their structural and compositional characteristics. It is commonly agreed that the OCM reaction proceeds via a heterogeneous-homogeneous mechanism, where ethane is primarily formed through the gas-phase recombination of methyl radicals that are generated through surface reactions. Ethylene is then formed via the dehydrogenation of ethane either homogeneously or heterogeneously. CO_x, on the other hand, is produced from the consecutive oxidation of either the methyl radicals or the C_2 products [29]. The enhancement of C_2 selectivity implies a restraint on these deep oxidation reactions, which could result from a more optimized strength of interaction between the carbon intermediate species and the surface of the catalyst, which allows them to desorb readily into the gas phase without being further consumed by the surface oxygen [30]. This is evidenced by the fact that there is significantly less amount of carbon left on the surface of the noble metal doped catalysts after the reaction (Table 4–4) and also lower olefin to paraffin ratios obtained on these catalysts (Table 4–5).

In addition, the change in the redox property of the oxide species (Fig. 4–7) would alter the electronic structure at the surface of the catalysts, thus affecting the strength of their interaction with the reaction intermediates, which could also be part of the reason for the enhanced performance. As has been mentioned in section 4.3.1.4., the reaction involves the activation of oxygen on the Mn^{2+} sites. The improvement of the reducibility of Mn species would imply an increased ability to activate oxygen. On the other hand, the activation of methane occurs mainly on the WO_4^{2-} sites, to which a facile reduction of the W species would be beneficial. The Rh-doped catalyst showed the Mn reduction feature at the lowest temperature, followed by the Ir-doped sample. On the other hand, the Ir-doped and Pt-doped catalysts showed higher degree of reduction of W than the Rh-doped sample at the temperature (750 °C) where the catalytic measurements were carried out. These two factors together result in a higher overall C_2 yield for the Ir-doped catalyst. The Rh-doped sample, although having Mn reduction peak at the lowest temperature, showed smaller

amount of enhancement in the overall C_2 yield due to a more difficult reduction of WO_4^{2-} species, which would lead to a weaker methane activation process.

4.4 Conclusions

To summarize, noble metal doped M-Mn_xO_y-Na_2WO_4/MCF-17 (M = Pt, Ir, Rh) catalysts with similar elemental compositions were prepared via a wet impregnation method, and their performance in the OCM reaction was tested. When compared to the undoped Mn_xO_y-Na_2WO_4/MCF-17 catalyst, the incorporation of the noble metals enhanced the selectivity towards both C_2 and C_3 hydrocarbons in the order of Rh-doped>Ir-doped>Pt-doped catalyst and offered lower olefin to paraffin ratios. On the other hand, the Ir-doped catalyst showed the highest C_2 yield, followed by the Rh-doped sample. Since no significant difference between the original and the doped catalysts was observed in terms of elemental loading, surface area, and phase composition, the enhanced OCM performance was attributed to a more optimized strength of interaction between the carbon intermediate species and the surface of the noble metal doped catalysts in combination with an improved reducibility of W and Mn species and metal dispersion.

4.5 References

1. Alvarez-Galvan MC, Mota N, Ojeda M, Rojas S, Navarro RM, Fierro JLG (2011) Catal Today 171:15–23
2. Galadima A, Muraza O (2016) J Ind Eng Chem 37:1–13
3. Hammond C, Conrad S, Hermans I (2012) ChemSusChem 5:1668–1686
4. Lunsford JH (1995) Angew Chemie Int Ed English 34:970–980
5. Alexiadis VI, Chaar M, van Veen A, Muhler M, Thybaut JW, Marin GB (2016) Appl Catal B Environ 199:252–259
6. Zavyalova U, Holena M, Schlögl R, Baerns M (2011) ChemCatChem 3:1935–1947
7. Arndt S, Otremba T, Simon U, Yildiz M, Schubert H, Schomäcker R (2012) Appl Catal A Gen 425–426:53–61
8. Wang J, Chou L, Zhang B, Song H, Zhao J, Yang J, Li S (2006) J Mol Catal A Chem 245:272–277
9. Ji S, Xiao T, Li S, Xu C, Hou R, Coleman KS, Green ML (2002) Appl Catal A Gen 225:271–284
10. Yildiz M, Aksu Y, Simon U, Kailasam K, Goerke O, Rosowski F, Schomäcker R, Thomas A, Arndt S (2014) Chem Commun 50:14440–14442
11. Yildiz M, Aksu Y, Simon U, Otremba T, Kailasam K, Göbel C, Girgsdies F, Görke O, Rosowski F, Thomas A, Schomäcker R, Arndt S (2016) Appl Catal A Gen 525:168–179
12. Labinger JA, Bercaw JE (2002) Nature 417:507–14

13. Wencel-Delord J, Dröge T, Liu F, Glorius F (2011) Chem Soc Rev 40:4740–4761

14. Latimer AA, Kulkarni AR, Aljama H, Montoya JH, Yoo JS, Tsai C, Abild-Pedersen F, Studt F, Nørskov JK (2016) Nat Mater 1:1–6

15. Wang C-C, Siao SS, Jiang J (2012) J Phys Chem C 116:6367–6370

16. Pham TLM, Leggesse EG, Jiang JC (2015) Catal Sci Technol 5:15–18

17. Han Y, Lee SS, Ying JY (2007) Chem Mater 19:2292–2298

18. Musselwhite N, Na K, Sabyrov K, Alayoglu S, Somorjai GA (2015) J Am Chem Soc 137:10231–10237

19. Liu W-C, Melaet G, Ralston WT, Alayoglu S, Horowitz Y, Ye R, Hurlburt T, Mao B, Crumlin E, Salmeron M, Somorjai GA (2016) Catal Letters 146:1574–1580

20. Melaet G, Ralston WT, Li C-S, Alayoglu S, An K, Musselwhite N, Kalkan B, Somorjai GA (2014) J Am Chem Soc 136:2260–2263

21. Ji S-F, Xiao T-C, Li S-B, Xu C-Z, Hou R-L, Coleman KS, Green MLH (2002) Appl Catal A Gen 225:271–284

22. Kou Y, Zhang B, Niu J, Li S, Wang H, Tanaka T, Yoshida S (1998) J Catal 173:399–408

23. Palermo A, Vazquez JPH, Lee AF, Tikhov MS, Lambert RM (1998) J Catal 177:259–266

24. Wang P, Zhao G, Wang Y, Lu Y (2017) Sci Adv 3:e1603180

25. Nesbitt HW, Banerjee D (1998) Am Mineral 83:305–315

26. Elkins TW, Hagelin-Weaver HE (2015) Appl Catal A Gen 497:96–106

27. Koirala R, Büchel R, Pratsinis SE, Baiker A (2014) Appl Catal A Gen 484:97–107

28. Liu Y, Luo M, Wei Z, Xin Q, Ying P, Li C (2001) Appl Catal B Environ 29:61–67

29. Kondratenko EV, Baerns M (2008) In: Ertl G, Knözinger H, Schüth F, Weitkamp J (eds) Handbook of Heterogeneous Catalysis, 2nd ed. Wiley-VCH, Weinheim, pp 3010–3023

30. Kumar G, Lau SLJ, Krcha MD, Janik MJ (2016) ACS Catal 6:1812–1821

Chapter 5 – Preliminary Study of Manganese–Tungsten–Oxide (Mn–W–O_x) Nanoparticles and Hydroxylated Hexagonal Boron Nitride (*h*-BN) Catalysts in Oxidative Coupling of Methane (OCM)

Abstract

Monodispersed leaf-like manganese–tungsten–oxide (Mn–W–O_x) nanoparticles were synthesized through a co-reduction method with Mn-oleate and $W(CO)_6$ as precursors. Transmission electron microscopy (TEM) analysis revealed the branched nature of the nanoparticles and scanning transmission electron microscopy–energy dispersive X-ray spectroscopy (STEM–EDS) measurements confirmed the homogeneous distribution of Mn and W within the nanoparticles. The as-synthesized Mn–W–O_x nanoparticles were loaded into mesoporous silica MCF–17 and the resulting catalyst was tested in the oxidative coupling of methane (OCM). In addition, hydroxylated hexagonal boron nitride (*h*-BN) as a novel catalyst in the OCM reaction was evaluated. The structural backbone of *h*-BN was confirmed by X-ray diffraction (XRD) and Fourier transform infrared (FT-IR) spectroscopy measurements. STEM–EDS and FT-IR measurements showed successful functionalization of *h*-BN with hydroxyl groups. The functionalized *h*-BN nanosheets showed good activity in the OCM reaction with moderate selectivity towards C_2 hydrocarbons. In the meantime, the catalyst faced serious deactivation, which was not alleviated by lowering the reaction temperature or the oxygen concentration in the reaction gas feed.

5.1 Introduction

OCM reaction over Mn_xO_y-Na_2WO_4/SiO_2 catalysts involves the activation of oxygen and methane on Mn^{2+} and WO_4^{2-} sites, respectively. This mechanism inspires the use of binary oxide nanoparticles that contain both Mn and W in intimate contact for the OCM reaction. Confining both the Mn and W sites within one particles and in close proximity with each other could potentially lead to a more efficient synergistic effect and eventually an enhanced OCM performance. In addition, with the powerful colloidal chemistry, binary oxide nanoparticles with controlled size, shape, and composition could be synthesized [1–4]. This would be beneficial in relating the catalytic performance to the well-defined structure of the nanoparticles, as compared to the situation with conventional impregnation catalysts.

Hexagonal boron nitride (*h*-BN), a structural analogue to the well-known graphene, has a layered structure characterized by alternately arranged B and N atoms in two-dimensional planes, forming a hexagonal lattice [5]. It is an important two-dimensional functional material and is widely used as solid lubricant, high temperature ceramics, and high temperature insulator due to its unique structural and electronic properties [6]. In addition to the above mentioned applications, *h*-BN nanomaterials are also utilized in catalysis as both support material and catalyst itself in various electrocatalytic and liquid–phase reactions such as the Oxygen Reduction Reaction (ORR) [7, 8] and oxidative desulfurization of aromatic sulfur compounds [9–11]. However, the use of *h*-BN as the active phase in gas-phase heterogeneous reactions is rarely reported.

Recently, *h*-BN as novel catalysts in C–H bond activation in the gas-phase oxidative dehydrogenation of small alkanes are reported [12–17]. Excellent selectivity towards the corresponding alkenes was observed along with an outstanding catalyst stability. The proposed reaction mechanism involves the activation of alkanes on the surface B–O(H) sites [12, 14, 15]. Since both the oxydehydrogenation and oxidative coupling of methane share the step of C–H bond activation, it is reasonable to speculate the improved C–H activation process observed on *h*-BN catalysts would be beneficial to the OCM reaction. By increasing the surface B–OH content, the activity of C–H activation on hydroxylated *h*-BN would be improved. However, due to the high resistance towards oxidation, functionalization of *h*-BN by oxidizing with molecular oxygen is not feasible under typical laboratory conditions [6] and therefore alternative methods have to be utilized. It is reported that by substituting the C atoms in graphitic C_3N_4 (*g*-C_3N_4) with B–OH units from H_3BO_3 precursor, hydroxylated *h*-BN with extremely high hydroxylation degrees could be obtained, which is ideal in producing hydroxylated *h*-BN for study in the OCM reaction.

In this chapter, the potential use of MCF–17 supported Mn–W–O_x nanoparticles and hydroxylated *h*-BN as catalysts in the oxidative coupling of methane (OCM) is explored. The synthesis of both materials are presented and the detailed parameters for the formation of branched Mn–W–O_x nanoparticles are reported. The synthesized materials are characterized with transmission electron microscopy (TEM), X-ray diffraction (XRD), and Fourier transform infrared (FT-IR) spectroscopy. Preliminary results on the catalytic performance of the two catalysts under different conditions are summarized.

5.2 Experimental

5.2.1 Material Synthesis

5.2.1.1 Synthesis of Manganese Oleate Precursor

The manganese oleate precursor used for the synthesis of manganese–tungsten–oxide (Mn–W–O_x) nanoparticles is synthesized according to a previously reported recipe [18]. Briefly, 7.92 g of manganese chloride tetrahydrate [$MnCl_4$, ≥99%] and 24.36 g of sodium oleate (TCI, 95%) were dissolved in a solvent containing ethanol (40 mL), deionized water (30 mL), and n-hexane (70 mL). The mixture was heated to 60 ºC and stirred vigorously at this temperature for 4 h. The hexane phase containing manganese oleate product was separated using a separation funnel, washed several times with deionized water, and then dried sufficiently with $MgSO_4$. Manganese oleate was collected by removing hexane using a rotary evaporator. The reddish–brown waxy solid was stored in a desiccator until further use.

5.2.1.2 Synthesis of Manganese–Tungsten–Oxide (Mn–W–O_x) Nanoparticles

The synthesis of manganese–tungsten–oxide (Mn–W–O_x) nanoparticles was carried out using the standard Schlenk line technique. 309 mg of pre-synthesized manganese oleate, 176 mg of tungsten hexacarbonyl [$W(CO)_6$, 97 %], and 1543 mg of oleic acid (technical grade, 90%) were first added into a 100 mL three-neck round-bottom flask, to which 15 mL of 1-octadecene [technical grade, 90%] and 333 mg of trimethylamine N-oxide dehydrate [TMAO, 98%] were added as reaction solvent and oxidant, respectively. The reaction flask was then degassed and refilled with argon for three times at room temperature. The reaction mixture was heated to 300 ºC with a heating rate of 4 ºC/min using a heating mental and held at 300 ºC for 2 h before being cooled down to room temperature. During the synthesis, the color of the reaction mixture remained milky-white until the reaction temperature reached 175 ºC, when it began to turn darker and finally became dark brown. The synthesized nanoparticles were collected by centrifugation and washed several times with acetone before being dispersed in toluene and stored for further use.

5.2.1.3 Preparation of Supported Mn–W–O_x Nanoparticle Catalysts on Mesoporous Silica MCF–17

The as-synthesized Mn–W–O_x nanoparticles were supported on MCF–17 type mesoporous silica via sonication. Briefly, pre-synthesized MCF–17 powder (BET surface area: ~710 m^2/g) was dispersed in toluene, to which Mn–W–O_x nanoparticle dispersion was added to achieve the desired loading. After being sonicated for 1 h, the suspension was centrifuged at 4300 rpm and washed with 75 vol% ethanol in acetone for five times. The final catalyst was dried overnight at 100 ºC and stored in a sealed glass vial until further use.

5.2.1.4 Synthesis of Hydroxylated *h*-BN

The hydroxyl group (–OH) functionalized *h*-BN was synthesized according to a previously reported recipe [19]. Briefly, graphitic C_3N_4 (*g*-C_3N_4) was first synthesized by the polycondensation of dicyandiamide (99%, Aldrich) at 500 ºC for 4 h with a heating rate

of 2.2 °C/min in a tube furnace under nitrogen atmosphere [20]. The obtained yellow solid was grounded to fine powders and 3.0 g of which was mixed with 0.9 g of boric acid (≥99.5%, Sigma) in 100 mL of deionized water. The resulting mixture was sonicated for 30 min. The finely mixed *g*-C_3N_4 and H_3BO_3 powder was obtained by evaporating water at temperatures above 90 °C under constant stirring. Finally, the finely mixed *g*-C_3N_4 and H_3BO_3 powder was then loaded into a alumina combustion boat and calcined in a tube furnace at 800 °C for 1 h with a heating rate of 3.3 °C/min under nitrogen atmosphere.

5.2.2 Material Characterization

Transmission electron microscopy (TEM) and scanning transmission electron microscopy–energy dispersive X-ray spectroscopy (STEM–EDS) analysis were performed using a JEOL JEM2100F TEM equipped with an Inca Energy Dispersive Spectrometer operated at 200 kV. Samples for TEM analysis were prepared by first dispersing the catalysts in ethanol and then dropping the dispersion on ultrathin lacey carbon TEM grids (Ted Pella, Inc.).

X-ray diffraction (XRD) measurements of the fresh and spent catalysts were performed using a Bruker D2 Phaser Benchtop X-ray powder diffractometer with a Cu x-ray source (Kα 1.54184 Å). 2 theta value was varied from 10° to 60° with a step size of 0.02°.

Fourier transform infrared (FT-IR) spectroscopy measurements were carried out with a Nicolet 6700 FT-IR Spectrometer (Thermo Scientific) equipped with a DTGS KBr detector. FT-IR spectra were collected in the range of 400–4000 cm^{-1} at room temperature with 100 scans and 8 cm^{-1} resolution. Samples for FT-IR measurements were prepared by pressing the sample powder to a thin pellet.

5.2.3 Catalytic Measurements

OCM reaction was performed in a home-built fixed bed flow reactor under atmospheric pressure. The catalysts were sieved to an average grain size of 150–250 um. The sieved catalyst (Approximately 60 mg for MCF–17 supported Mn–W–O_x nanaoparticle and 30 mg for hydroxylated *h*-BN) was mixed with quartz sand (Umicore, 99.99%, grain size: 0.2–0.7 mm) and then packed in the center of a quartz reactor tube (Quartz Scientific, 16 inches, 4 mm ID, 6.35 mm OD). Additional quartz sand was packed on both sides of the catalytic bed to help reduce the empty space of the reactor and promote heat dissipation. Methane (Praxair, 5.0 Research Grade) and synthetic air (Praxair, Ultra Zero) were fed into the reactor using carefully calibrated mass flow controllers (Parker) with a total flow rate of 60 sccm and a varied composition of CH_4:O_2. The reactor was heated to the desired temperature (600–750 °C) with a heating rate of 8 °C/min by an electric tube furnace. Outlet gas was sampled and separated using an on-line GC–MS (Agilent 7890A-5975C) equipped with two capillary columns (HP-PLOT Q and HP-PLOT MoleSieve). The gaseous composition was analyzed by a thermal conductivity detector (TCD) and a flame ionization detector (FID) detector equipped with a methanizer. Calculation of reaction conversion and selectivity can be found in Chapter 4.

5.3 Results and Discussion

5.3.1 Manganese–Tungsten–Oxide (Mn–W–O_x) Nanoparticles

5.3.1.1 Synthesis of Manganese-Tungsten-Oxide (Mn–W–O_x) Nanoparticles

Fig. 5–1 are the TEM images of the as-synthesized Mn–W–O_x nanoparticles. It can be seen from Fig. 5–1a to 5–1c that the nanoparticles are leaf-like in shape with good monodispersity. Fig. 5–1d shows the TEM image of a single Mn–W–O_x nanoparticle, which confirms its branched nature. The size of the nanoparticles measured from the longest dimension is between 30 to 40 nm, although some size distributions do exist.

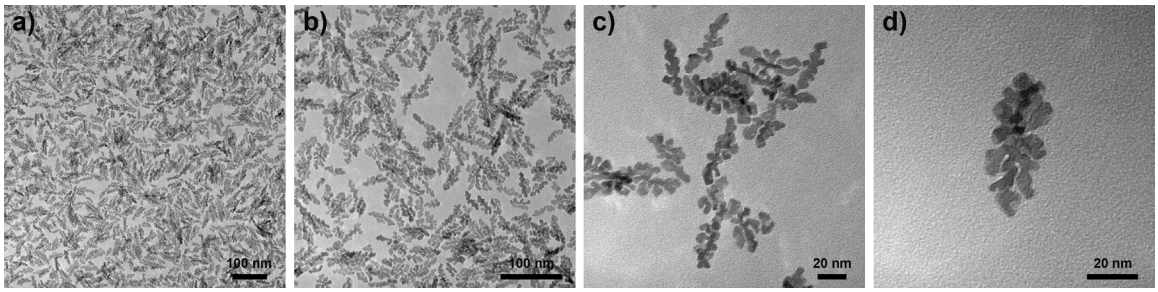

Fig. 5–1. TEM images of the as-synthesized Mn–W–O_x nanoparticles.

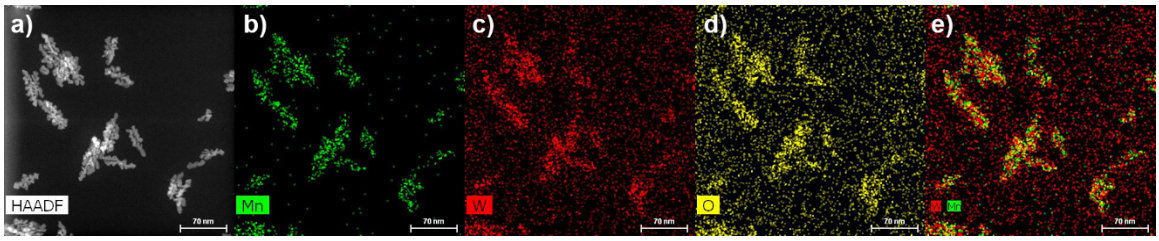

Fig. 5–2. a) HAADF image and b–d) EDS elemental mapping results of the as-synthesized Mn–W–O_x nanoparticles as shown in a) (Mn: green, W: red, O: yellow). e) Superimposed image of the elemental mapping results of Mn and W.

STEM–EDS measurements (Fig. 5–2) indicates that both Mn and W are homogeneously distributed and no oxide nanoparticles of either Mn or W alone were observed. Zoomed in HAADF image of the Mn–W–O_x nanoparticles is shown in Fig. 5–3b and EDS elemental mapping results of the corresponding area is given in Fig. 5–3c to 5–3f. The results confirmed the homogeneous distribution of both Mn and W and no obvious segregation of either of the elements was observed within the nanoparticles.

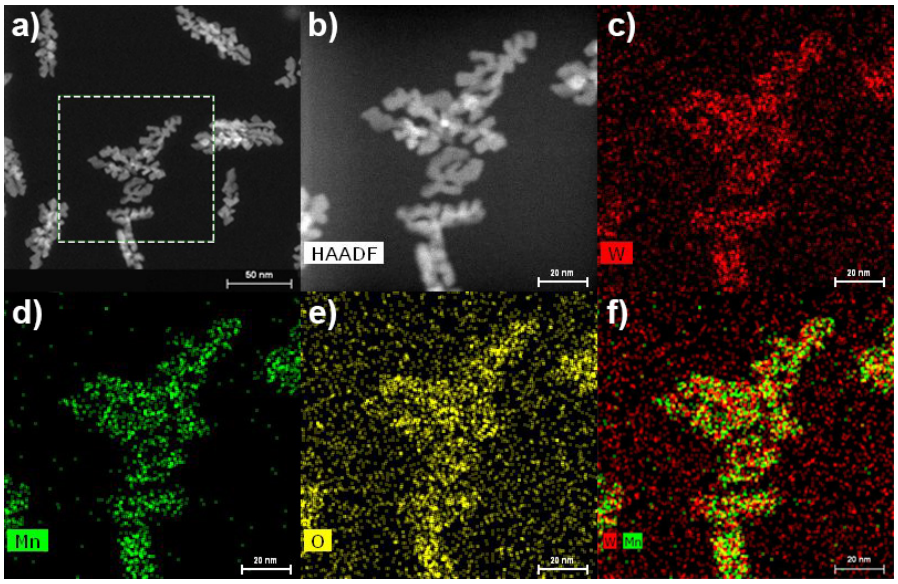

Fig. 5–3. a–b) HAADF images and c–e) EDS elemental mapping results of the as-synthesized Mn–W–O_x nanoparticles as shown in b) (Mn: green, W: red, O: yellow). f) Superimposed image of the elemental mapping results of Mn and W.

The effects of the amount of oleic acid and TMAO used during the synthesis were also investigated. Reducing the amount of oleic acid in half resulted in the change of the shape of the nanoparticles from leaf-like to nanorods (Fig. 5–4: a–b). It is noted that some of the nanorods showed a small degree of branching as indicated by the concave features along the long axis. This is possibly related to the wakened adsorption of oleic acid on the nanoparticles during their structure evolution due to its lowered chemical potential. On the other hand, double the amount of oleic acid used in the synthesis led to an increase in both the size and degree of branching of the resulting nanoparticles (Fig. 5–4: c–d).

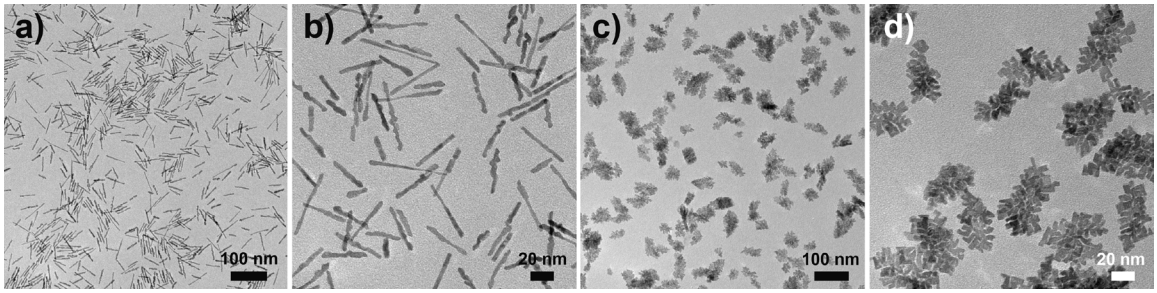

Fig. 5–4. TEM images of the Mn–W–O_x nanoparticles synthesized with a–b) half and c–d) double the amount of oleic acid originally used.

When the amount of oxidant is reduced to half of the original value, the effect is somewhat similar to the situation where the amount of oleic acid is doubled. The resulting nanoparticles were larger in size and showed a higher degree of branching (Fig. 5–5). This phenomenon can be rationalized by taking the competitive adsorption of oleic acid and trimethylamine produced by the reduction of TMAO into account. In the presence of amine species which has strong affinity to the nanoparticle surface, stronger competition from oleic acid by either a decreased concentration of TMAO or an increased concentration of oleic acid would result in an additional growth on partly uncovered surface of the

nanoparticle [21], leading to a higher degree of branching. In addition, the decreased oxidation power of the reaction media caused by the lowered concentration of TMAO would lead to a slower nucleation of the oxide nanoparticle and a decreased number of nuclei formed, which could contribute to the increased size of the resulting nanoparticles.

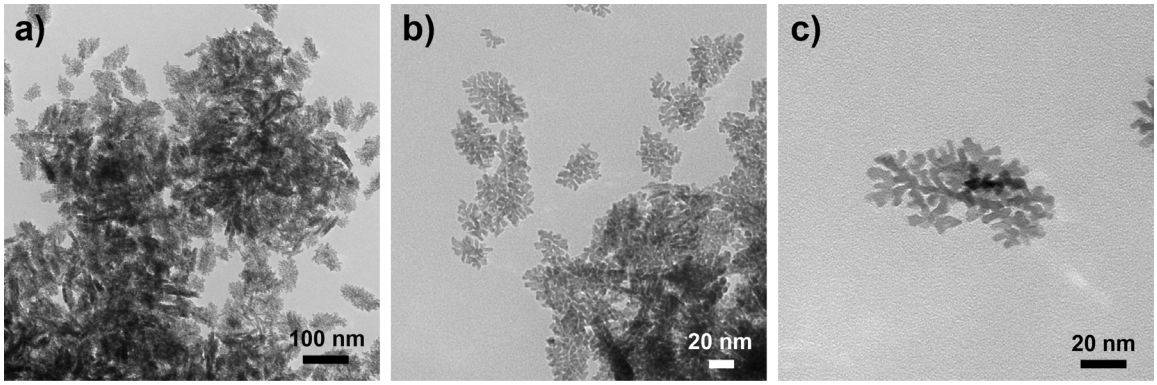

Fig. 5–5. TEM images of the Mn–W–O_x nanoparticles synthesized with half the amount of TMAO originally used.

5.3.1.2 Catalytic Performance of MCF–17 Supported Mn–W–O_x Nanoparticle Catalyst

The as-synthesized Mn–W–O_x nanoparticles were supported on mesoporous silica MCF–17 and used in the oxidative coupling of methane. The results are shown in Fig. 5–6. It can be seen from Fig. 5–6 that, despite a spike at around 300 min, the CH_4 conversion showed an initial decrease with more time on stream and stabilized at around 5.4%. The reaction selectivity towards C_2 hydrocarbons stayed fairly constant at 42% with ethylene to ethane ratio close to one. As compared to its impregnated counterpart, the Mn–W–O_x nanoparticle catalyst showed lower activity but higher selectivity towards C_2 hydrocarbons. However, meaningful comparison of the catalytic performance to the impregnated catalyst as reported in Chapter 4 is difficult at this point due to the absence of Na in the Mn–W–O_x nanoparticle and the difference in the conversion level (5.4% for the nanoparticle *vs.* 15.6% for the impregnated catalyst). Future work needs to be carried out to define the structure and composition of the Mn–W–O_x nanoparticles in detail.

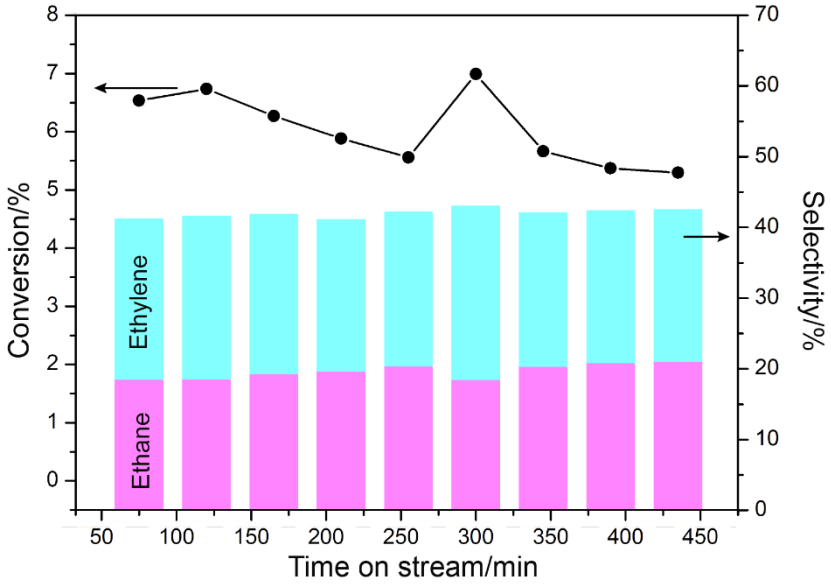

Fig. 5–6. Reaction conversion and selectivity towards C_2 hydrocarbons of MCF–17 supported Mn–W–O_x nanoparticle catalyst in OCM reaction as a function of reaction time on stream. Reactions were carried out at 750 °C and atmospheric pressure with CH_4:O_2 = 4:1 and total flow rate of 60 sccm.

5.3.2 Hydroxylated Hexagonal Boron Nitride (*h*-BN)

5.3.2.1 Synthesis of –OH Functionalized *h*-BN

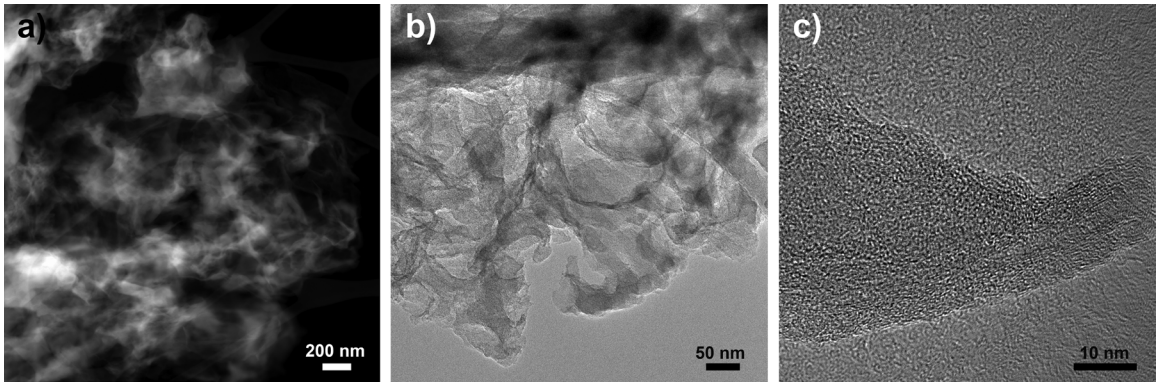

Fig. 5–7. a) HAADF and b–c) TEM images of the as-synthesized hydroxylated *h*-BN.

Both the TEM and HAADF images (Fig. 5–7a and 5–7b) reveals the sheet-like morphology of the synthesized hydroxylated *h*-BN. Fig. 5–7c shows a high-resolution image of the edge area of the hydroxylated *h*-BN, which confirms its layered structure. The HAADF and the corresponding EDS elemental mapping results (Fig. 5–8) confirmed the successful incorporation of B and O into the structure. However, significant amount of carbon was shown to have left on the surface of the hydroxylated *h*-BN after the synthesis due to the incomplete substitution.

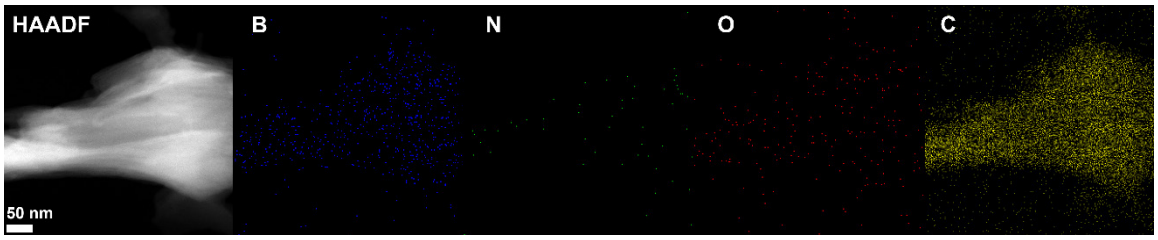

Fig. 5–8. HAADF image and the corresponding EDS elemental mapping results of the as-synthesized hydroxylated *h*-BN (B: blue, N: green, O: red, C: yellow).

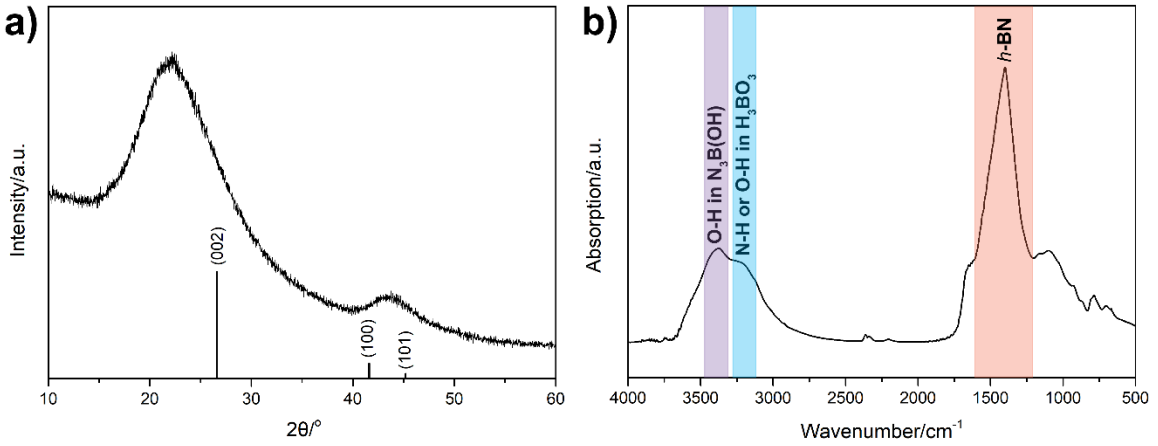

Fig. 5–9. a) XRD pattern and b) FT-IR spectrum of the as-synthesized hydroxylated *h*-BN. The standard XRD pattern for bulk *h*-BN as shown in a) is taken from JCPDS #01-073-2095.

Fig. 5–9a shows a typical XRD spectrum of the synthesized hydroxylated *h*-BN. The peaks at 22.4° and 43.7° correspond to (002) and (100)/(101) planes of *h*-BN with the main diffraction peak associated with (002) direction shifted to lower angles as compared to the bulk *h*-BN. The backbone of *h*-BN was confirmed by the intense absorption feature at around 1396 cm^{-1} in the FT-IR spectrum, which is characteristic for *h*-BN. The feature at around 3380 cm^{-1} was ascribed to the stretching vibration mode from the O–H in $N_3B(OH)$ units [22], which confirms the successful functionalization of *h*-BN with hydroxyl groups. The shoulder feature at around 3220 cm^{-1} was associated with the absorption from either the N–H in the BN backbone or the O–H from the H_3BO_3 residue.

5.3.2.2 Catalytic performance of –OH Functionalized *h*-BN

The as-synthesized hydroxylated *h*-BN was tested in the OCM reaction and the results are shown in Fig. 5–10. The catalyst showed good activity with up to 20% CH_4 conversion and 5.3% C_2 yield. Unfunctionalized *h*-BN was barely active in the OCM reaction at the temperatures tested, indicating an enhanced activity induced by the surface hydroxylation. However, fast deactivation was observed after 120 min of reaction and the catalyst completely lost its activity after 200 min of time on stream.

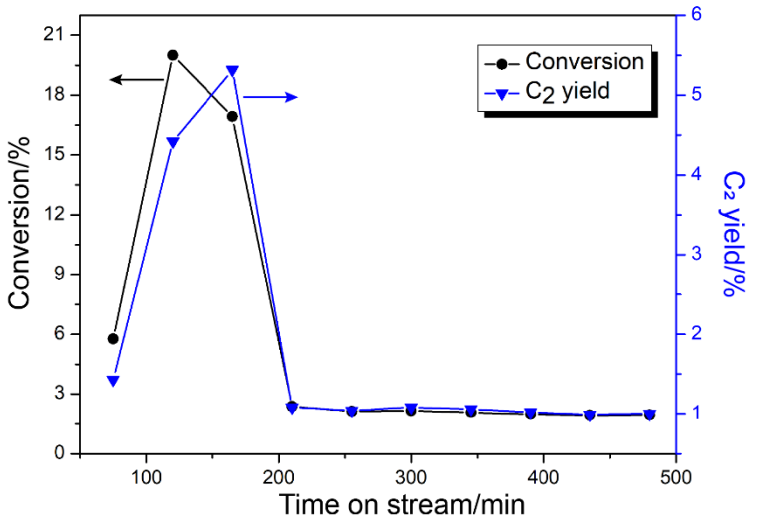

Fig. 5–10. Reaction conversion and C_2 hydrocarbon yields of the hydroxylated *h*-BN catalyst in OCM reaction as a function of reaction time on stream. Reactions were carried out at 750 °C and atmospheric pressure with CH_4:O_2 = 4:1 and total flow rate of 60 sccm.

The effects of reaction temperature and oxygen concentration in the reaction gas feed were investigated. Lowering the reaction temperature to 700 °C led to a slight decrease in the C_2 yield, while severe catalyst deactivation was still observed. Further decreasing the reaction temperature to 650 °C slowed down the deactivation process but resulted in a drastic decrease in the C_2 yield. On the other hand, reducing the oxygen concertation in the gas feed led to a sharp decrease of the overall reaction activity. At CH_4 to O_2 ratio of 10:1, the reaction conversion was almost negligible.

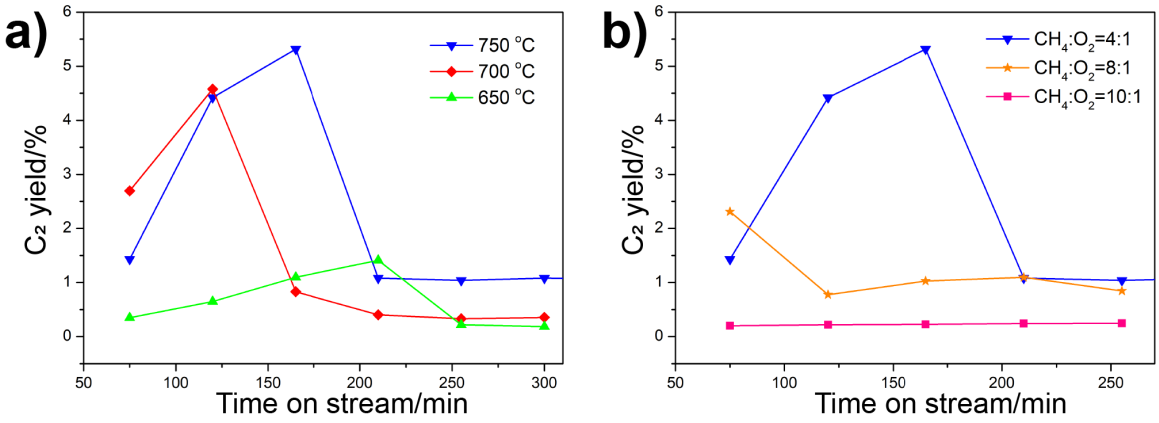

Fig. 5–11. C_2 hydrocarbon yields of the hydroxylated *h*-BN catalyst in OCM reaction at a) various reaction temperatures (650 °C, 700 °C, and 750 °C) and b) various CH_4 to O_2 ratios (4:1, 8:1, and 10:1). Reactions were carried out at 750 °C and atmospheric pressure with CH_4:O_2 = 4:1 and total flow rate of 60 sccm, if not otherwise specified.

5.4 Conclusions and Future Work

To summarize, monodispersed leaf-like manganese–tungsten–oxide (Mn–W–O_x) nanoparticles were synthesized via a colloidal process with Mn-oleate and $W(CO)_6$ as Mn and W sources, respectively. Mn and W were shown to be homogeneously distributed

within the binary oxide nanoparticles. MCF–17 supported Mn–W–O_x nanoparticle catalyst showed a CH_4 conversion of 5.4% and C_2 selectivity of 42% with good stability over time in OCM reaction carried out at 750 ºC with CH_4:O_2 = 4:1. On the other hand, hydroxylated hexagonal boron nitride (*h*-BN) as a novel catalyst in the OCM reaction was evaluated. Functionalizing *h*-BN with –OH groups resulted in good activity in OCM reaction with moderate selectivity towards C_2 hydrocarbons. In the meantime, the catalyst faced serious deactivation, which was not eliminated by lowering the reaction temperature or the oxygen concentration in the reaction gas feed. Additional work has to be carried out to fully characterize both the W–Mn–O_x nanoparticle catalyst and hydroxylated *h*-BN, preferably under reaction relevant conditions. Specifically, future work has to be carried out to 1. Systematically tune the composition of the W–Mn–O_x nanoparticles and correlate it to its performance in the OCM reaction. 2. Introduce Na into the binary oxide and compare the performance of the resulting nanoparticles to its impregnated counterpart. 3. Identify the surface species on the hydroxylated *h*-BN and investigate their connection with the reaction activity. 4. Understand the mechanism for catalyst deactivation of hydroxylated *h*-BN and modify the catalyst for better stability. 5. Promote the hydroxylated *h*-BN catalyst with alkali or noble metals to tailor the adsorption and dissociation properties of the reactant molecules for better performance.

5.5 References

1. Niederberger M (2007) Acc Chem Res 40:793–800
2. Choi J, Moon K, Kang I, Kim S, Yoo PJ, Oh KW, Park J (2015) Chem Eng J 281:236–242
3. Zhang Y, Li L, Su H, Huang W, Dong X (2015) J Mater Chem A 3:43–59
4. Van Embden J, Chesman ASR, Jasieniak JJ (2015) Chem Mater 27:2246–2285
5. Wang J, Ma F, Sun M (2017) RSC Adv 7:16801–16822
6. Zheng Z, Cox M, Li B (2018) J Mater Sci 53:66–99
7. Chen X, Chang J, Yan H, Xia D (2016) J Phys Chem C 120:28912–28916
8. Siahrostami S, Tsai C, Karamad M, Koitz R, García-Melchor M, Bajdich M, Vojvodic A, Abild-Pedersen F, Nørskov JK, Studt F (2016) Catal Lett 146:1917–1921
9. Wu P, Zhu W, Wei A, Dai B, Chao Y, Li C, Li H, Dai S (2015) Chem - A Eur J 21:15421–15427
10. Wu P, Zhu W, Chao Y, Zhang J, Zhang P, Zhu H, Li C, Chen Z, Li H, Dai S (2016) Chem Commun 52:144–147
11. Zhu W, Dai B, Wu P, Chao Y, Xiong J, Xun S, Li H, Li H (2015) ACS Sustain Chem Eng 3:186–194
12. Grant JT, Carrero CA, Goeltl F, Venegas J, Mueller P, Burt SP, Specht SE, McDermott WP, Chieregato A, Hermans I (2016) Science 354:1570–1573

13. Shi L, Yan B, Shao D, Jiang F, Wang D, Lu AH (2017) Chinese J Catal 38:389–395

14. Shi L, Wang D, Song W, Shao D, Zhang WP, Lu AH (2017) ChemCatChem 9:1788–1793

15. Huang R, Zhang B, Wang J, Wu KH, Shi W, Zhang Y, Liu Y, Zheng A, Schlögl R, Su DS (2017) ChemCatChem 9:3293–3297

16. Venegas JM, Grant JT, McDermott WP, Burt SP, Micka J, Carrero CA, Hermans I (2017) ChemCatChem 9:2118–2127

17. Grant JT, Mcdermott WP, Venegas JM, Burt SP, Micka J, Phivilay SP, Carrero CA, Hermans I (2017) ChemCatChem 9:3623–3626

18. An K, Park M, Yu JH, Na H Bin, Lee N, Park J, Choi SH, Song IC, Moon WK, Hyeon T (2012) Eur J Inorg Chem 2012:2148–2155

19. Li X, Hartley G, Ward AJ, Young PA, Masters AF, Maschmeyer T (2015) J Phys Chem C 119:14938–14946

20. Ong WJ, Tan LL, Ng YH, Yong ST, Chai SP (2016) Chem Rev 116:7159–7329

21. Schladt TD, Graf T, Tremel W (2009) Chem Mater 21:3183–3190

22. Weng Q, Wang B, Wang X, Hanagata N, Li X, Liu D, Wang X, Jiang X, Bando Y, Golberg D (2014) ACS Nano 8:6123–6130